The effect of machining marks within the pick interval cusp and a 5 axis milling simulation model

Chun Hin CHAN

Supervisor: Prof. Simon Barrans & Dr. Karl Walton

A thesis submitted to the University of Huddersfield in partial fulfilment of the requirements for the degree of Doctor of Philosophy

March, 2023

Copyright

The following papers listed were studied previously contributed by the authors:

This paper reported research that I carried out and was written by me. The co-author was one of my supervisors who directed the work and had editorial input to the paper. Chan, C., & Barrans, S. (2021). Simulating 5-Axis Milling with a Ball Nose Cutting Tool. Paper presented at the 2021 12th International Conference on Mechanical and Aerospace Engineering (ICMAE).

This paper reported research that I carried out and was written by me. The co-author was one of my supervisors who directed the experiment and had editorial input to the paper. Chan, C., & Walton, K. (2021). Areal Decomposition Methodology for a 5-Axis Milled Surface. Paper presented at the Advances in Manufacturing Engineering and Materials II: Proceedings of the International Conference on Manufacturing Engineering and Materials (ICMEM 2020), 21–25 June, 2021, Nový Smokovec, Slovakia.

Abstract

The use of 5-axis milling to produce a freeform component has become more popular than conventional die casting in many industries. Turbocharger compressor wheels are one of the components that require long a life-time and high durability. Improvements in 5-axis milling lead manufacturers to use this method to produce such wheels, because the cutting is more precise and there are fewer imperfections in the material. A ball end cutting tool is one of the commonest tools used to cut materials in 5-axis milling. This cutting tool leaves cusp marks on the surface across the feed direction. In this work, an optical inspection machine has been used to inspect the topography of the cusp surface. A model has been developed to simulate the marks generated by 5-axis milling using a ball end cutting tool. This model incorporates the cutter shape, number of cutting edges and the lead and tilt angles of the cutting tool, and it uses transformation matrixes to define the cutter position and cutting locus to simulate the cutting edge's motion. By filtering the lowest surface of the cutting locus, it creates the surface that simulates the final surface. This result contained a continuous cutting mark that simulates a surface under perfect cutting conditions and with different cutting parameters. The difference between actual cutting trials and the simulation is less than 5.6%.

Also, the feed interval marks within the pick interval cusps have been investigated using cylindrical form removal, wavelet filtering and polynomial filtering. Cylindrical form removal is a function in Alicona Infinite Focus Measurement G4. The wavelet filtering and polynomial filtering are provided by software called SurfStand. The results show that the arithmetical mean height (Sa) of a surface increased in proportion to the feed rate since the faster tool feed rate creates vibration during the cutting process, and if the spindle speed was too slow there was less cutting action.

Acknowledgements

I would like to thank my main supervisor, Prof. Simon Barrans, for his extensive support and knowledge throughout my studies. His guidance was invaluable and I learned a lot from him. I will owe him my thanks for the rest of my life.

I would like to extend my thanks to my second supervisor, Dr. Karl Walton, for his advice and knowledge. He has led me to become a professional engineer specialising in surface inspection.

Many thanks also to the Prof. Liam Blunt and Tukun Li for their support at the Centre for Precision Technologies (CPT) in the University of Huddersfield, and also for allowing me access to the facilities and the use of the SurfStand software.

Contents

List of Figures

List of Tables

Nomenclature (list of symbols)

Roman lower case

c	y axis in the FCN coordinate system
f	x axis in the FCN coordinate system
f_x	Feed rate
n	z axis in the FCN coordinate system
r	Radius of the cutting tool
r_i	The radius of the point on the cutting edge

t	time
u	x axis in the tool coordinate system
v	y axis in the tool coordinate system
vb	Highest frequency in the bandwidth
vs	Sampling rate
w	z axis in the tool coordinate system
w_i	The Length from tool tip to the height of the point on cutting edge

Roman upper case

CPT	Centre for Precision Technologies in University of Huddersfield
C	Cross feed
F	Feed
N	Normal to the axis
Ni	Total number of peak
Ra	Arithmetic mean surface roughness
Sa	Arithmetical mean height
Sk	Surface core height
Svk	Reduced valley depth
Sz	Maximum height
$Z_{(x)}$	Profile height function

Greek lower case

β	The angle between the point and the u axis
θ	Angle of the point on the cutting edge
ξ	Tilt angle
φ	Lead angle
ω	Spindle speed

1. Introduction

1.1. Project background

1.1.1. 5-axis milling machine

5-axis milling is one of the most advanced manufacturing technologies that is used widely in various industries such as the automotive, aerospace and medical industries. Conventional 3-axis milling uses a milling machine where the spindle only moves in the z direction, and the bed plate provides the x and y motions. This type of machine is a more cost effective, easier to operate and requires less maintenance than 5-axis milling machines. However, 3-axis milling has limited capability and efficiency because neither the bed plate nor the spindle can rotate about other axes. Sheen and You (2006) stated that this type of milling is commonly used to cut a 2D and 2.5D geometry. Unlike 5-axis milling with three directions of movement and two axes of rotation, 3-axis milling cannot produce a component as complex as 5-axis milling. According to Chen et al. (2019), 5-axis milling can provide high efficiency, high quality and high precision as a result of the high cutting speed and with fewer internal imperfections in the material. Jung et al. (2002) & Shaw and Ou (2008) identify two principal types of 5-axis layout: (a) AB type, (b) AC type. The AB type uses the conventional three x, y and z axes with a rotational movement on the x-axis referred to as the A-axis and on the y-axis referred to as the B-axis, as shown in Fig 1. The AC type is like the AB type except that the rotational movement is on the z-axis rather than on the y-axis. These two types of 5-axis milling machine can produce a complex component with 3D geometry.

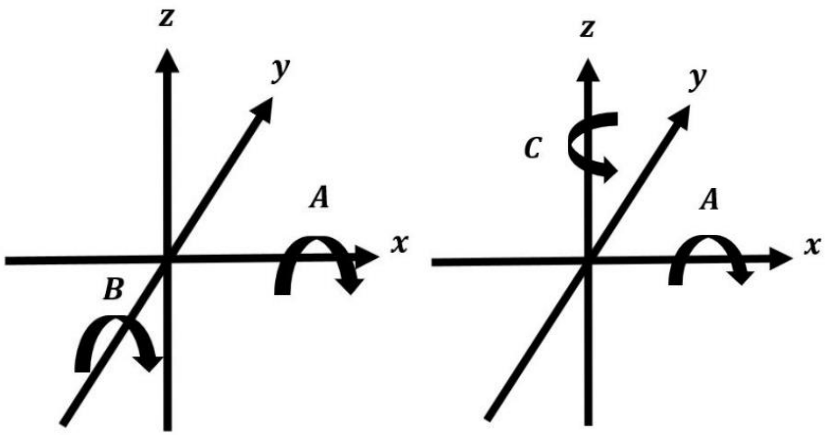

Figure 1. (a) AB type 5-axis milling layout (b) AC type 5-axis milling layout

1.1.2. The need for 5-axis ball end milling

5-axis milling has been used widely in industries such as the automotive and aerospace industries. This technique can not only machine plane surfaces or cylinders, but can also machine a complete 3D component. An example of a turbocharger compressor wheel is shown in Fig 2.

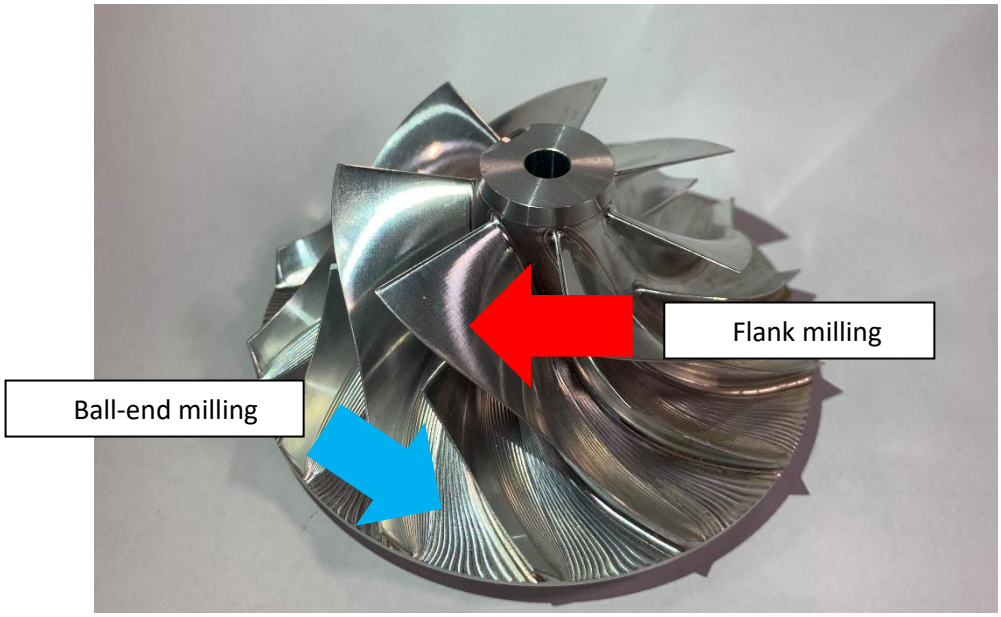

Figure 2. A sample of a turbocharger compressor wheel

The surface of these blades (Red arrow) were shaped by flank milling, using the side of the end milling tool to cut the surface. The surface of the hub (blue arrow) was shaped by ball-end milling. Therefore, the bottom area shows very clear cusp marks. Conventional 3-axis milling cannot cut such a component because the blades are not perpendicular to the bottom plane of the component, and the cutting tool cannot reach the area beneath the blades to cut the material. Since 5-axis milling can cut a more complex surface, the demand for its use is increasing, and hence more investigations are needed. Tabriz et al. (2017) investigated the effect of different cutting parameters on the roughness of surfaces machined by 5-axis ball-end milling. According to Ozturk et al. (2009), the aerospace, die-cast and automotive industries use 5-axis milling because it improves tool accessibility and contouring on complex surfaces and geometries. Prat et al. (2012) pointed out that the aeronautical, spatial and energy sectors use this milling technique to machine complex parts such as blades, impellers or inducers, as those parts may be made from difficult-to-cut material such as titanium alloy. The study also mentioned that ball end or hemispherical cutters are used to finish those parts. Xu et al. (2020) & Li et al. (2016) used this milling method to machine the contours of the curved blades of the impeller since the impeller has a complex curved features . Tan et al. (2020) investigated the surface integrity and fatigue properties of TC17 alloy blades machined by ball end milling, since forging the blades is not ideal . Habibi et al. (2021) used 5-axis ball-end milling to machine blade specimens. Yu et al. (2021) studied the surface improvement resulting from using a 5-axis milling to machine a non-circular gear.

1.1.3. 5-axis milling with ball end cutter

A ball end cutter is an end mill with a hemispherical tool end with multiple cutting edges. This type of cutter is also called a ball nose end cutter or spherical end cutter. An example of a ball end cutter is shown in Fig 3. In the milling process, the only very end of the cutter will be used to cut material.

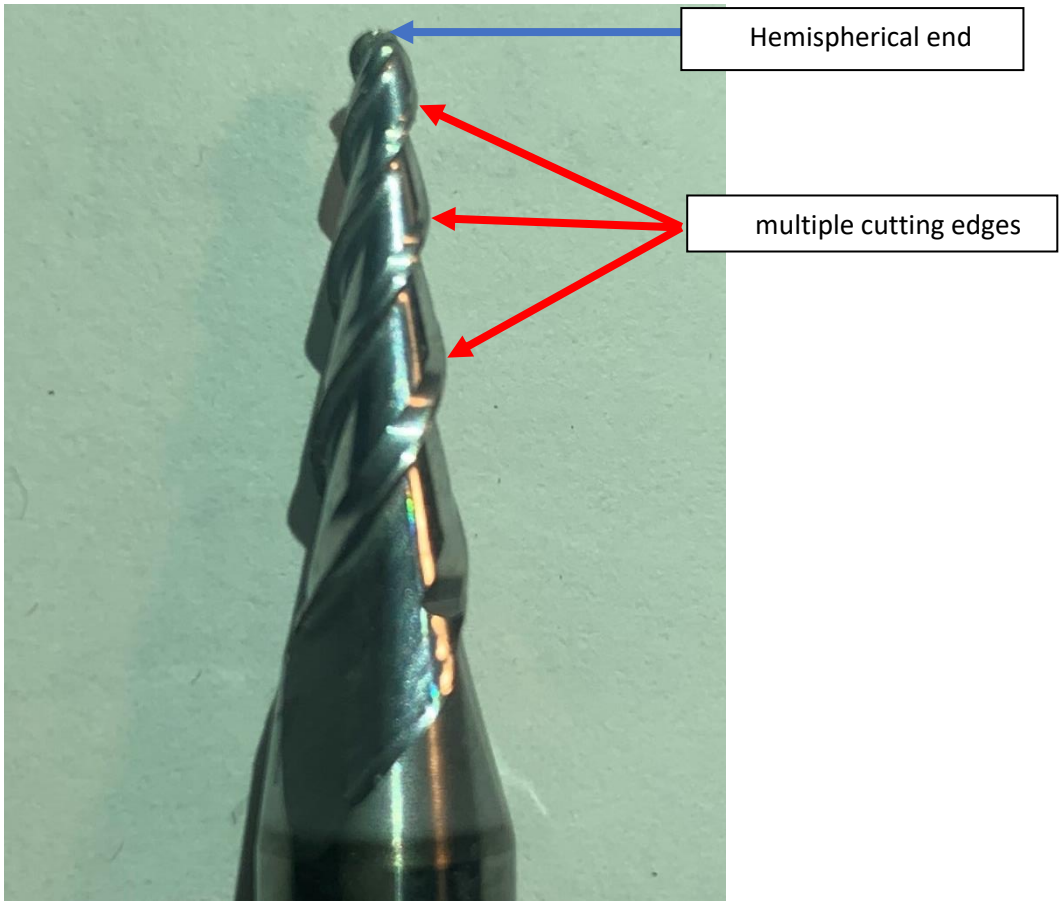

Figure 3. Example of a ball end cutter

A turbocharger's compressor wheel is an automotive component which used to be manufactured by casting. However, as Barrans et al. (2017) observed, this component is now often machined using 5 axis milling rather than casting because the casting process results in porosity and shrinkage issues In order to produce the compressor wheel using 5-axis milling, a ball end cutter must be used. The advantage of using a ball end cutter is that the hemispherical shape of the cutting edge does not collapse as easily as an that of an end mill cutter and it can cut continuously at all angles. The disadvantage of using a ball end cutter is that during the cutting process the cutting edge will leave step-over or pick-interval cusps and feed-interval cusps. Fig 4 shows a specimen of a turbocharger impeller machined by a ball end cutter in a 5-axis mill. It shows the pick-interval cusp marks are that located across the feed direction.

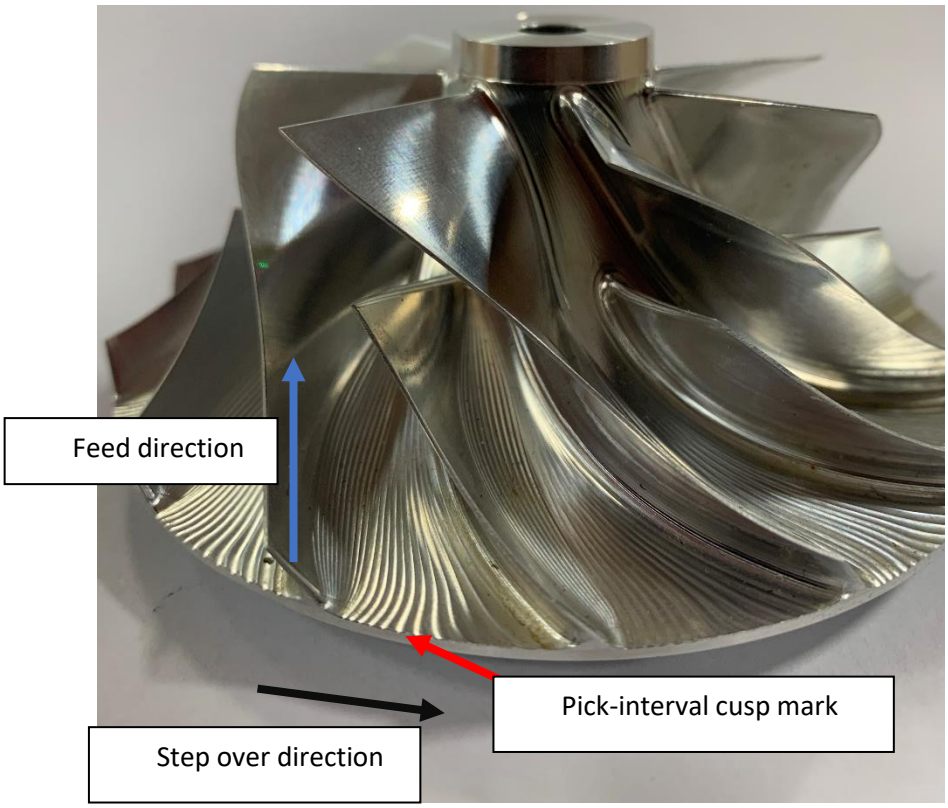

Figure 4. Detail of a turbocharger impeller

Fig 5 shows a stylised illustration of pick and feed-interval cusps on a flat surface. The height of the pick-interval cusp increases as the step over distance for each feed increases. Tunc (2019) also mentioned in their study that one of the factors that determines the surface roughness of the final cutting is step over distance. Feed rate and spindle speed are another two factors that can determine the surface roughness of the final cut. A higher spindle speed setting can cut more material during the machining process since the revolution of the tool is higher. The cutting tool turns further over the same distance of travel by comparison with a lower spindle speed. Ma et al. (2014) mentioned that different spindle speeds will influence the surface quality of the curved surface. A lower feed rate can also cut more material since the cutting tool turns more for the same distance travelled by comparison with a higher feed rate, also affecting the surface roughness. Feng and Su (2000) mentioned that a higher feed rate will lead to the feed-interval cusps being higher. Park et al. (1993) mentioned that

both feed rate and spindle speed determine the final surface roughness and machining time. In conclusion, higher spindle speed and lower feed rate generally gives a lower surface roughness.

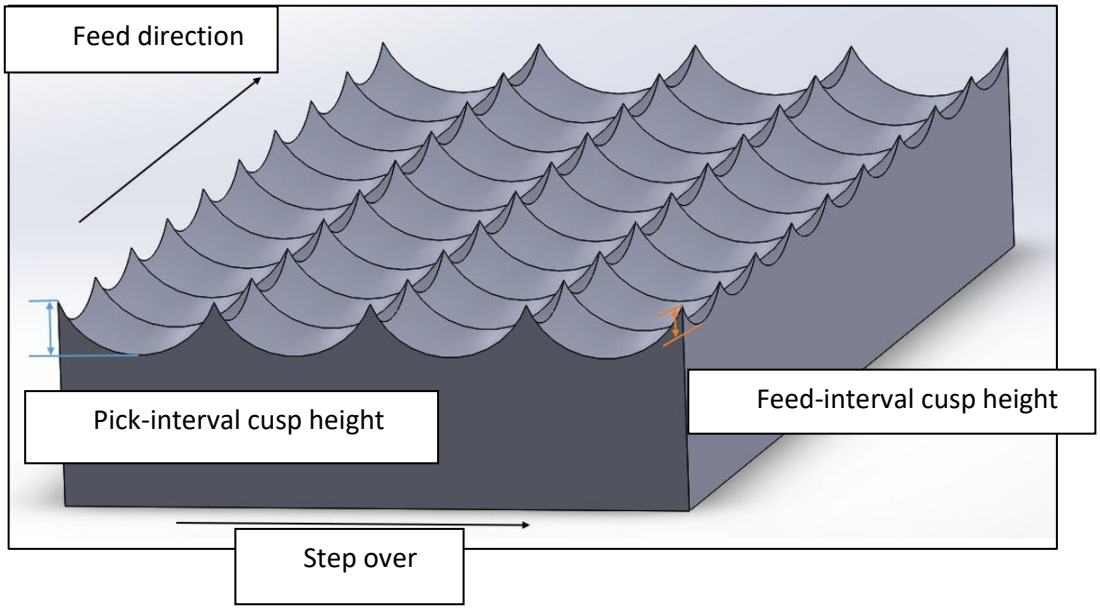

Figure 5. Illustration of Pick and Feed interval cusps height on a work piece

The parameters described above can affect the final surface result when using both 3 and 5-axis milling machines to shape materials. For 5-axis milling, the two orientations of the tool angle, the lead (φ) and tilt (ξ) angles illustrated in Fig 6, can also determine the final surface roughness. The lead angle is defined as positive in the feed direction. The tilt angle is defined as positive on the right hand side of the feed direction. Ju et al. (2015), Ozturk et al. (2009) and Baptista and Simoes (2000) used the same definitions for the orientation of the cutting tool.

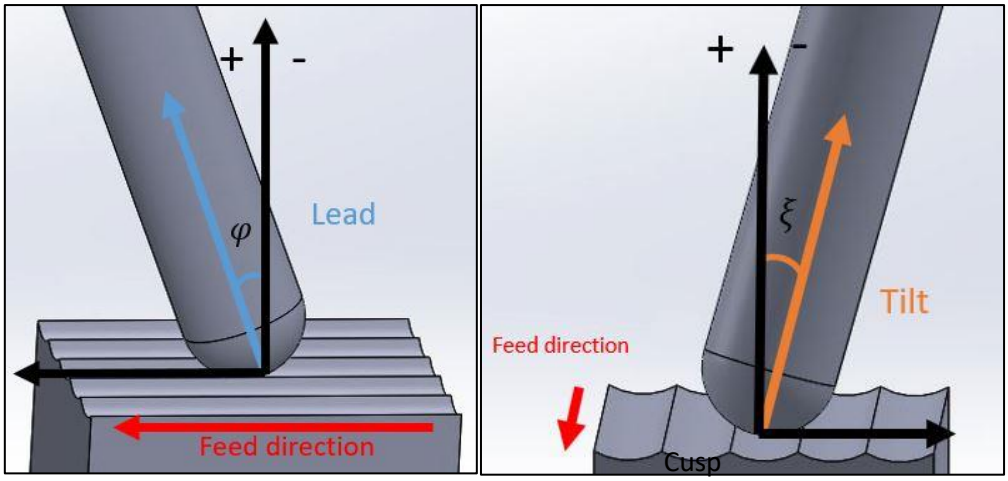

Figure 6. Illustration of lead(φ) and tilt (ξ) and tilt angle on a work piece

1.1.4. Impact of cutting parameters on surface finish

As mentioned in section 1.1.3, various cutting parameters can affect the final surface roughness in the milling process. Baptista and Simoes (2000) investigated the influence of cutting parameters on the surface finish. Their research used both 3 and 5 axis milling with end mill and ball end cutters. Their results showed that a better surface finish was achieved with 5 axis milling when using an end mill with a positive lead angle.

Chen et al. (2005) found that the feed-interval cusp height decreased continuously with increasing lead angle during their cutting trial. Ozturk et al. (2009) found that the tool tip generated tool tip marks when no lead or tilt angle was applied to the workpiece. Therefore, they asserted that the problem can be solved by applying a negative lead angle and confirmed their assertion by experiment using a 5 axis milling machine on Ti6Al4V. Layegh and Lazoglu (2017) investigated the use of different lead and tilt angles on aluminium. They stated that introducing lead and tilt angles of as little as 5° during the milling process resulted in the surface roughness of the tested area being less than with 0° of lead and tilt angle. Vakondios et al. (2015) investigated the effect of different levels of cutting parameter on the final surface roughness. The cutting parameters included step over, depth of cut, feed rate,

lead and tilt angle. They also discovered that changes in the lead and tilt angle affect the surface roughness.

In addition to the angle of the cutter, a few other parameters can affect the final surface roughness. Surface roughness results from the surface features identified in section 1.1.3, which have been investigated by a number of researchers. Khorasani et al. (2018) investigated the effect of various cutting parameters including feed rate, tool path and spindle speed on the roughness of finished surfaces. Gdula et al. (2018) concluded that their new strategy for generating simultaneous 5-axis tool paths with dynamic changes of lead angle relative to the curvature of the machined profile increased the accuracy of 5-axis machining of a turbine blade. Mersni et al. (2018) predicted that cutting speed, step over and feed per tooth were the parameters that affected the final surface roughness. They used a 25° inclination angle and oriented the cutter in one direction vertically upward. They also proved that by introducing an inclination between the cutter and the work piece, the result was better than with no angle of inclination. Yang et al. (2016) conducted an experimental study of the effect of using different tool axis lead and tilt angles on the titanium alloy TC17. They demonstrated that by introducing a negative lead angle with either a positive or negative tilt angle of the cutter, the final surface roughness improved or showed signs of decreasing. However, when the cutter was at a negative inclination angle, the final surface roughness increased.

1.1.5. Failure due to machining defects

Tool wear and defects can have a significant impact on the final surface produced by a milling process. Barrans et al. (2017) discovered that cusp marks near the impeller blade roots were stress raisers that led to fatigue failure during runs at speeds 5 % beyond the design limit. Investigation of the resultant fatigue failure showed that cracks were initiated at the machining marks. They concluded that the stress raising effect of the machining marks limited the lifetime of the wheel. Tabriz et al. (2017) discovered that the surface quality within the cusps can have a significant impact on the fatigue life

and durability of a component. Thakur and Gangopadhyay (2016) and Gómez-Escudero et al. (2021) both stated that the feed path in a particular area generated compressive residual stresses which reduced fatigue failure and prevented brittle fracture of a component. Wang et al. (2017) also agreed that surface defects created during 5-axis ball end milling can lower the fatigue life of steel components. Weimin Huang, Jun Zhao, Jintao Niu, et al. (2018) studied the fatigue performance of ball-end milled hardened AISI D2 steel and showed that by selecting a relatively high spindle speed a satisfactory combination of surface residual stress and microhardness can be obtained, which improves fatigue performance and machining efficiency. Weimin Huang, Jun Zhao, Ai Xing, et al. (2018) discovered that micro-scratches can develop into fatigue cracks and lead to fatigue failure of a component.

In this project, the hub of the turbocharger compressor wheel is cut by a ball end cutter. As mentioned previously in this section, the failure area is on the hub near the impeller blade root, since harder particles might appear to create a machining mark. Aluminium is the commonest material used to produce turbocharger compressors. However, machining aluminium will create segmented chips and a segmented chip can become aluminium oxide, i.e. corundum (Mohs' hardness 9) Zhao and Suhr (1992) which is harder than aluminium (Mohs' hardness 2.5) Sharma et al. (2015). This aluminium oxide can adhere to the cutting edge. Therefore, this phenomenon can create imperfections on the surface that potentially lead to a failure.

1.2. Aims

The aim of this research is to investigate the machining marks within a cusp on an aluminium specimen and develop a tool to predict the generation of these marks.

1.3. Objectives

- Undertake a literature review to determine the kinematic and kinetic factors that could affect the surface roughness of an aluminium work piece resulting from machining with a ball nose tool.
- Determine the current state of the art regarding the modelling of ball end cutting and the prediction and measurement of surface roughness.
- Create a kinematic model to simulate the cutting process. Other models used in research focus mainly on the overall roughness of the finished surface and the results are dominated by the pick interval marks. In this project, the model focuses on the effect of different cutting parameters such as lead and tilt angle on the feed interval cusp marks within the pick interval cusp mark. The results will be analysed.
- Use the results from previous cutting trials using a ball end cutting tool to determine the relationship between cutting parameters, tool edge degradation and within cusp scratch marks. Carry out 3D optical surface measurements to investigate the surface roughness and feed interval marks.

  Validate the results of simulation using experimental results. Extract data from both the experimental results and simulation analysis and adjust both results for comparison.

1.4. Motivation

The motivation of this project is the study of the fatigue limit of impeller blades by Barrans et al. (2017) as described in section 1.1.5. Their results show that the failure area is around the cusp and that the stress raiser is within the cusp area. Therefore, marks within the cusp are more likely to initiate crack propagation. In order to investigate fatigue failure, a model to simulate the marks within the cusp is required.

1.5. Summary

The major aim of this research is to investigate the feed marks within the cusp and develop a model to simulate the surface with different cutting parameters such as the helical ball end effect, lead and tilt angles. The structure of this thesis is as follows:

- Chapter 2 - A literature review of the current state-of-the-art of experimental 5-axis milling using different methods, models developed by various researchers and result validation, kinetic investigation, ball end cutting edge, the prediction of the cutting tool position, the surface roughness and the surface inspection, the filtration and form removal and the sampling theorem. Consider the current state-of-the-art and determine the missing parts of the model for later development.
- Chapter 3 - Develop an initial theoretical calculation for the cutting model to simulate 3-axis single and multiple cutting edges with a straight cutter. Incorporate the theory into MATLAB to generate a point cloud to simulate the locus of the cutting edge. However, this model will not include the lead and tilt effects of 5-axis milling.
- Chapter 4 – Introduce additional cutting parameters including lead and tilt angles and helical cutting edges into the model to simulate the effects of 5-axis milling. This model with all the parameters has a relatively long run-time and the resolution is not ideal for filtration and visualization of the resulting surface. Therefore, it must be optimised.
- Chapter 5 – Model improvement including justifying the number of time increments per revolution and cutting-edge model segments, reducing the computing time, filtering the cutting locus into a surface and profile, and validating the results.
- Chapter 6 - Carry out surface inspection of various cutting specimens prepared by a previous researcher. The results are dominated by the pick interval cusps, which is not the

focus of this project. Therefore, several filtration methods to remove the pick interval marks have been conducted to investigate the feed interval marks.

- Chapter 7 – Conclusion of the project and suggestions for further research.

2. Literature review

2.1. Experimental investigation of 5-axis milling

Many researchers such as Hauth et al. (2011) & Gray et al. (2003) have looked at how cusp marks are created by ball end cutters at the macro scale on various materials such as stainless steel, copper and aluminium. The macro scale (cusp formed) surface finish of samples machined using ball end cutters has been investigated widely. Most researchers have focussed on the height and width of the cusp, and the overall surface roughness. P. Yang et al. (2016) established a series of cutting experiments using a carbide ball end cutter on a Titanium alloy TC17 workpiece. The results demonstrated that the surface roughness (Ra) was lessened by applying lead and tilt angles during the cutting process, especially for lead angles between 12° and 60°. Chen et al. (2019) established a series of cutting experiments using a solid carbide ball end cutter on steel. The results showed that the surface roughness can be minimised by applying a small lead angle. Buj-Corral et al. (2012) analysed the effect of different combinations of cutting parameters, such as the feed per tooth, spindle speed and radial depth on areal surface roughness parameters, such as the average roughness (Sa). They concluded that a sufficiently low radial depth of cut or a low feed rate can minimise the feed-interval cusp height. Tabriz et al. (2017) also investigated the effect of using a ball end cutter with different combinations of spindle speed, feed rate and lead angle when cutting in the push direction. The result showed that higher spindle speeds resulted in lower surface roughness values unless the cutter lead angle was greater than 50°, at which point tool vibration became a significant factor. Wojciechowski et al. (2017) also carried out an experimental investigation of the influence of cutting parameters, tool run-out and deflections induced by the cutting force for a 5-axis milling machine with hardened steel. Their result showed that the lead angle influences the surface finish significantly. The tool life can be improved and cutting forces minimized by applying a lead angle of 15° with a feed rate of 375 m/min. J.-S. Chen et al. (2005) found that the feed marks have a greater impact on the surface roughness than the cusp marks during high-speed machining. The results of this study showed that the feed marks were 3-4

times higher than the cusp marks when cutting with a high feed rate and the cusp height decreased continuously when the tool lead angle was increased. A lead angle of up to 10° is sufficient to create lower surface roughness values than with a 0° lead angle for most diameters of ball-end tool. Gdula (2020) carried out an experimental investigation of the effect of using different tool orientations on variable curvature surfaces on a turbine blade. Their results showed that increasing the lead angle across the entire surface can reduce the average surface roughness (Ra) and the peak and valley difference value (Rz). Lizzul et al. (2021) presented a paper to investigate the difference between three sets of lead angle when machining a titanium alloy workpiece. They found that cutting with a 15° lead angle required the highest cutting force but gave a smooth and clean surface, a 45° lead angle cutting required a low cutting force but created tool marks, and a 75° lead angle cutting required a low cutting force and resulted in low surface roughness. However, the 75° angle induced tool deflection. Han and Zhao (2010) conducted a study of the effect of the lead angle during the machining process on the surface quality of potassium dihydrogen phosphate (KH_2PO_4) crystals cut using a micro ball-end cutter. Their study suggested that a 45° lead angle resulted in the lowest surface roughness for a micro ball end cutter cutting KDP crystal. Shan et al. (2016) conducted a study to investigate the optimal lead angle to minimise the deformation and cutting force for thin-walled freeform surface parts. Their experimental results showed that when the lead angles are between 15° and 45°, the milling force and deformation of the workpiece were the least. Yigit and Lazoglu (2015) analysed the effects of lead and tilt angles on the 5-axis ball-end milling of flexible freeform aerospace parts. Their conducted a set of experiments in which the tilt angle was varied between -25° to + 25° and the lead angle between -25° to +15° in 5° increments. The results showed that the best surface roughness was achieved with a -2° lead angle and 10° tilt angle. In this tool orientation, the tool tip marginally avoided any ploughing effect from the cutting. Biermann et al. (2010) established a model consisting of an FE model of the turbine blades to simulate the results of milling. This model transforms the movement of the workpiece into tool movements to simulate the machining process and generate the surface result. Ozturk and Budak (2007) calculated the relationship between the ball end tool radius and the tilt angle

in order to avoid leaving tool tip marks from the previous feed-interval cusp. Wang et al. (2016) investigated the tilt angle effect during the machining process. The result showed that the general surface roughness decreases significantly by increasing the tilt angle from 0° to 5°. The lowest surface roughness value generated at 10° tilt angle. From 10° to 30°, the surface roughness increases slightly.

2.2. Kinematic prediction of the surface result

Chen et al. (2005) undertook a study to predict the pick-interval and feed-interval cusps. They developed a cutting model based on a cutter with two straight flutes. By using a coordinate system with the origin at the centre of the hemispherical end of the cutter, they could define the depth to which the cutter was immersed in the work piece. Subsequently, they added the rotational spindle speed and time into a matrix function to simulate the kinematics of the cutting process. Ozturk et al. (2009) also conducted a similar study of the effects of lead and tilt angle in 5-axis ball end milling processes. This simulation not only focussed on the effect of applying the tilt angle during the cutting process, but also on the ploughing effect resulting from the lack of cutting effect at the tool tip, and the cusp height associated with the step over length when using a ball end milling cutter. The results of the simulation were validated by a series of cutting tests. This study also proved that increasing the tilt angle could reduce the pick-interval cusp height relative to a zero tilt angle. Also, the step over length could be increased to achieve the same pick-interval cusp height as with a zero-tilt angle, with fewer steps. Further, they also affirmed that the ploughing effect could be avoided by increasing the tilt angle or reducing the cutting depth. This was supported by a set of calculations to simulate how the tool tip cut the material at different tilt angles and cutting depths over several feed passes, in order to show the resulting surface. This phenomenon arises because the particular tilt angles associated with the step over can cut out the previous tool tip mark. Layegh and Lazoglu (2017) conducted a similar analysis of 3D surface topography using a 5-axis ball end milling machine. They developed a method to predict the surface texture and roughness based on their model using MATLAB

R2015b which did not include any real-life conditions such as tool vibration and imperfections in the cutter. They used a different method to define the motion of the cutter during the cutting process, since they simulated a swept cutter edge. Their model was based on the feed coordinate frame rather than the tool coordinate frame. They focused on different combinations of lead and tilt angle and obtained the resulting 3D average roughness (Sa) and 3D root mean square roughness (Sq) value. The results of the simulation were verified experimentally with an average prediction accuracy of 20%. However, the simulation considered the cutter, tool holder and the work piece to be rigid bodies. Therefore, when the lead and tilt angles were higher, the cutter and the work piece encountered more vibration which affects the accuracy of the results. Lavernhe et al. (2010) carried out a simulation to predict the 3D surface topography in 5-axis milling using a filleted end cutter. Their model is based on the material removal simulation technique known as the N-buffer method. This method creates discrete parallel lines or spikes along the z axis, and the cutter generates a volume which truncates the spikes. The part of those lines that remains presents an approximation of the surface finish. The model results showed that lead angle is the most significant factor that influences the final surface pattern. Denkena et al. (2015) compared the kinematic topography from the machining simulation with the stochastic topography based on empirical data. This study used material removal simulations (MRS) similar to those by Lavernhe et al. (2010). In the model, the work piece is represented by voxels, dexels or solid modelling techniques such as constructive solid geometry to simulate the material cutting process, and it simulates material removal as the cutter traverses the work piece. Each simulation takes considerable processing time, but the MRS takes into consideration most of the kinematic factors of the process alongside an empirical model to create a more realistic result. The result of the kinematic model incorporates the previous experimental result of the stochastic effect on the surface. The combined result shows that the wall shear stress is distributed irregularly and depends on the local surface shape. However, the wall shear stress using the kinematic surface model alone was homogeneously distributed and only increased at the peak of the milling paths. Quinsat et al. (2011) conducted similar research to model the result of 5-axis milling with a filleted end cutter.

The result of the model showed that both lead and tilt angle can significantly affect the final surface quality. Zhang et al. (2017)& Ghorbani and Movahhedy (2019) both developed a similar CWE (cutter/workpiece engagement) model to simulate the surface results using different tool orientations and cutter runouts on different geometric surfaces. Their models are supported by a set of experimental pieces cut using different step over values, different curvatures of the surface combined with different lead and tilt angles.

2.3. Kinetic investigation

All the above studies did not consider real-life factors such as tool vibration, cutting edge chips and adhesion. However, stochastic influence is also a factor that affects the surface result. Therefore, a study done by Sun and Guo (2011) investigated the effect of run-out on 5-axis milling by executing two sets of experiment, the first set using different feed rates and spindle speeds with a 0° tilt angle, the second set of experiment using different feed rates and spindle speeds with tilt angles of 0°, 20° and 50°. By combining the results of these two experiments, a method to predict the cutter run-out effect was developed. Wojciechowski et al. (2016) also carried out an experimental investigation of the influence of cutting parameters, tool run-out and deflections induced by cutting force on a 5-axis milling machine with hardened steel. This experiment applied different feeds per tooth, axial and radial depths of cut. They concluded that geometrical errors and dynamic deflections are induced by radial run-out and caused by forces generated during the machining process. Wang et al. (2019) developed a model to simulate the surface topography resulting from 5-axis milling with a ball end cutter, taking tool and workpiece vibration into consideration. Their model took tool vibration and the trajectory of the cutting edge into consideration to analyse the surface topography, and also added workpiece vibration as the low rigidity of thin-walled parts can create vibration during milling. The model has been validated by a series of experiment on a 5-axis milling machine with a ball end cutter. As a result, their model has a 15% difference between the experimental and simulated results, the

main difference arising from random noise during the cutting process. Wang et al. (2015) studied a cutting force prediction algorithm that considers the effect of cutter vibration and cutter run-out. Han et al. (2009) proposed a cutting model with a dynamically changing feed rate, as a curved workpiece surface can affect the feed rate because of the drive limits of the machine tools. Their model incorporated the influence of elements including the surface of the workpiece, shape of the ball-end cutter, path interval and tool orientation. Experimental testing was conducted to verify the accuracy of the model result. Bo et al. (2017) developed a model to simulate the surface result of 5-axis milling using a ball-end cutter. Their model can generate a surface result which includes the effects of locating errors, spindle errors, geometric errors of the machine tool and cutting tool deflection.

2.4. Cutting edge profile

While many researchers have investigated the effect of using 3 or 5-axis milling with a ball end cutter, cutters with a helical cutting edge profile have been investigated less often. Denkena et al. (2021) proposed a method to predict surface defects by considering the minimum chip thickness within a virtual process design. Their experimental result used a ball end cutter with helical cutting edges but their prediction model used straight cutting edges. Buj-Corral et al. (2012) and J.-S. Chen et al. (2005) both used straight cutting edges in their models to predict the surface roughness in a 5-axis milling process. Their model concluded that a higher feed rate will lead to greater surface roughness.

Some researchers have investigated cutting edges with a helical profile. Nespor et al. (2016), developed a model to predict the general surface machined by a ball end cutter with helical cutting edge. The prediction result showed that applied a small lead angle during the machining process can decrease the effect of tool deflection and tool runout. Ryabov et al. (2018) investigated the constant cutting geometry of a ball end cutter with curved cutting edge. The result showed that a curved cutting edge can machine a flat workpiece with a constant surface roughness, but the surface roughness changes over a complex workpiece profile. Weijian Huang et al. (2018) developed a model that

simulated a helical cutting edge on a ball end cutter to estimate the cutting force at different lead angles. The result showed that the model prediction matched the experimental result in all three directions on the surface. Dai et al. (2019) also carried out similar research to calculate the helical profile and incorporated that into their model to estimate the cutting force with different lead and tilt angles. Layegh and Lazoglu (2017) developed a model using a helical profile to simulate the general surface of 5-axis milling.

2.5. Methodology of predicting the tool position

A conventional 3-axis milling machine has a simple definition of the tool coordinate system: x, y and z axes. However, it is insufficient to use x, y and z axes alone to define the tool coordinate system on a 5-axis milling machine as the raw material, the feed direction and the tool position all require different coordinate systems to represent them. There are three coordinate systems used by many researchers, a global coordinate system (GCS), a raw material, feed, cross-feed and normal system (FCN) and a tool coordinate system (TCS) as shown in Fig 7. GCS is aligned with the machine axes. The origin will be a fixed point relative to the machine structure and defined by the user. This coordinate system is then translated to create the FCN with its origin at the tip of the tool. The FCN origin at the tool tip coincides with the TCS origin. This coordinate system contains feed (F), cross feed (C) and normal (N) axes which is a moving coordinate system, also known as process coordinates. TCS is a coordinate system that contains the u, v and w axes and represents the tool. The w axis is coincident with the tool axis. This coordinate system depends on the lead and tilt angle specified by the user to determine the position of the tool. Therefore, the u, v and w axes may not always coincide with the f, c and n axes.

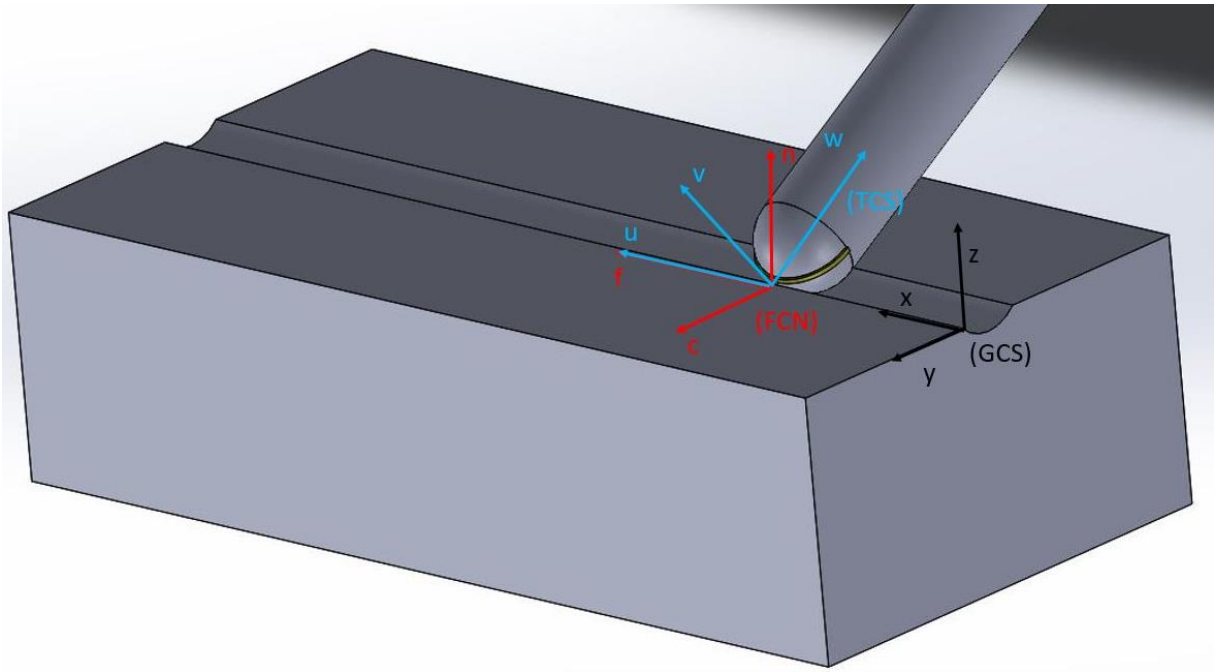

Figure 7. Illustration of coordinate systems

Song et al. (2017) used these three different coordinate systems to represent the tool position in their model to predict the cutting force in a multi-axis milling process. Tunc and Budak (2009) used the FCN system to define the tool position in their model to predict 5-axis milling on smooth free-form surfaces. Bandila et al. (2017) used the same FCN system in their model to predict the cutting force acting on the tool.

In order to define the tool position to predict the final cutting surface, Chen et al. (2005) used a similar coordinate system to define the cutter motion and the cutting edge. Their study used a coordinate system based on the midpoint of the cutter as the origin associated with the radius of the cutter to identify the cutting edges. The cutter is tracked using the TCS with the rotational speed and time. This study also used an additional coordinate of the lead angle relative to the surface to simulate the lead effect. However, this study did not describe how to transfer the path of the cutting edges onto the final surface. Ozturk et al. (2009) mentioned that they used the TCS to identify the tool inclination orientation, associated with the feed rate and spindle speed, to calculate the distance between each

feed mark and determined the feed-interval cusp height and ploughing effect. However, this method does not simulate the continuous motion of the cutter. It can only reflect the feed-interval cusp height and demonstrate the ploughing effect of the tool tip, if any. Layegh and Lazoglu (2017) identified the position of the cutting edge at each discrete point by using the rotational angle of the tool, local helix angle, total number of cutting edges, number of current cutting edge and tool radius. Their model produced a result for cutting edge motion without any lead or tilt effects at this stage. However, they did not describe how they incorporated tool orientation into their model to obtain the resulting final surface including the lead and tilt angle effect. Zhang et al. (2017) established a model based on calculating the B and C axes to find the tool orientation. They added this calculation into the tool geometry coordinate in a manner similar to Layegh and Lazoglu (2017) to determine motion of the cutting edge. Wang et al. (2021) established a model similar to Zhang et al. (2017) but used the A and C axes to define the rotary axes.

2.6. Surface roughness parameters

Surface roughness is an important parameter when defining the quality of cutting. This parameter determines how the surface reacts to the environment and to other surfaces. A rough surface can lead to crack propagation. One of the most commonly used parameters is the arithmetic mean surface roughness (Ra). The definition of arithmetic mean surface roughness is given by ISO 4287:1997, and is a parameter that describes the deviation of a surface from an ideal level. Bhardwaj et al. (2014) developed a model to predict the surface roughness resulting from cutting AISI 1019 steel specimens. This research also used Ra as a parameter to measure an AISI 1019 steel specimen and discovered a linear relationship between cutting speed and roughness. An experiment was carried out and the resulting Ra used to validate the predicted result. Khare and Agarwal (2015) provided a similar approach to establish a model using Ra for a grinding surface to predict the surface roughness and validate it experimentally. Kittali et al. (2022) used Ra to compare the results of machine cutting with

and without coolant. Another parameter that some researchers have used is arithmetical mean height (Sa). Nwaogu et al. (2013) carried out research into the surface roughness of two standard roughness products from the foundry industry and compared them with cast surfaces. They also compared the difference in results between a non-contact technique using a 3D optical system with the Sa and Ra result, and also compared the result using a stylus instrument. They concluded that the 3D surface parameter result reflected the surface more accurately and precisely than 2D parameters.

In this project, another surface parameter that we have used to describe the surface is the maximum height (Sz) . This parameter can be defined as the sum of the maximum peak height value and the maximum valley depth value. Nakatani et al. (2019) used Sz to investigate the effects of surface roughness on the fatigue strength of Ti-6A1-4V alloy manufactured by additive manufacturing. They compared the Sz result for two additive manufacturing techniques, electron beam melting and direct metal laser sintering. Cai et al. (2018) also used Sz to study the surface of 316L stainless steel machined by nanosecond pulsed laser since their study focused on characterisation of the hydrophobicity of surfaces with Gaussian holes.

Other parameters mentioned in this report include core height (Sk) and reduced valley depth (Svk), Core height (Sk) can be defined as the difference of height between 40% of the areal material ratio from the linear equivalent curve KEYENCE (2024a). Reduced valley depth (Svk) can be defined as the arithmetical mean of the reduced valley depth of the areal material ratio curve, and also is a measure of the valley depth below the core roughness (KEYENCE, 2024b).

2.7. Alicona infinite focus measurement

As mentioned in section 2.6, surface roughness is an important parameter that determines the reaction of the workpiece surface. The Alicona Infinite Focus Measurement G4 is a machine that has been used widely to inspect surfaces in many applications. This machine captures an image of the

surface and analyses the depth of field by varying the focus. Since the microscope camera of the machine can only move horizontally, the machine can only produce areal results. Seid Ahmed et al. (2017) used this machine to study the wear of coated and uncoated tools by comparing the volume of the tools before and after the cutting process. Walton et al. (2015) used the Alicona IFM to investigate Titanium samples and obtained the surface core height (Sk) and reduced valley depth (Svk). They used the result to characterise the finished surface of samples and to provide guidance for further investigation to improve the surface quality, specifically in a civil aeronautical compressor. To achieve the desired resolution, the whole area was divided into 400 fields (20x20 grid), each scanned individually. The individual images were then overlapped until the height value of each pixel matched. This area stitching process required approximately 10% overlap. Polishetty et al. (2017) also used the Alicona IFM to scan the cutting insert's flank and rake face areas for wear analysis. They used a scan of the new cutting edge insert as a reference to compare with the scan of the worn edge. The differential analysis function of the machine's software was used to superimpose the two scans to evaluate the tool wear. Bandila et al. (2017) used the Alicona IFM to measure the cutter edge radius, tool wear and the final surface roughness. The result was that there is a noticeable difference between the actual values of edge radius and the corresponding nominal edge radius. P. Wang et al. (2017) used the Alicona IFM to measure an electron beam melting specimen to visualise the surface topography of multispot and non-multispot melting and concluded that multispot melting produced greater surface roughness but better dimensional accuracy. Nwaogu et al. (2013) used the Alicona IFM to measure cast components to measure the surface roughness of two selected standard roughness comparators used in the foundry industry. They recommended that a 5x microscope gives a more reliable result than a 2.5x microscope.

2.8. Filtration and form removal

Filtration and form removal are two of the most important factors in the methodology of surface studies. Errors and artefacts always occur during the inspection process, and forms appear on the specimen that are sometimes not relevant to a particular study and must be filtered and removed. Therefore, I review filtration and form removal. Leach (2013) explains that filtration is a function to divide the measured data into different scales of interest. Muralikrishnan and Raja (2009) stated that the Gaussian filter is one of the filters most widely used for surface metrology and is identified within the international standard (ISO 16610-21:2011). This filter has a 50% transmission at the cut-off wavelength so that the short and long wave portions of the surface profile are separated and can be reconstructed without altering the surface profile (ISO16610-21 (2011)). It has been defined as one of the standard filtering techniques for profile analysis by Podulka (2018). Leach (2013) stated that this filter is known to determine a weighted moving average and can be used in individual cases such as freeform surfaces to eliminate the nominal form. However, Muralikrishnan and Raja (2009) stated that this filter has the drawback that as it is not robust, a large peak or valley will be distorted and affect the final measured surface roughness.

Wavelet transformation is a method which avoids the distortion created by the Gaussian filter. Whitehouse (2010) stated that wavelet transform method decomposes a surface profile into a set of basic wavelets and breaks down a signal into sinusoids of different frequency. Chen et al. (1999) stated that this analysis technique is applied extensively in image processing, pattern recognition and some non-linear subjects, and it can be used to isolate and further evaluate the characteristics of surface structures. In this study, a wavelet analysis function within the software package SurfStand has been used. The software allows the user to select from an automatically generated wavelength range to extract relevant data. Blunt and Jiang (2003b) investigated this software and it calculates the longest (form) and shortest (roughness) wavelength frequency on the surface, and then divides the range into 8 levels and allows the user to choose the levels. However, this method only applies to a certain range of wavelengths, and the user cannot choose the precise maximum and minimum width of the wavelength window.

The next method which can 'void' the restrictions of the wavelet transform method, is polynomial fitting. Fan and Gijbels (1995) stated that this is a smoothing method to filter the data to produce the required data. The advantages of using this method include there being no need to modify the boundary on the surface; it can be applied to various design situations. The disadvantage of using this method is that it is difficult predict the outcome of the fitting procedure; many trials may be required before the system can create an appropriate result (Keren and Gotsman (1999)).

Finally, the form removal function aims to remove the basic surface shape but leave other features of the surface unaffected. This does not distort the surface like the previous methods. Duval-Chaneac et al. (2018a) used this function to remove the cylindrical form of a measured surface, leaving a flat surface ready to be analysed for surface roughness and shown in Fig 8.

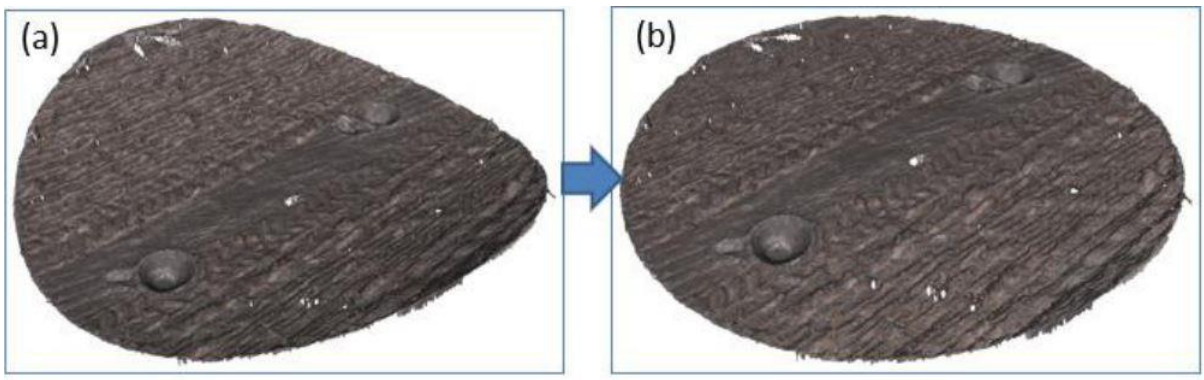

Figure 8. Cylindrical form removal example from Duval-Chaneac et al. (2018a)

Duval-Chaneac et al. (2018b) inspected the surface of maraging steel 300 moulded by selective laser melting. They also used the form removal function to flatten the cylindrical surface.

The studies described above demonstrate that a cylindrical or other surface form can be removed using various functions of diverse software packages. However, the forms removed were simple prismatic shapes such as a cylinder. There does not appear to be any application where forms at two or more levels have been removed. For example, this removal technique still cannot completely

remove an incomplete cylindrical form with rough edges to investigate micro marks within the form. Therefore, all the above methods were used in this study to determine the one most suitable for investigating machined surfaces. Also, further study is required to develop a more comprehensive way to investigate the marks within cusps on the machined surface.

Another software package used in this project is SURFSTAND, which was developed to study surface metrology by researchers at the Centre for Precision Technologies (CPT) in the University of Huddersfield and Taylor Hobson. According to Blunt and Jiang (2003a), the software aims to use mathematical techniques to measure surface textures accurately, and also to inform standards bodies of the potential for a new international standard covering the field of 3D surface characterisation. The software can handle various surface filtering techniques, such as Polynomial filtering, Gaussian filtering, Wavelet filtering etc.

2.9. Nyquist Shannon sampling theorem

The Nyquist Shannon sampling theorem connects discrete-time signals and continuous-time signals. It determines the sampling rate that allows a discrete sequence of samples to capture all the information contained in a continuous signal of finite bandwidth. Therefore, in order to represent the data accurately, an adequate sample frequency is required. Shannon (1948) studied the bandwidth and number of relays and discovered that twice the highest frequency (vb) of the analogue signal can avoid aliasing errors. Ficker and Martišek (2015) also mentioned that the discretisation must be performed with a sampling rate (vs) that is at least twice the highest frequency (vb) of the analogue signal according to this theorem. Li et al. (2006) agreed that the sampling rate needs to be twice the highest frequency, otherwise the reconstructed sample will suffer from aliasing errors. Por et al. (2019) & Lévesque (2014) explained the result of insufficient-sampling and sufficient sampling. If the sample frequency (blue line) is less than twice the analogue signal frequency (orange line), the signal is insufficient-sampled as shown in Fig 9. Here, the sample frequency has less than two samples per

sinusoid cycle of the original signal and there is not enough data to reconstruct the original signal. If the sample frequency (blue line) is two or more samples per sinusoid cycle of the original signal (orange line), the signal can be reconstructed perfectly as shown in Fig 10.

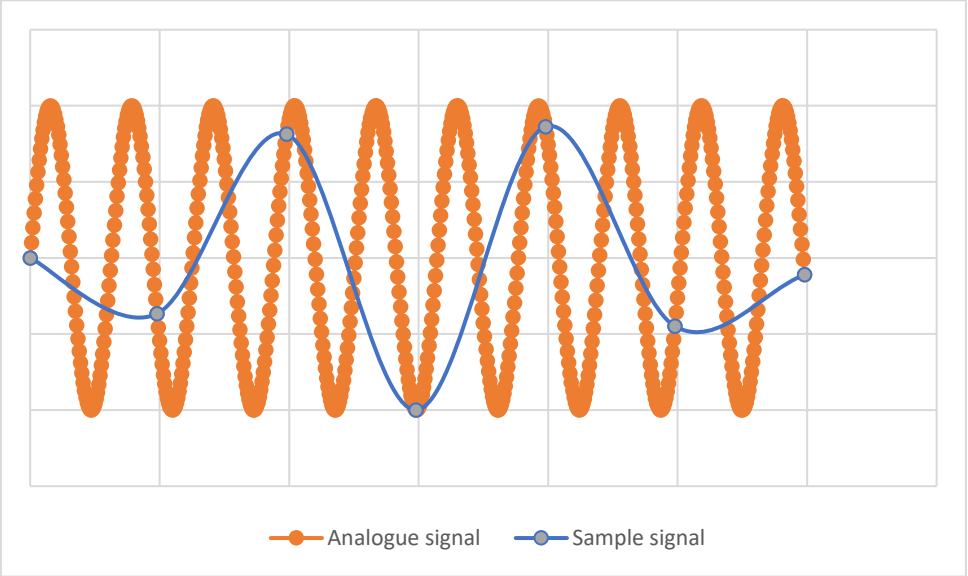

Figure 9. Insufficient sampling frequency

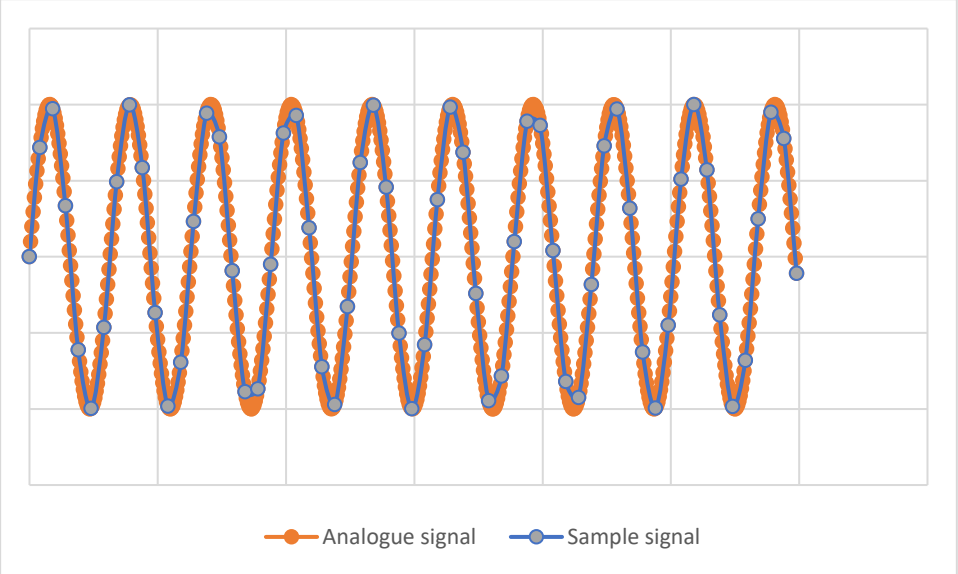

Figure 10. Sufficient sampling frequency

Zamaruiev (2017) applied this theorem to convert the original data into a digital signal for an electric power converter. The study concluded that for some applications it is necessary to use a sampling frequency greater than twice that of the original signal to avoid error. Romo-Cárdenas et al. (2018)

determined the window size parameters for bio-optical signals. They also established how to calculate the window size supported by the Nyquist Shannon sampling theorem. Devi and Pugazhenthi (2016) adopted this theorem to convert audio samples into a digital waveform and they concluded that the sampling rate given by the Nyquist Shannon sampling theorem is a perfect sampling rate for their application. This study helps the model development in section 5.2.2 to avoid any error occur in the final surface result of the model in both x and y direction.

2.10. Aluminium milling problems

Milling defects in aluminium can be created by several mechanisms including the use of coolant during cutting and chips segmentation. Cagan et al. (2020) investigated the effect of the high-speed milling of Al7075-T6 aluminium alloy on the surface quality under dry and minimum quantity lubrication (MQL) conditions. Ther result showed that the Ra value was higher in the cutting experiments with the dry environment than with the MQL environment because the heat generated by MQL is more easily discharged. Sreejith (2008) conducted a similar study on 6061 aluminium alloy under dry, MQL and floored conditions. The result demonstrated that the MQL cutting condition created a lower Ra value compared to the dry cutting condition because the coolant acts as a lubricant and lowers the cutting force during cutting. Pham et al. (2020) carried an experiment on high-speed face milling of A6061 aluminium alloy under dry cutting condition. This study demonstrated that chip material adheres to the cutting edge after milling, leading to unwanted scratches on the surface. Haddag et al. (2016) investigated the cutting force, chip segmentation and formation of a built-up edge when machining aeronautical aluminium alloy AA2024-T351 under dry conditions. The orthogonal cutting experimental result showed that a lead angle of 15° generated a lower built-up edge effect than 0° lead angle. This is because the work material flows less easily in a low lead angle machining condition.

2.11. Conclusion

The literature review can be summarised in the following areas.

- Pick-interval and feed-interval cusp marks in 5-axis milling have been investigated in many studies. Parameters such as feed rate, tool diameters, lead and tilt angles have been investigated through experiment and simulation. However, the final surface and surface roughness of 5-axis milling with a ball end cutter with a helical cutting edge has not been simulated.
- Kinematic prediction of the surface has been investigated widely in many studies. Models used to simulate the final milled surface have mainly used the N-buffer method but not the actual cutting edge locus with filtration to simulate the surface.
- Ball end cutters have commonly been used in 5-axis milling with both straight and helical cutting edges.
- GCS, FCN and TCS are commonly used in many studies to indicate the position of the cutting tool and the work piece.
- Ra and Sa are the two most commonly used parameters to represent the surface roughness in different studies.
- Feed-interval cusp marks always dominate the surface roughness parameter and the micro marks within feed-interval cusp marks have usually been ignored. Also, a study of the surface roughness within pick-interval cusp marks is absent.

3. Initial model

Some of the work presented in this chapter has previously been reported in Chan and Barrans (2021).

3.1. Single cutting edge and rotation movement

The first step in developing a cutting model is to use single cutting with no lead or tilt angle. This step requires several assumptions to support the development of this model as follows:

- There is a single straight cutting edge, as shown in Fig 11
- The u direction of the tool is parallel to the x direction (feed direction)
- The cutting edges are not subject to any tool wear or abrasion
- The machine does not create any vibration during the milling process

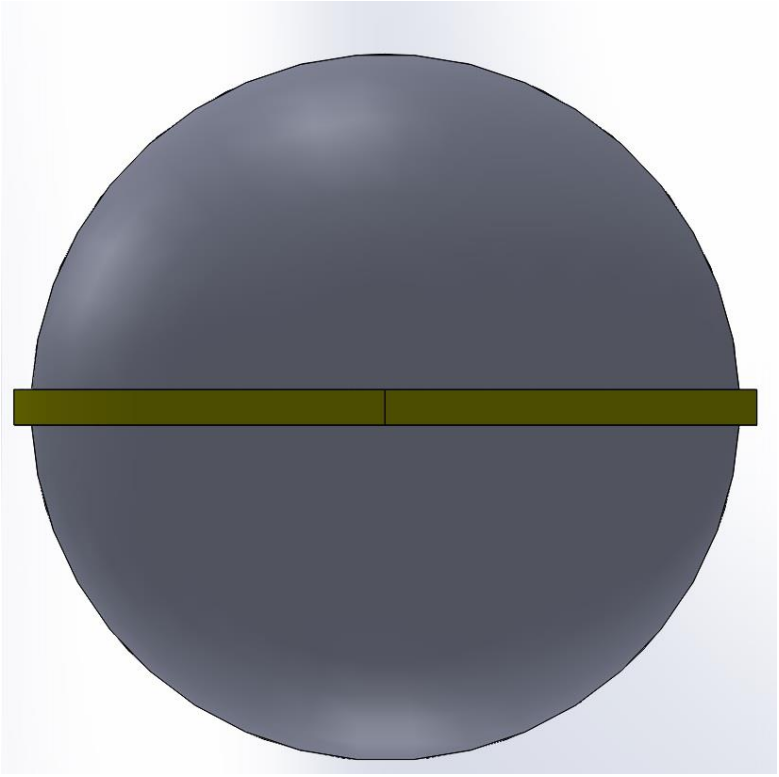

Figure 11. End view of tool showing the cutting edge

In order to simulate the cutting motion, an origin (0) is defined at the tool tip with zero lead and tilt angles at time = 0 as shown in Fig 12.

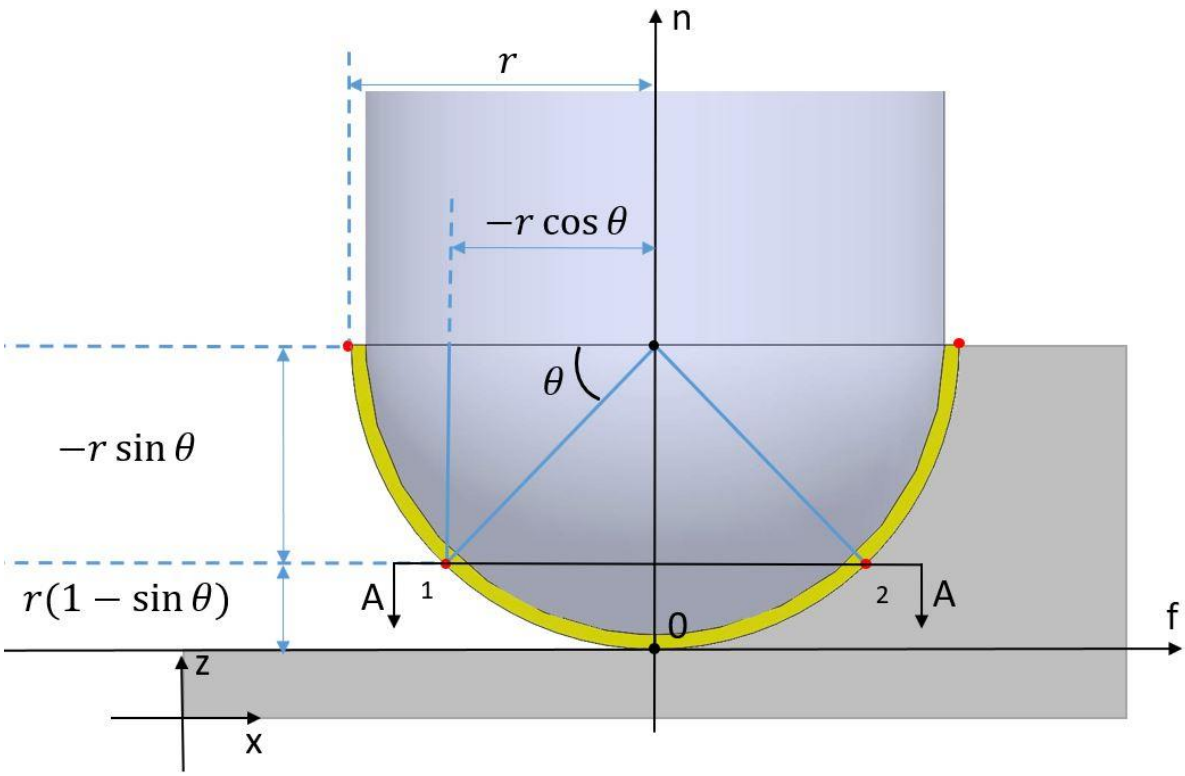

Figure 12. Side view of the cutter as it approaches the work-piece

The section A-A in Fig 13 shows how the cutter moves from the position in Fig 12. Point 1 moves to position 1' during time t. This results from the angular displacement (ωt) determined by the spindle speed ω and the translation, ($f_x t$) resulting from the feed rate (f_x).

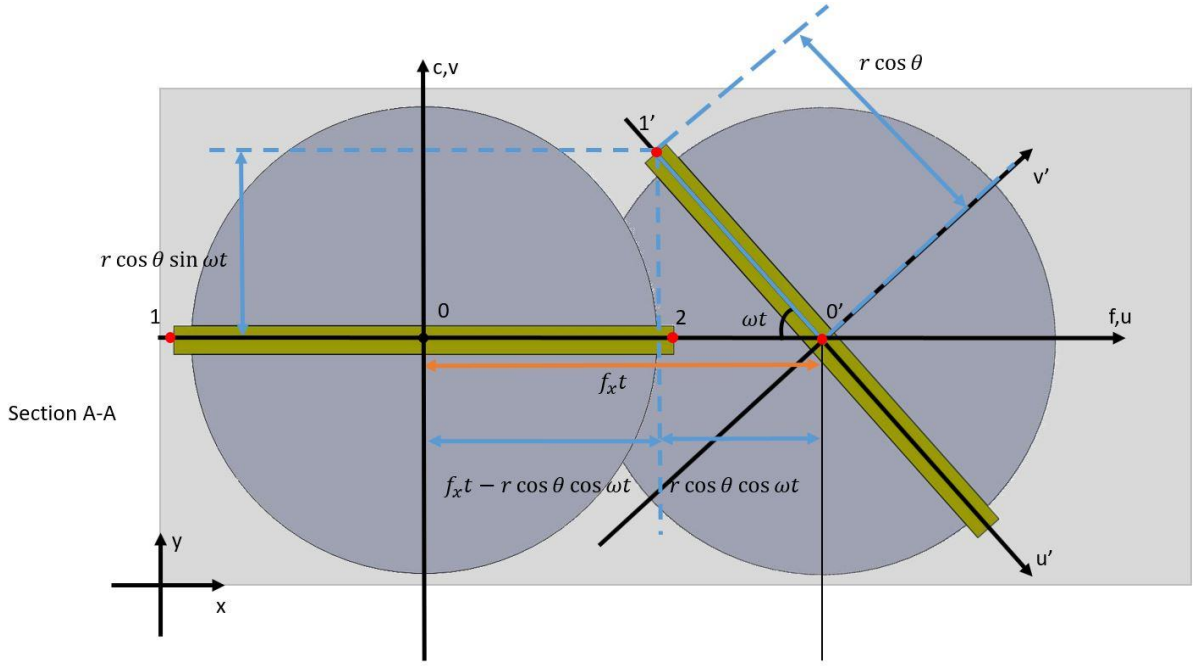

Figure 13. View A-A from figure 12 at time = 0 and time = t

From Fig 13 the u position of point 1 at time = 0 relative to the tool origin is:

$$u_0 = (-r\,cos\,\theta) \qquad \text{eqn 1}$$

The change in position (u) resulting from the rotational movement from Point 1 to Point 1' as shown in Fig 13 is:

$$u = -r\,cos\,\theta\,cos\,\omega t \qquad \text{eqn 2}$$

Adding the translation caused by the feed, the f_1 position of Point 1' is given by:

$$f_1 = \mathrm{u} + (f_x\mathrm{t}) = (f_x\mathrm{t}) - (r\,cos\,\theta\,cos\,\omega t) \qquad \text{eqn 3}$$

The c coordinate of Point 1' is not affected by the feed rate and is parallel to the machine coordinate system in the y direction. Hence only movement caused by spindle rotation needs to be considered to determine the position. From Fig 13:

$$v = c = r\,cos\,\theta\,sin\,\omega t \qquad \text{eqn 4}$$

$$y = y_0 + c = y_0 + r\,cos\,\theta\,sin\,\omega t$$ eqn 5

To illustrate the 3D effect of the cutting process, the n coordinate must be included. Here, the n direction is aligned with the tool coordinate system in the w direction, and is also perpendicular to the workpiece surface. Therefore, the z direction is also aligned with the n and w direction. Since this coordinate is not affected by the feed rate and the spindle speed, it can be taken from Fig 12 that:

$$w = n = r - r\,sin\,\theta$$ eqn 6

$$z = z_0 + n = z_0 + r - r\,sin\,\theta$$ eqn 7

As described in section 2.5, the x, y and z axes are the global coordinate system. Therefore, the TCS coordinates referred to as u, v and w and are used when defining the angle of the tool later. This TCS is coincident with the FCN here as there is no lead or tilt angle and can be expressed as a vector as follow:

$$\begin{bmatrix} u \\ v \\ w \end{bmatrix} = \begin{bmatrix} -r\cos\theta\cos\omega t \\ \mathrm{r}\cos\theta\sin\omega t \\ \mathrm{r} - \mathrm{r}\sin\theta \end{bmatrix}$$ eqn 8

Fig 14 illustrates in orange the cutting path of the highest point of the first cutting edge, where θ=0. The blue trace in Fig 14 illustrates the movement of the highest point along the second cutting edge of the cutting path. The f coordinate of this point is slightly different from the same position on the first cutting edge, since the second cutting edge is ahead of the centre point of the cutting tool. Therefore, the f_2 coordinate is given by.

$$f_2 = (f_x t) + (r\cos\theta\cos\omega t)$$ eqn 9

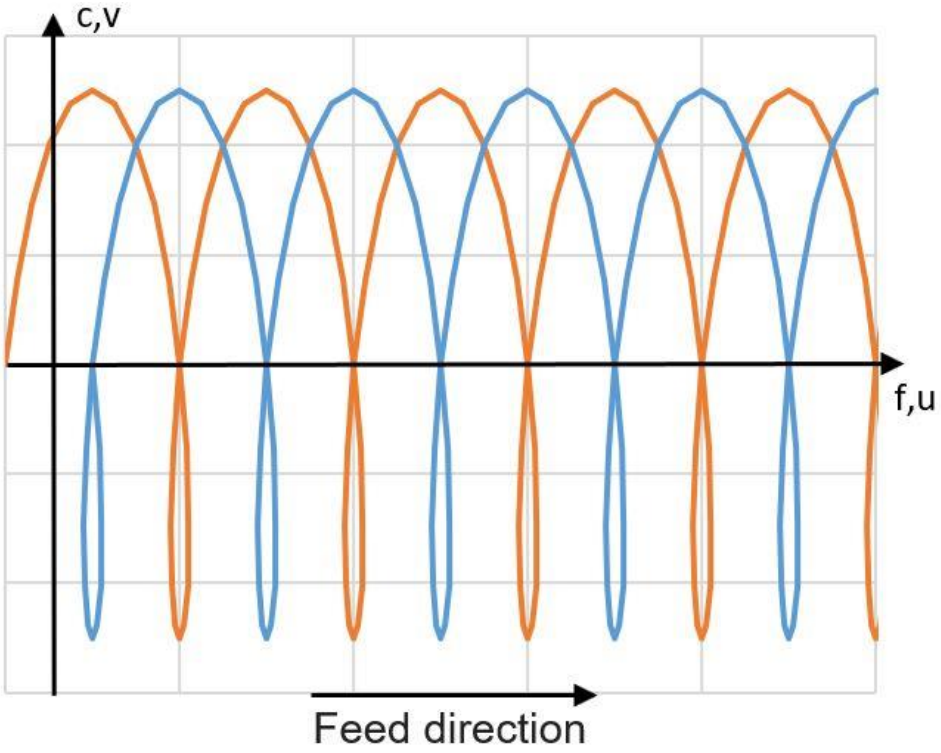

Figure 14. Illustration of the tool paths of two cutting flutes

3.2. Multiple cutting edges

Fig 13 shows that the second cutting edge is 180° away from the first. This means that the angular displacement of the second cutting edge's f and c positions are π from the first cutting edge. Therefore, the position of the second cutting edge in the FCN matrix is given by.

$$\begin{bmatrix} u \\ v \\ w \end{bmatrix} = \begin{bmatrix} -r\cos\theta\cos(\omega t+\pi) \\ \mathrm{r}\cos\theta\sin(\omega t+\pi) \\ \mathrm{r}-\mathrm{r}\sin\theta \end{bmatrix} \quad \text{eqn 10}$$

Similarly, for a cutter with three cutting edges, the second edge matrix is as follow.

$$\begin{bmatrix} u \\ v \\ w \end{bmatrix} = \begin{bmatrix} -r\cos\theta\cos(\omega t+\frac{2\pi}{3}) \\ \mathrm{r}\cos\theta\sin(\omega t+\frac{2\pi}{3}) \\ \mathrm{r}-\mathrm{r}\sin\theta \end{bmatrix} \quad \text{eqn 11}$$

The third edge matrix is as follow:

$$\begin{bmatrix} u \\ v \\ w \end{bmatrix} = \begin{bmatrix} -r\cos\theta\cos(\omega t + \frac{2\pi}{3} * 2) \\ \mathrm{r}\cos\theta\sin(\omega t + \frac{2\pi}{3} * 2) \\ \mathrm{r} - \mathrm{r}\sin\theta \end{bmatrix} \quad \text{eqn 12}$$

3.3. Incorporate the theory into MATLAB

This study used MATLAB to simulate the theorical calculation described in the previous section. The theorical calculation was coded in the MATLAB language and added to the MATLAB script function with the pre-set cutting parameters shown in Appendix A. In Fig 15, the procedure for model generation is shown in a flow chart. First, the coding in the script requires pre-set values for the feed rate, spindle speed and radius of the cutting tool. Second, it requires the number of the interval section and the number of points on each cutting edge in each interval section. These two numbers also determine the resolution of the point cloud plot. Third, a loop uses all the pre-set parameters to find the position of each point along the cutting edge and then uses the fcn matrix to calculate the result for each point and generates a point cloud as the result.

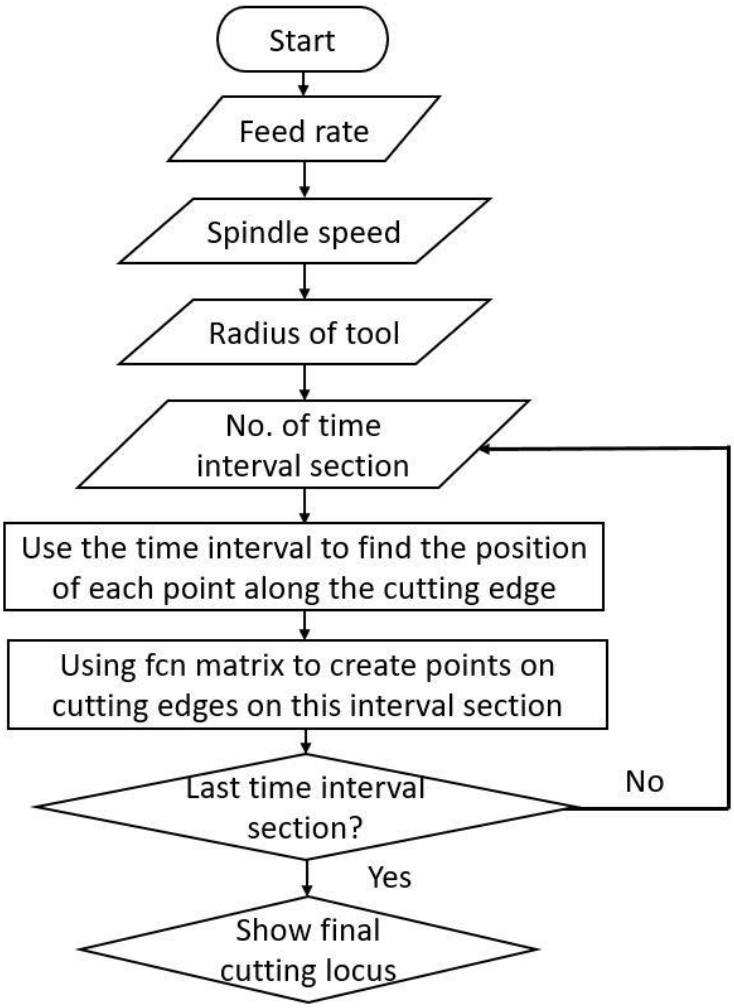

Figure 15. Model generation process in MATLAB

Three examples of point clouds were generated by MATLAB to show multiple cutting edges and different feed rates. The first set of example shows two and three cutting edges. In Fig 16, the example shows that there are two starting edges 180° apart from each other and rotated through two revolutions. The distance in the x direction between the beginning and the end of the top of the first cutting edge point is 7.05 mm. The pre-set input value of the feed rate was 7 mm/s and the spindle speed was 2π rad/s, which results in each cutting edge advancing by 7 mm per revolution. The difference between the two results was less than 1 %. This is mainly for two reasons. The first is because the resolution is not high enough, creating a slight difference, and the second is because the first interval section of the second rotation does not line up exactly with the x axis as a result of the

setup. In reality, the cutting will actually happen at $x = 0 + tool\ radius$ as the cutting actually starts after the cutting tool moves into the workpiece and this position is the closest possible position. The second example in Fig 17 shows that there are three starting edges 120° apart from each other. These starting edges represent the cutting edges on the tool. The distance in the x direction between the beginning and the end of the top of the first cutting edge point is the same as for two cutting edges.

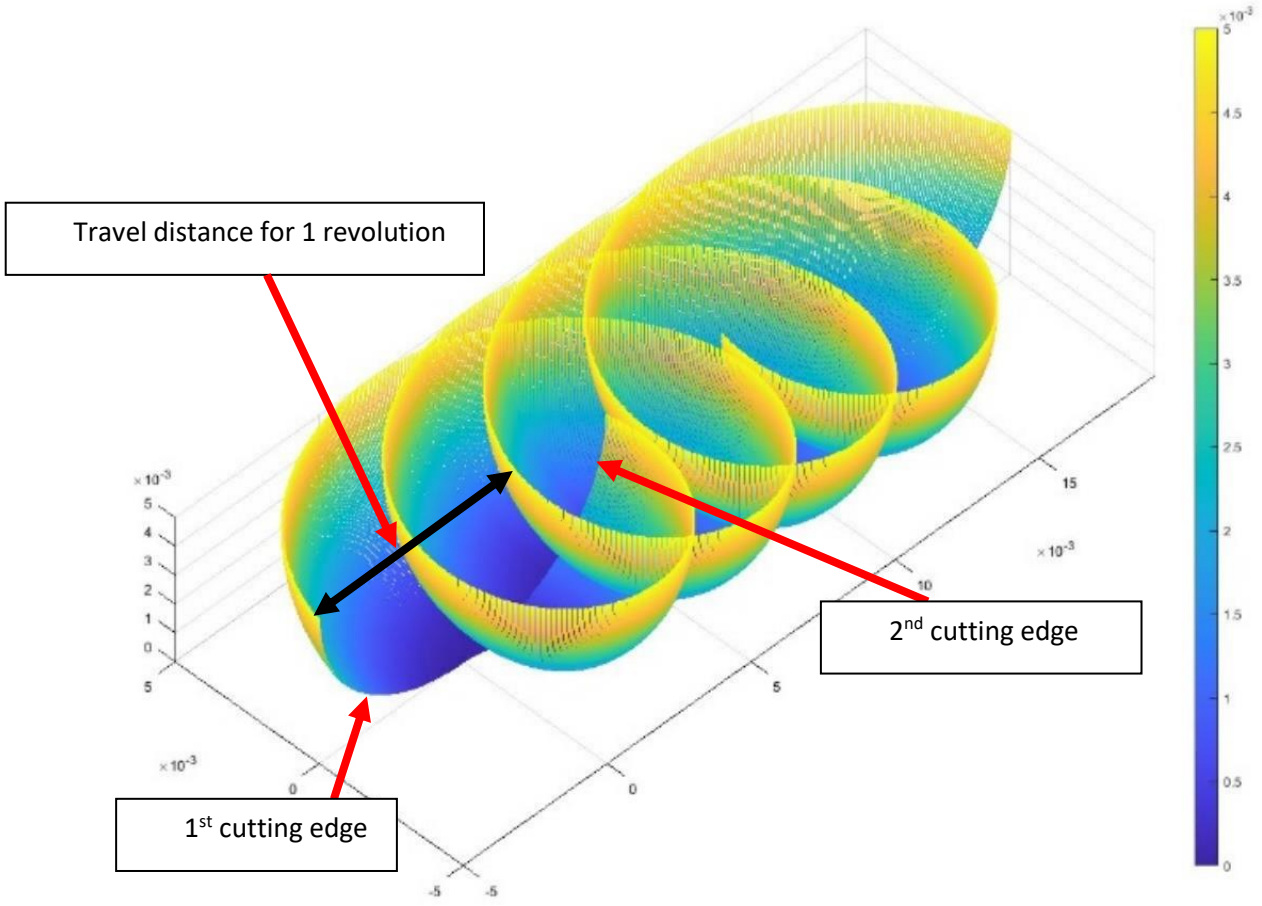

Figure 16. Cutting path for two cutting edges

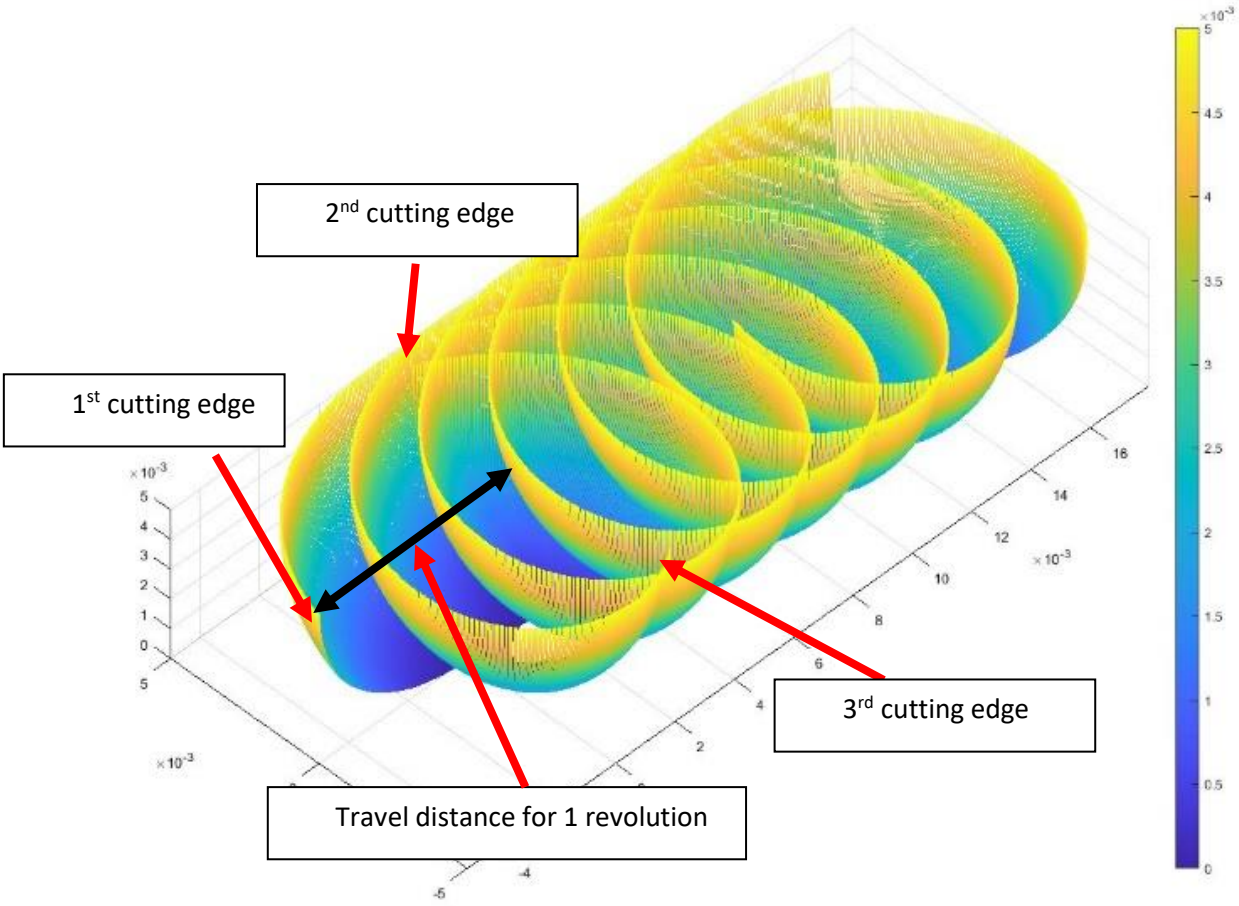

Figure 17. Cutting path with three cutting edges

The third example in Fig 18 has a double feed rate of 14 mm/s compared to the example in Fig 16. The distance between the beginning and the end of the top of the first cutting edge point is 14.11 mm. The difference between the pre-set input and the output is less than 1%.

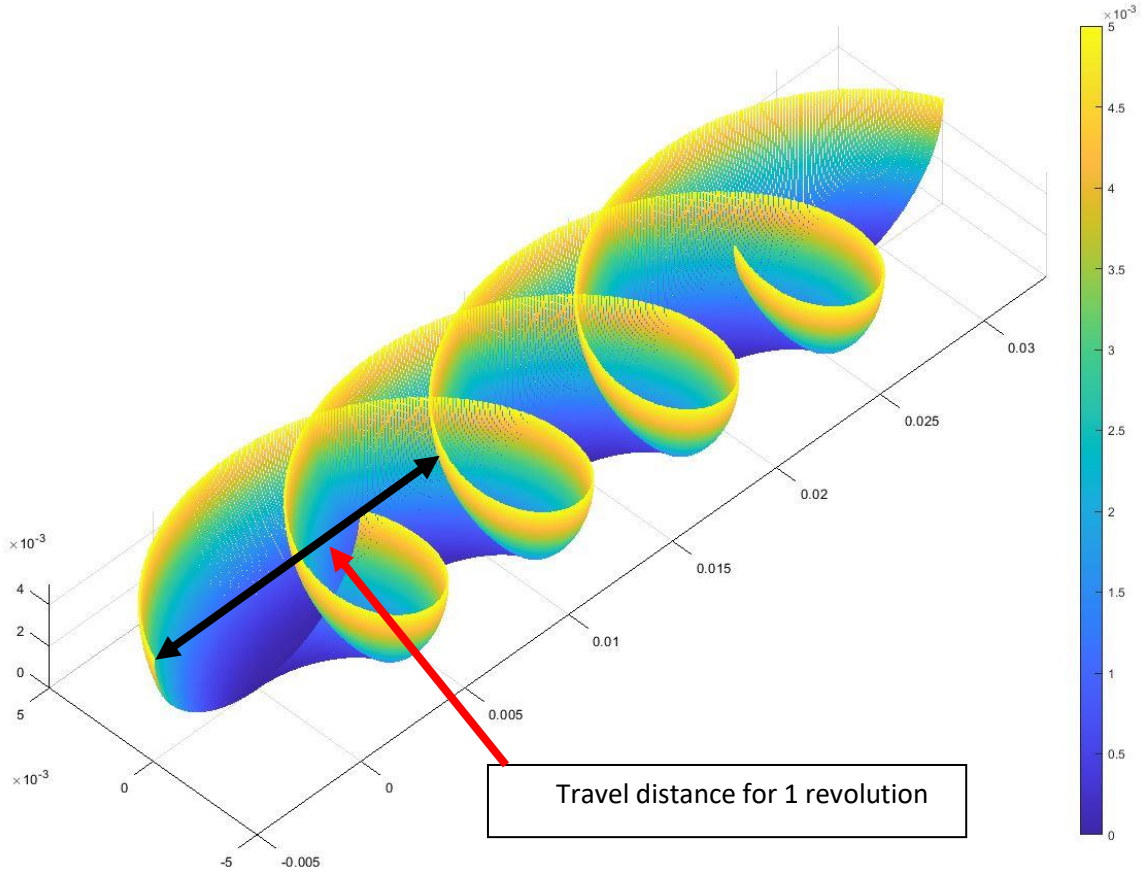

Figure 18. Two cutting edges cutting path with a faster feed rate

3.4. Conclusion

This chapter concludes with the following observations:

- The cutting tool position has been defined so that the tool position is normal to the axis.
- An fcn matrix has been defined to determine the rotational movement of the cutting tool in time. The cutting trail was discussed, and a set of calculations developed to illustrate the rotational movement of the cutter relative to cutter diameter, spindle speed and time.
- Multiple cutting edges have been defined and added to the model for different purposes. The fcn matrix and other cutting parameters have been implemented in MATLAB code and have generated point clouds to simulate the cutting tool locus.

4. Kinematic cutting model with additional cutting parameters

4.1. Introducing lead and tilt angle

When either lead or tilt angle are applied during the cutting process, the TCS and FCN will not be coincident as the u and w or v and w axes will move. Fig 19 shows the relationship between TCS and FCN with changing tilt angle that is used to identify and transform the lead and tilt angle from TCS to FCN. These two transformations are similar to that used by Ozturk and Budak (2007) in their research.

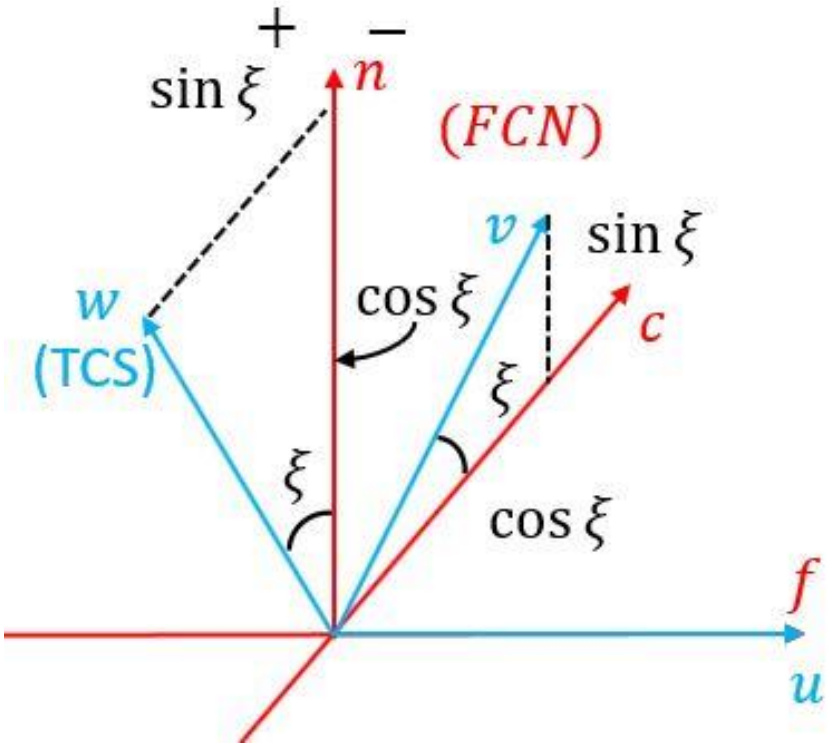

Figure 19. Translation between TCS and FCN for tilt angle

By using Fig 19 to identify the relationship between those coordinate systems for tilt angle of the first cutting edge, it can be shown using the coordinate transformation matrix that:

$$\begin{bmatrix} f \\ c \\ n \end{bmatrix} = \begin{bmatrix} 1 & 0 & 0 \\ 0 & \cos\xi & -\sin\xi \\ 0 & \sin\xi & \cos\xi \end{bmatrix} \begin{bmatrix} u \\ v \\ w \end{bmatrix} = \begin{bmatrix} 1 & 0 & 0 \\ 0 & \cos\xi & -\sin\xi \\ 0 & \sin\xi & \cos\xi \end{bmatrix} \begin{bmatrix} -r\cos\theta\cos(\omega t) \\ \mathrm{r}\cos\theta\sin(\omega t) \\ \mathrm{r} - \mathrm{r}\sin\theta \end{bmatrix} \quad \text{eqn 13}$$

Therefore, by using Fig 20 to identify the relationship between those coordinate systems for lead angle of the first cutting edge, it can be written using a coordinate transformation matrix as:

$$\begin{bmatrix} f \\ c \\ n \end{bmatrix} = \begin{bmatrix} \cos\varphi & 0 & \sin\varphi \\ 0 & 1 & 0 \\ -\sin\varphi & 0 & \cos\varphi \end{bmatrix} \begin{bmatrix} -r\cos\theta\cos(\omega t) \\ \mathrm{r}\cos\theta\sin(\omega t) \\ \mathrm{r}-\mathrm{r}\sin\theta \end{bmatrix} \quad \text{eqn 14}$$

Here, the negative lead angle shown in Fig 20 represents a push feed style and a positive lead angle a pull feed style.

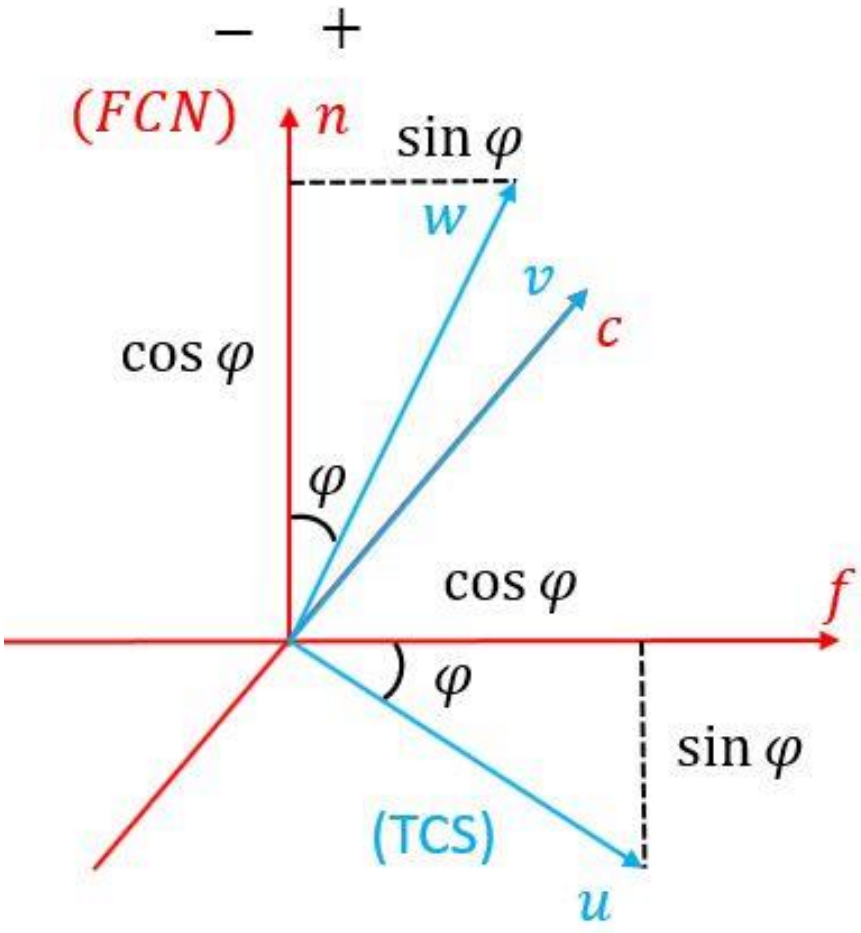

Figure 20. Translation between TCS and FCN for lead angle

By combining eqn 13 and eqn 14 into the matrix of the tilt and lead angle, the matrix becomes:

$$\begin{bmatrix} f \\ c \\ n \end{bmatrix} = \begin{bmatrix} \cos\varphi & 0 & \sin\varphi \\ \sin\xi\sin\varphi & \cos\xi & -\sin\xi\cos\varphi \\ -\sin\varphi\cos\xi & \sin\xi & \cos\xi\cos\varphi \end{bmatrix} \begin{bmatrix} -r\cos\theta\cos(\omega t) \\ \mathrm{r}\cos\theta\sin(\omega t) \\ \mathrm{r}-\mathrm{r}\sin\theta \end{bmatrix} \quad \text{eqn 15}$$

By combining eqn 15, the feed rate in time and the GCS origin into the fcn matrix, the matrix becomes:

$$\begin{bmatrix} x \\ y \\ z \end{bmatrix} = \begin{bmatrix} f \\ c \\ n \end{bmatrix} + \begin{bmatrix} x_0 + f_x t \\ y_0 \\ z_0 \end{bmatrix} \quad \text{eqn 16}$$

Here, the GCS origin is the point that the tool tip at the start point.

Appendix B shows MATLAB code for all the formulae given in Appendix A. When all the criteria are defined, the software will generate a tool path to simulate the cutter path and the surface generated by it. The software generates the movement of the cutting edge during the cutting process to give the result. The following sub-chapters show the point cloud resulting from MATLAB when simulating lead, tilt and combinations of both angles. All the examples used a model with one cutting edge as this demonstrates the cutting edge trail and lead and tilt angle more clearly. Since this method incorporates both lead and tilt angle into the cutting process, the results from the model not only represent the material surface after simulated cutting, but it also shows the movement of the cutter. Therefore, it is necessary to crop the upper part of the simulation to show the surface generated by the cutter alone. This step will be explained in Chapter 5.

4.1.1. Lead angle applied

The first simulation demonstrates the impact of leaning the tool backward when viewed perpendicular to the direction of travel. The part of the cutting edge with a lead angle of 18° is shown by the point cloud in Fig 21. Other cutting parameters are shown in Table 1. As expected, the cutter axis lies in the x-z plane but is at 18° to the y axis and feeds in the x direction.

Table 1. Initial simulation cutting parameters

Feed rate	Spindle speed	Cutter radius	Time
5 mm/s	2π rad/s	5 mm	3 seconds

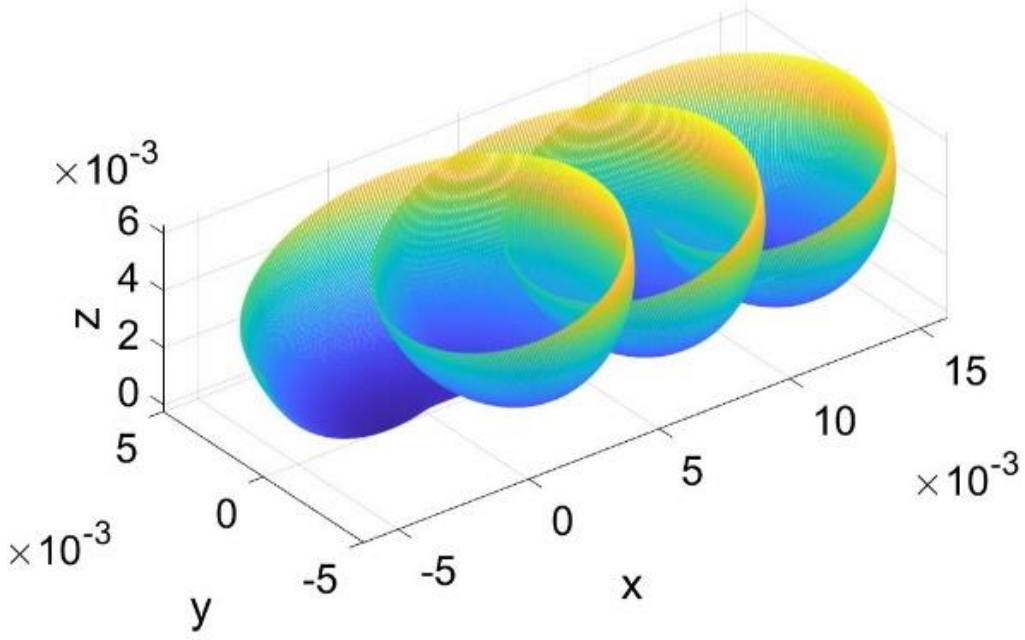

Figure 21. Overall 3D view of a cutting model with one cutting edge and lead angle applied (dimension in m)

4.1.2. Tilt angle applied

The second simulation demonstrated the impact of tilting the tool to the right when viewed in the direction of travel (i.e. with a negative tilt angle ξ as defined in Fig. 20). A tilt angle of -18° was applied with other cutting parameters as shown in Table 1. The point cloud generated is shown in Fig. 22. As expected, the cutter axis is at -18° to the x axis and feeds in the x direction.

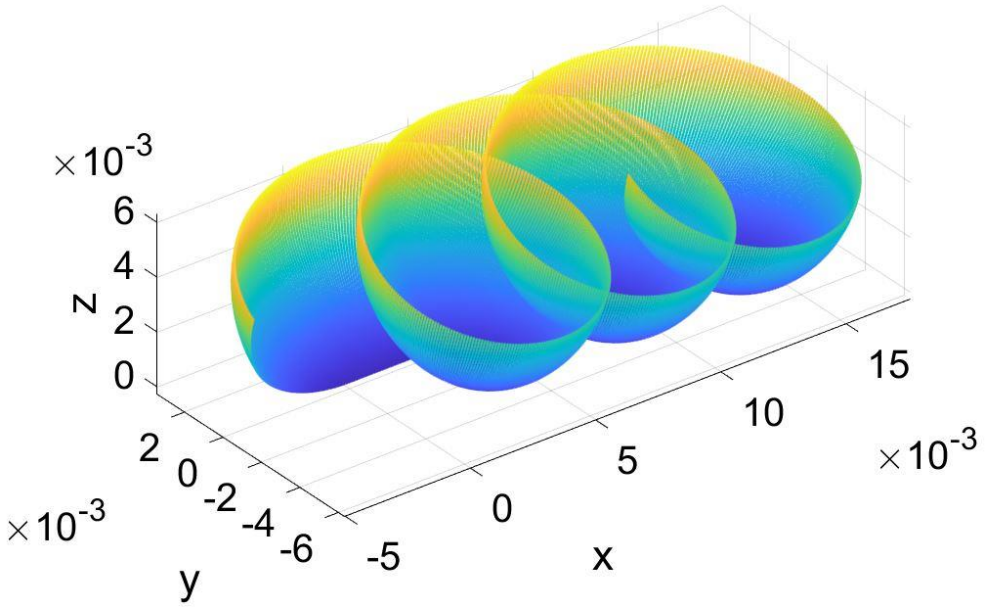

Figure 22. Overall 3D view of a cutting model with one cutting edge and tilt angle applied (dimension in m)

4.1.3. Lead and tilt angle applied

The third simulation demonstrates the application of both lead and tilt angle. The details are given in Table 2, along with the other cutting parameters. This simulation generated the point cloud shown in Fig 23.

Table 2. Simulation parameters with both lead and tilt angle applied

Feed rate	Spindle speed	Cutter radius	Time	Tilt angle	Lead angle
5 mm/s	2π rad/s	5 mm	3 seconds	-18°	18°

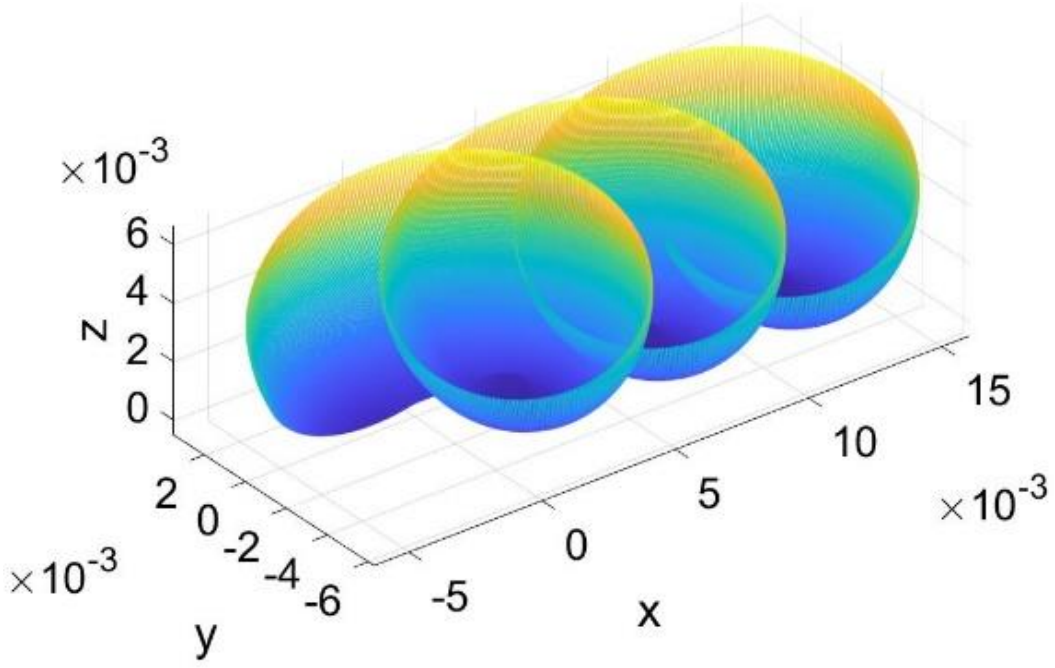

Figure 23. Overall 3D view of a cutting model with one cutting edge, with both lead and tilt angle applied (dimension in m)

The combined effect of applying both tilt and lead angles to the simulation can be seen. However, the actual angle shown on the simulation has a tilt angle of -18° and a lead angle of 18.86°. This has arisen because the simulation applied the tilt angle first and subsequently applied the lead angle. Therefore, the final unit vector of the cutter has changed slightly.

4.2. Introducing helix angle on the cutter

Most ball end cutters do not have a straight cutting edge. A common geometry for the tool edge is a helical profile. When adding the angle of the helix into the model, the TCS must be amended. From Fig 24, point 1 on the cutting edge relates to (r_i). The angle from the shank of the tool is no longer the parameter required to find the position of point 1. Instead, a new variable, the length (w_i) from the tool tip to the point 1 is used. To find the position of point 1, (w_i) and the radius can determine (r_i) as follows.

$$r^2 = {r_i}^2 + (r - w_i)^2$$

$$\therefore {r_i}^2 = 2rw_i - {w_i}^2 \qquad \text{eqn 17}$$

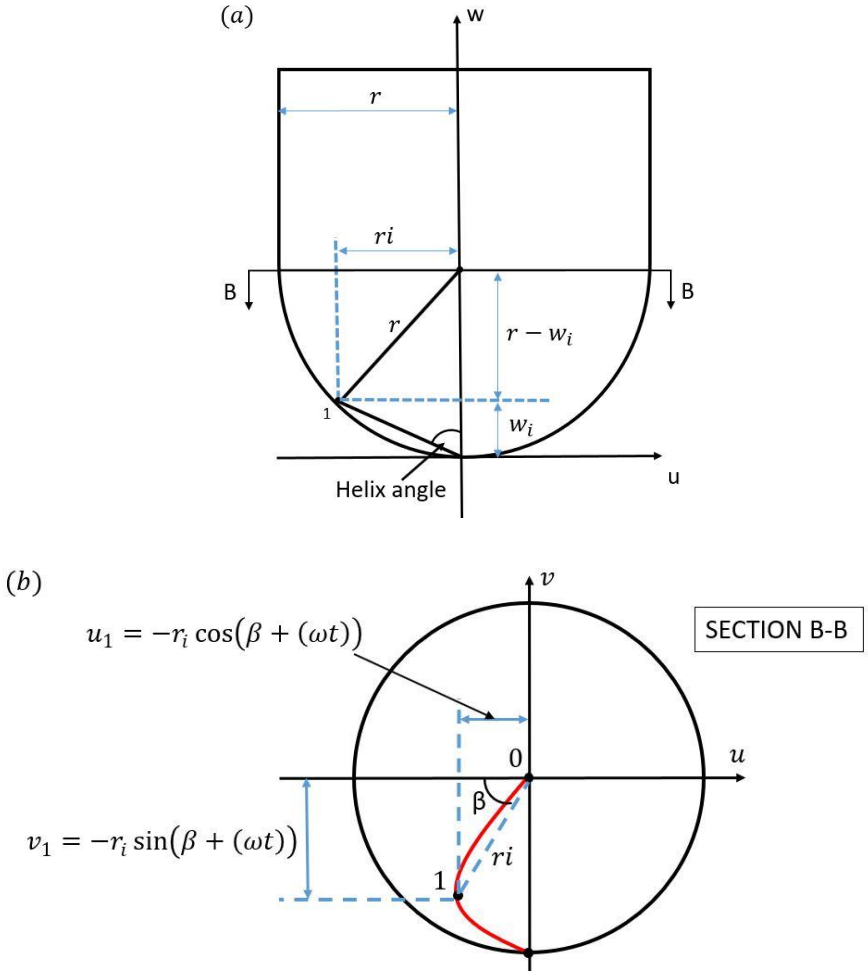

Figure 24. Definition of the geometry of a ball end cutting tool with helical cutting edge in (a) side view and (b) cross section view

Fig 24(a) shows the new definition of the height in w direction, and Fig24(b) shows the angle (β) is the angle between the u axis and (r_i), using an equation similar to that in Arizmendi et al. (2019). Point 1 at height (w_i) can be obtained by projection onto a spherical surface of radius (r) perpendicular to the tool axis, where the angle (β) can be expressed as a function of the helix angle, the height (w_i) and a pre-set radius as in the following equation.

$$\tan(helix) = \left(\frac{r \times \beta}{w_i}\right)$$

$$\beta = \tan(helix)\left(\frac{w_i}{r}\right) \quad \text{eqn 18}$$

$$w_i = \textit{ the height between discrete point on the cutting edge to the axis}$$

Therefore, the u position for the first set of cutting edges in Fig 24(b) taking the rotational movement into consideration is:

$$u_1 = -r_i \cos\big(\beta + (\omega t)\big) \quad \text{eqn 19}$$

To add the second and the third sets on cutting edge for a three cutting edges tool, 2/3π is added to the time (t) as shown:

$$u_2 = -r_i \cos\left(\beta + \left(\omega t + \frac{2\pi}{3}\right)\right) \quad \text{eqn 20}$$

$$u_3 = -r_i \cos\left(\beta + \left(\omega t + \frac{4\pi}{3}\right)\right) \quad \text{eqn 21}$$

To add the second set of cutting edge for a two cutting edge tool, π is added to the time (t) as shown:

$$u_2 = -r_i \cos\big(\beta + (\omega t + \pi)\big) \quad \text{eqn 22}$$

The v coordinate of point 1 is not affected by the feed rate. Hence the only movement is the spindle rotation which is required to determine the position as shown:

$$v_1 = -r_i \sin\big(\beta + (\omega t)\big) \quad \text{eqn 23}$$

To add the second and the third set of cutting edges for a three cutting edge tool, 2/3π is added to the time (t) as shown:

$$v_2 = -r_i \sin\left(\beta + \left(\omega t + \frac{2\pi}{3}\right)\right) \quad \text{eqn 24}$$

$$v_3 = -r_i \sin\left(\beta + \left(\omega t \frac{4\pi}{3}\right)\right) \quad \text{eqn 25}$$

To add a second set of cutting edges for a two cutting edge tool, π is added to the time (t) as shown:

$$v_2 = -r_i \sin\big(\beta + (\omega t + \pi)\big) \qquad \text{eqn 26}$$

Since the w coordinate of point 1 is not affected by the feed rate and spindle speed, only (w_i) is required for this model and it is the same (w) as in eqn 8.

The position vector of point 1 in the tool coordinate system is:

$$\begin{bmatrix} u \\ v \\ w \end{bmatrix} = \begin{bmatrix} -r_i \cos\big(\beta + (\omega t)\big) \\ -r_i \sin\big(\beta + (\omega t)\big) \\ w_i \end{bmatrix} \qquad \text{eqn 27}$$

Combining the latest uvw vector with the multiple cutting edges equations will simulate the cutting tool path for a variety of cutting parameters including helix angle and multiple cutting edges.

Combining this result with the previous equations determines r_i and β. A new uvw vector coding was developed. Sample MATLAB code for all these formulae is given in Appendix C. This code was used to generate a helix cut-out and a 1/3 turn with single cutting edge as shown in Fig 25. This example simulated a 5 mm radius with a 30° helical angle on the cutting edge, and only one cutting edge has been generated with 1mm/s feed rate to demonstrate the helical effect more clearly. The result shows that the start and finish sections both have a helical effect rather than a straight line as in the previous result. The origin is set at the tool tip and the helical effect is set to go in the anti-clockwise direction. The result also shows that it matches the calculation.

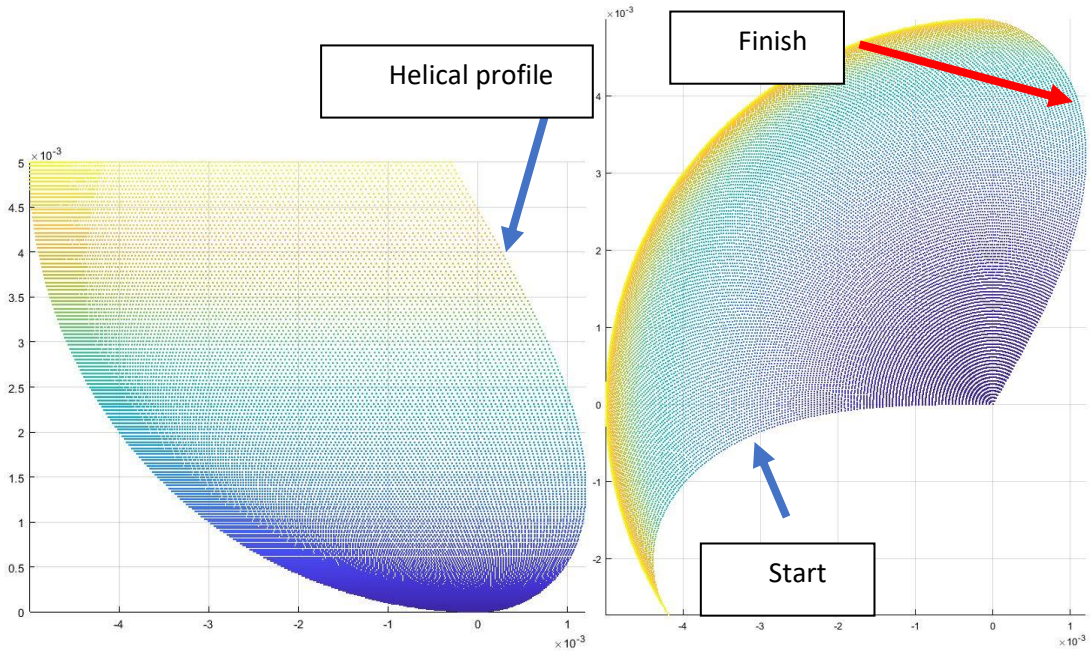

Figure 25. Side view of the helix demonstration (left), Top view of the helix demonstration (right)

4.3. Conclusion

This chapter summarised as follows:

- Lead and tilt angles have been defined by a rotation matrix and added to the MATLAB code in Appendix B to convert from the tool coordinate system to the [fcn] coordinate system.
- Results for the lead angle, tilt angle and both lead and tilt angles have been generated. The lead angle result showed that the cutting locus can lean forward or backward depending on positive or negative lead angle that is consistent with the actual tool orientation. The tilt angle result showed that the cutting locus can lean to either side depend ing on the whether the tilt angle is positive or negative, consistent with the actual tool orientation. The result for both lead and tilt angles combined has a slight difference in lead angle as the angle is slightly changed after the tilt angle is set in the code.
- A helical profile has been defined in a fcn matrix and incorporated in the MATLAB code to simulate a complex profile in Appendix C.

- Results for a helical cutting edge profile have been generated and the result shows the swept profile of the cutting edge in the cutting locus.
- Results for either lead and tilt angle are accurate, but the result for both lead and tilt angles combined has a slight difference in lead angle as the angle is slightly changed after the tilt angle is set in the code.

5. Model development

5.1. Introduction

The previous chapter demonstrated the calculation of the cutter position and shape, and the initial model coded in MATLAB. This chapter focuses on improving the simulation and optimising the cutting outcome. This chapter presents improved code to generate and filter the resulting trail of the cutting edge into a simulated surface.

5.2. Improved model

5.2.1. Number of time increments per revolution

The number of sections that determine the resolution of the whole cutting trail is a pre-set number. This led to an issue that the resolution changes when the time unit changes if no other parameters have changed. The improved model changes the setup by calculating the time for each revolution and using it to determine the number of sections for each revolution rather than for the complete time unit. This ensures that even when the total number of time units changes, the resolution of the final cutting trail remains the same. The following figures show the difference between 20 sections per revolution (Fig 26a) and 200 sections per revolution (Fig. 26b).

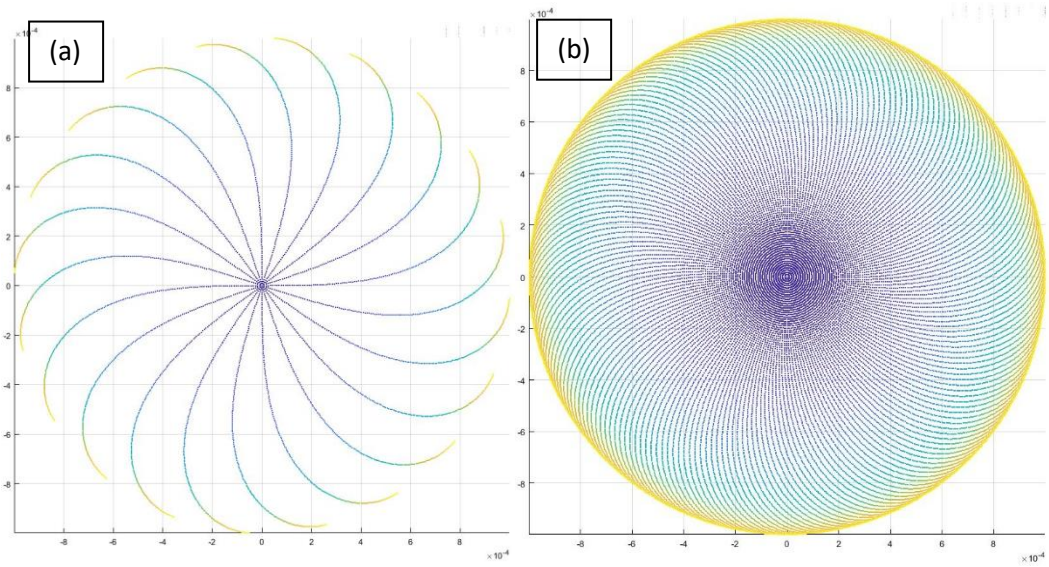

Figure 26. Top view of the cutting trail with (a) 20 sections per revolution, (b) 200 sections per revolution

5.2.2. Filter the result to create a surface

The idea behind filtering the cutting trail into a surface is to determine the lowest point in each pre-set grid element. The code defines the grid size and the range in both the x and y directions. In order to filter the cutting trail, a loop has been incorporated in the code. The loop searches for the lowest value in the z direction to find the lowest point within each pre-set grid element to represent the final surface. Fig 27 shows a flowchart of the process and sample code is given in Appendix D.

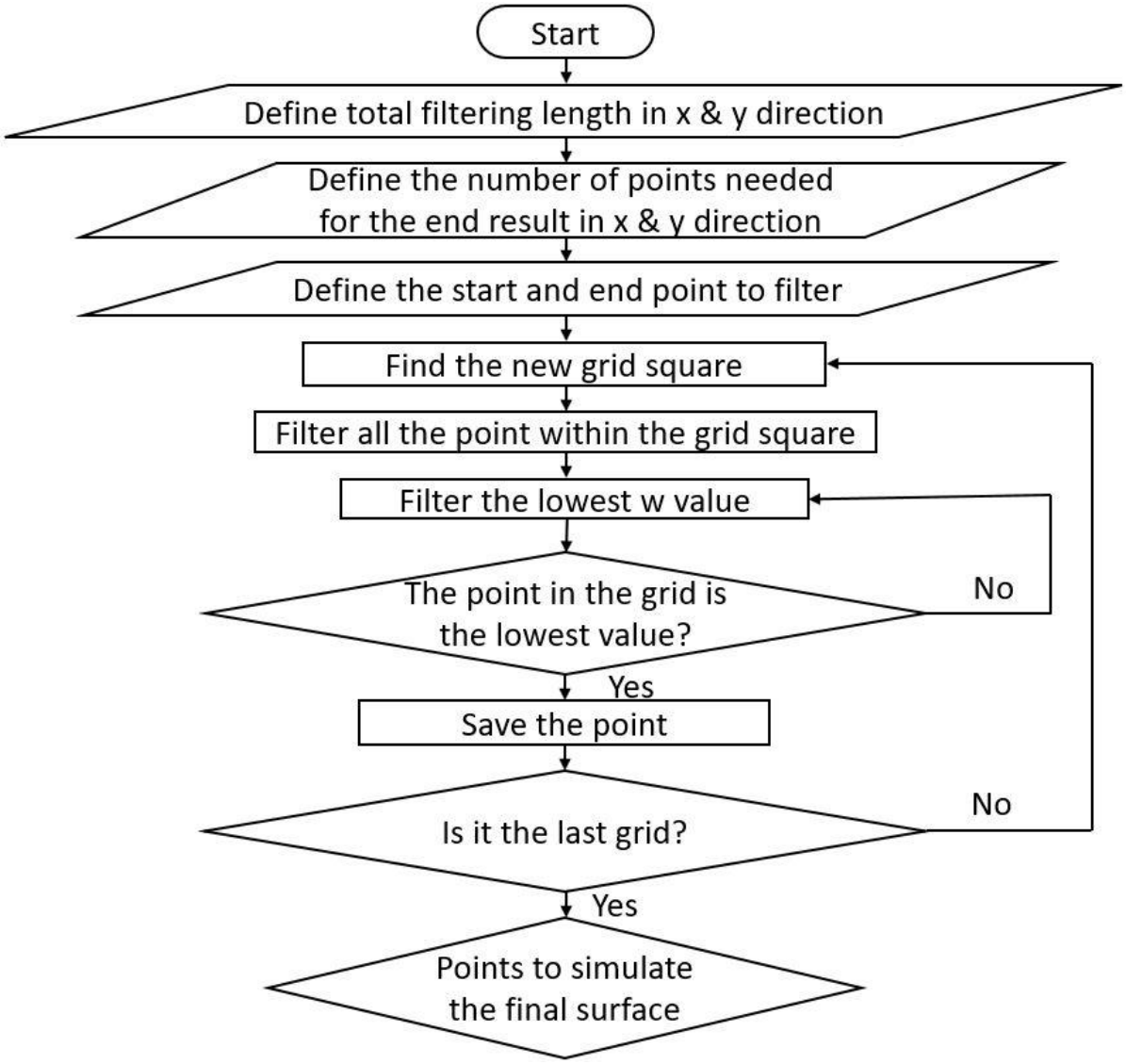

Figure 27. Cutting trail filtration process in MATLAB

Fig 28(a) shows an example of a cutting trail generated by the previous code. This example used a three cutting edge cutter with a tool radius of 1 mm, feed rate of 0.324 m/s, spindle speed of 12000 rev/min, lead angle of -55° and helix angle of 30°. This example has a relatively fast feed rate. Therefore, all three cutting edges show clearly. Fig 28(b) shows an image of the grid defined in the code. The code will loop through all the points in the entire point cloud to identify whether those points are in the relevant grid square. Fig 28(c) shows a three-dimensional view of the example grid square in Fig 28(b). It can be seen here that this includes partial point clouds from three cutting edge

passes. The code uses the relevant grid square and determines the lowest value in the z direction in that grid square. This value will be used to generate the point cloud for the final surface.

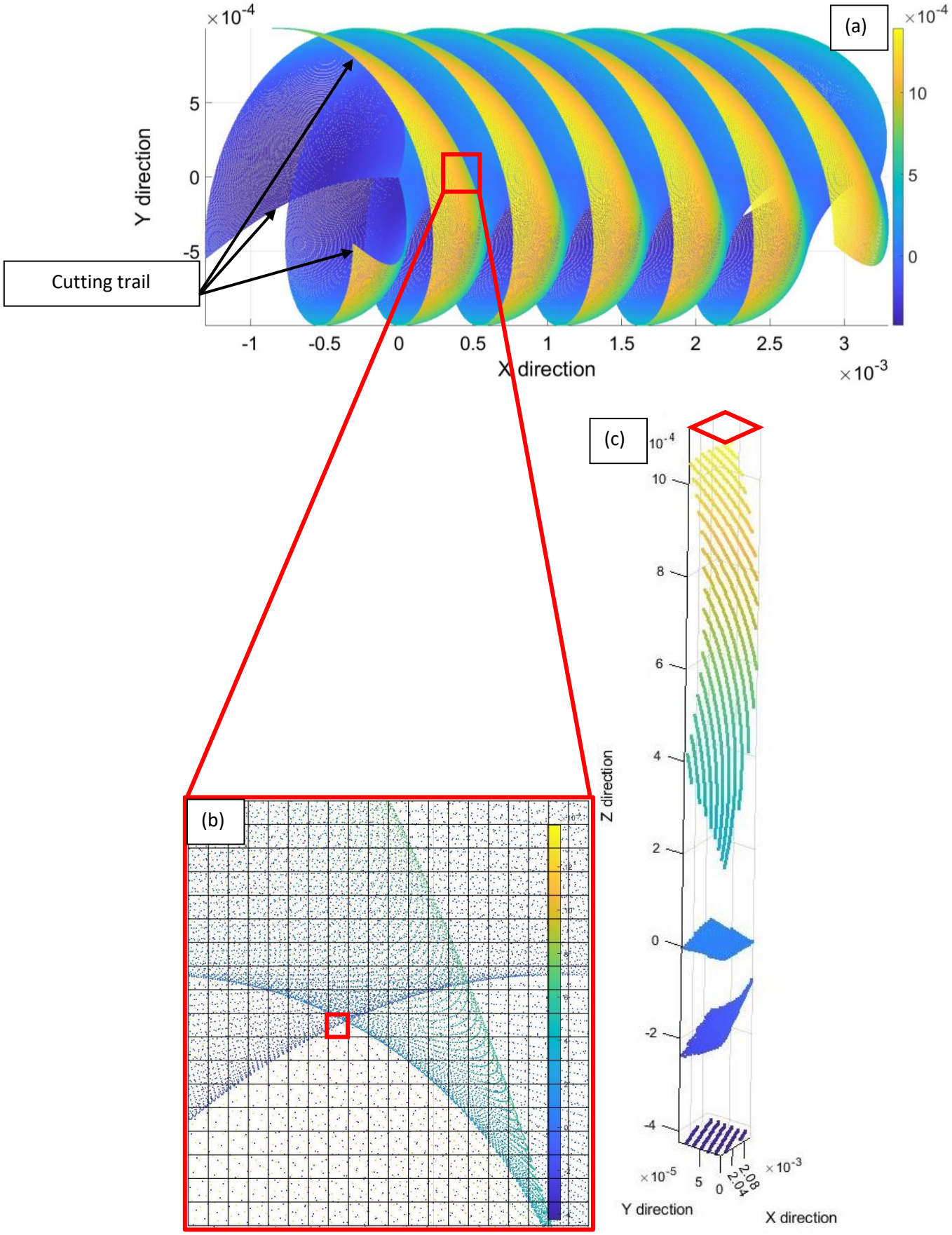
(a)
Cutting trail
Y direction
X direction
(b)
(c)
Z direction
Y direction
X direction

Figure 28. (a) Cutting trail before filtration, (b) Grid setup for the filtration process, (c) Grid example from (b) (dimension in m)

The final surface point cloud resulting from Fig 28 is shown in Fig 29. This example used 200 grid points in the x direction and 137 in the y direction for a total of 27,400 grid points. The example limited the z value to -0.1 mm, which means any points above this value in the z direction will not be used and it shows the approximate width of the feed interval cusp that represent the surface on a workpiece. Fig 29 shows that the feed interval cusp mark has been generated within the cusp and it can be seen as the final surface result. The result clearly shows that the feed interval cusp marks are not straight and chasing in the x direction, i.e. the feed interval cusp marks are not perpendicular to the feed direction. The phenomenon arises from the relatively fast feed rate and the helical profile of the cutting edges pushing the marks so they chase forward. Another feature that can be seen in the image is the straight profile at the start and end of the point cloud, which arises because a limit has been set on the x value. Therefore, any point outside this limit will not be used in this point cloud.

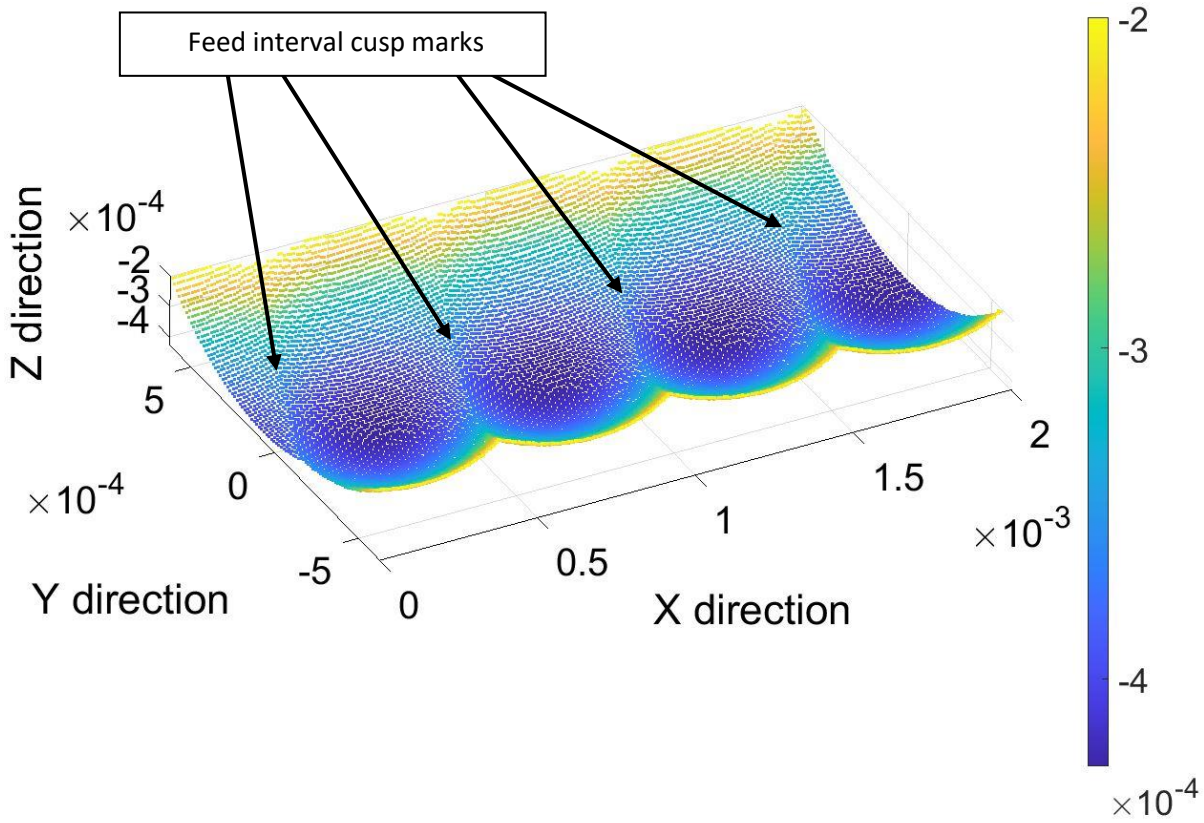

Figure 29. Point cloud of a filtered cutting trail (dimension in m)

Another example in Fig 30 uses the same parameters as above, but the feed rate is ten times slower at 0.0324 m/s. These filtered results do not show the feed interval cusp marks as clearly as in the previous example, because there are fewer points in each feed interval cusp mark than with a faster feed rate. Hence the resolution of the filtration process was reduced massively. Therefore, there are many error points in the point cloud as there are insufficient points for the code to find the ideal result.

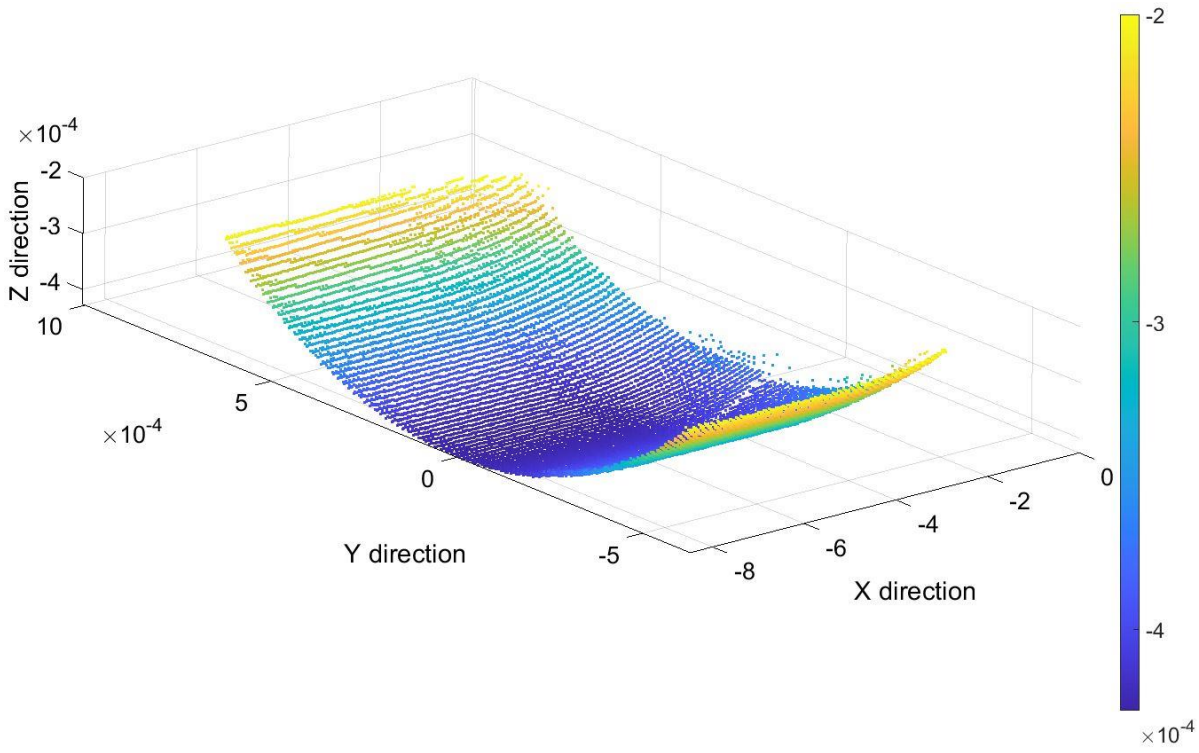

Figure 30. Point cloud of a filtered cutting trail with a slow feed rate (dimension in m)

Initially, this part of the code was integrated after the code to generate the cutting trail and the benefit of doing it this way is that the surface result is generated in one set of code. However, it also means that if an error occurs, it will only show at the end of the simulation. The Nyquist Shannon sampling theorem as mentioned in section 2.9 demonstrates that the sampling rate needs to be at least twice the highest frequency to avoid any aliasing error. Fig 29 shows that only 4 feed interval marks have been filtered. This shows that 200 grid points in x direction for 4 feed interval marks and 137 grid points in y direction for 1 pick interval mark are required to avoid aliasing error. However, if the future model contains features such as tool wear or vibration during cutting, the sampling rate needs to be recalculated to determine the new number of grid points for both x and y directions.

5.2.3. Filter the surface into a profile

The main aim of this model is to determine the roughness parameter of the simulated surface. In this step, code has been developed to loop through all the points created in the previous step and find points within a pre-set y value range. This means that it can pick a profile along a particular line in the y direction. Also, the (Ra) equation, which is the arithmetic average of the absolute values of the profile height deviations from the mean line, is incorporated in the code. In this study, those values are the z value of all the points along the sampling area. It can generate a point cloud result and the Ra value. An example is shown in Fig 31 and the sample code is given in Appendix E.

$$Ra = \frac{|Z_1|+|Z_2|+|Z_3|+\cdots+|Z_{ni}|}{ni} \quad \text{eqn28}$$

$Z_{(x)} = \text{profile height function}$

$\text{ni} = \text{total number of peak}$

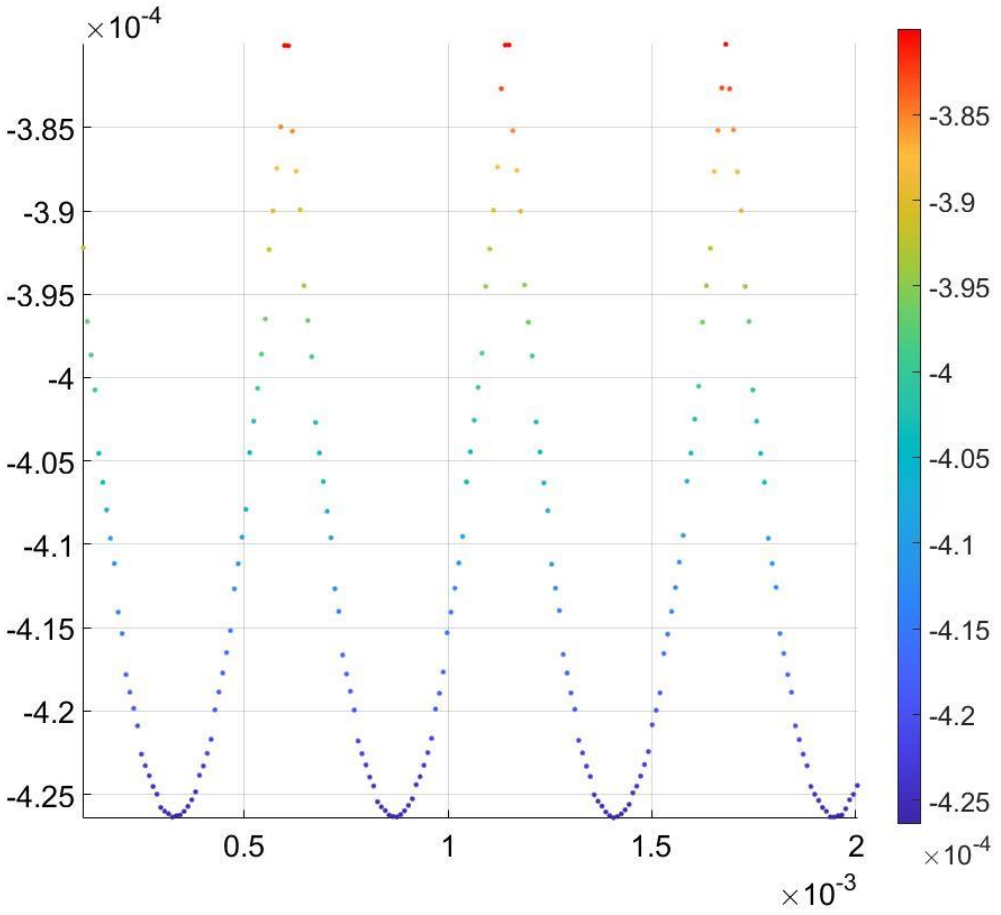

Figure 31. Point cloud of the feed mark's profile (dimension in m)

5.2.4. Reducing the computing time

In the early stages, the model was run using a function called 'Live Script'. This function produces a graph and output, and is highly flexible allowing the user to amend the input values. However, this function uses computing power continuously to show each step of the calculation. This makes the computing time longer than expected. To reduce the computing time, the 'Live Script' has been converted into a normal 'Script' in which the system only produces a result at the end of the calculation. This significantly reduced the computing time. Sample code has been created to test the time difference between 'Live Script' and 'Script'. The result showed that the 'Live Script' finished in 22 seconds and 'Script' in 19.1 seconds, i.e around 13% faster. And another technique in MATLAB is adding semicolon (;) at the end of each line, this function hides and suppresses the output in the

command window so the computer does not require to use the power to show the output during the run of the code. Previous sample code has been used to test the semicolon function, and the result showed that the code without semicolons took 109,481 seconds to finish the run and code with semicolons only used 0.34 seconds.

On the other hand, the code combined the cutting trail and filtering parts into a single script to generate the final surface. However, the time it took to generate the result was long and had the disadvantage that it was not possible to see any problems until the end of the process. Therefore, the code was divided into two parts, the first to generate a point cloud representing the movement of the cutting edge and the second to filter the point cloud to generate the cut surface. This adjustment may not reduce the total time required to generate the surface at this stage, but it ensures that the cutting trail is sensible before moving to the filtration part.

The code was therefore modified to create segments within the cutting trail usable in the filtration process, but not all of them. By knowing that the depth of cut for the cutting parameter is the maximum z value, the code was modified to only create points within the pre-set depth of cut limit, as shown in Fig 32. This example has a tool radius of 5mm, feed rate of 0.5 m/s, spindle speed of 12000 rev/min, lead angle of -30° and total of 3 revolutions for a three cutting edges trail. The depth of cut limit has been set to 3 mm. Therefore, the result only shows points below 3 mm. This result differs from the previous results as points above the depth of cut limit were eliminated. However, as the depth of cut limit is set relatively high and the beginning of the cutting trail still shows the lead effect, this confirms that the model is still generating the previous cutting parameters setup and has correctly cropped points above the depth of cut limit.

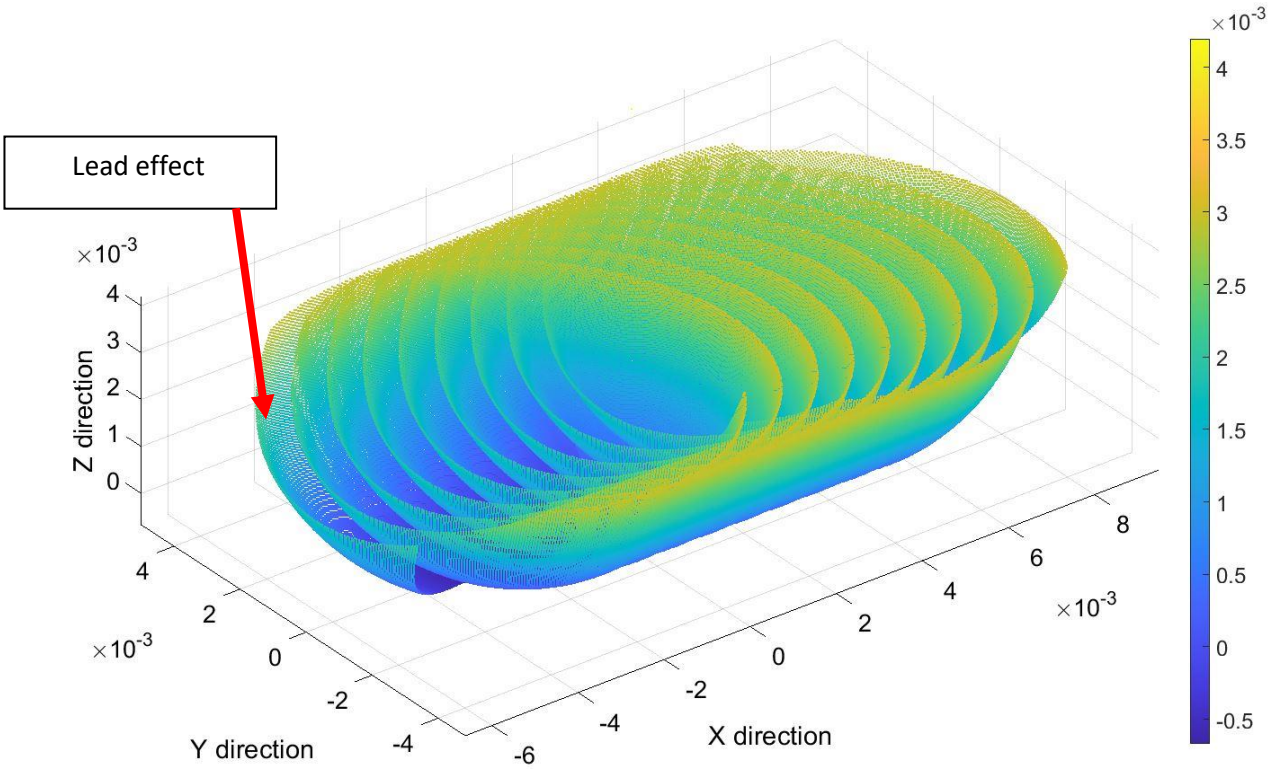

Figure 32. Point cloud of a top cropped cutting trail (dimension in m)

This step reduces the computing power required as the code produces fewer points than before. This also benefits the filtration process as the system loops through fewer points.

New filtration code was developed as mentioned in 5.2.2, which reduced the computing time even further. A test was carried out to calculate the time difference between the original filtration code and the latest code. The result showed that the original filtration code used 53.7 seconds and the latest code only used 2.6 seconds to create the same result.

5.3. Result

5.3.1. Visual validation

A previous researcher developed a set of cutting parameters for the actual cutting experiment described in chapter 6.1. The simulation here used sample EAC 1-1 and the detail is shown in Table 3.

Table 3. Cutting parameter of the sample EAC 1-1

Feed rate	**Spindle speed**	**Cutter radius**	**Lead angle**	**Tilt angle**	**Helix angle of the cutter**	**No. of cutting edge**	**Total revolution**
0.0324 m/s	12,000 rpm	1 mm	-55°	0°	30°	3	2

First, the cutting trail with the top cropped was generated and is shown in Fig 33. The tool tip mark is not at the bottom of the simulated model which indicates that the imaginary cutting tool was leaning backward when the cutting trail was generated. Also, the tool tip mark is aligned with the y axis, so there is no tilt effect in this model. However, the width of the cutting trail is less than 2 mm in the model, because the top of the model has been cropped as mentioned in the previous section. Therefore, this model does not present the full width of the cutting trail. The result shows that the cutter was turning in a clockwise direction and the feed direction is from negative to positive x values.

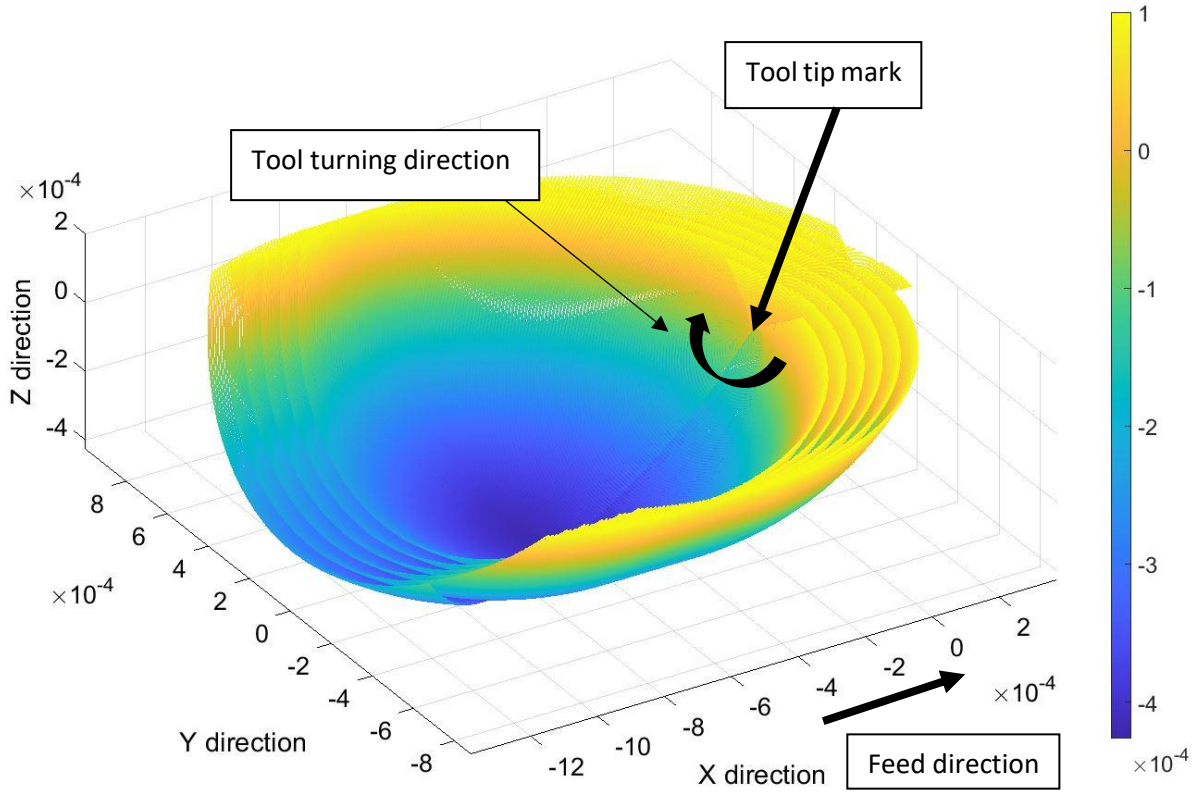

Figure 33. Result of simulating a cutting trail (dimension in m)

Second, the cutting trail result was filtered resulting in a final surface, as shown in Fig 34 & 35. As shown, the pick-interval cusp marks (U shape across the y direction) have clearly been generated. However, it does not show the feed mark as clearly as in Fig 29. This is because the feed rate is lower than the previous example, hence the feed marks are insignificant.

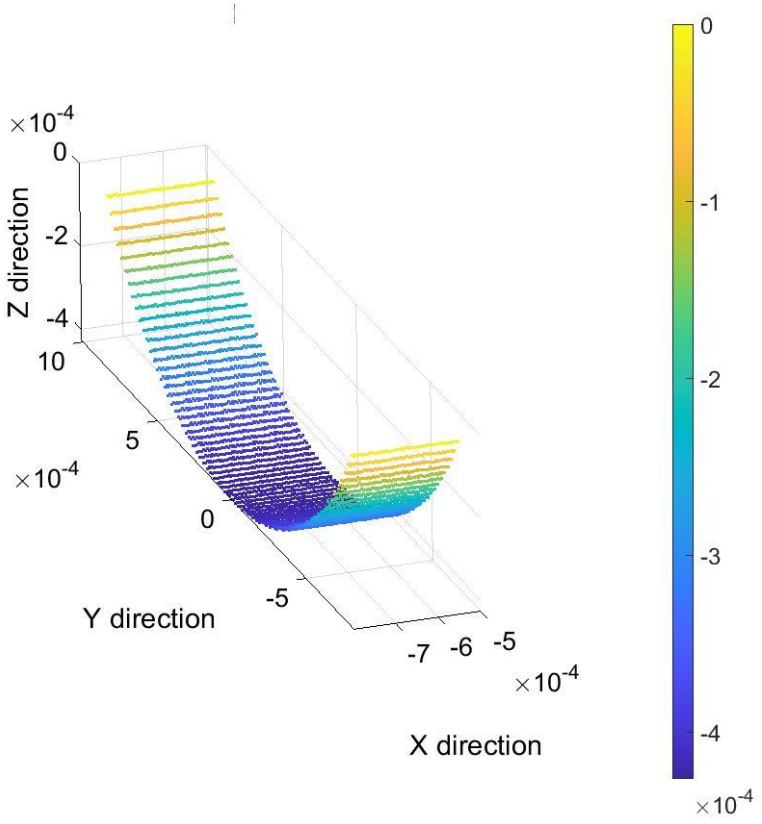

Figure 34. General view of the surface result (dimension in m)

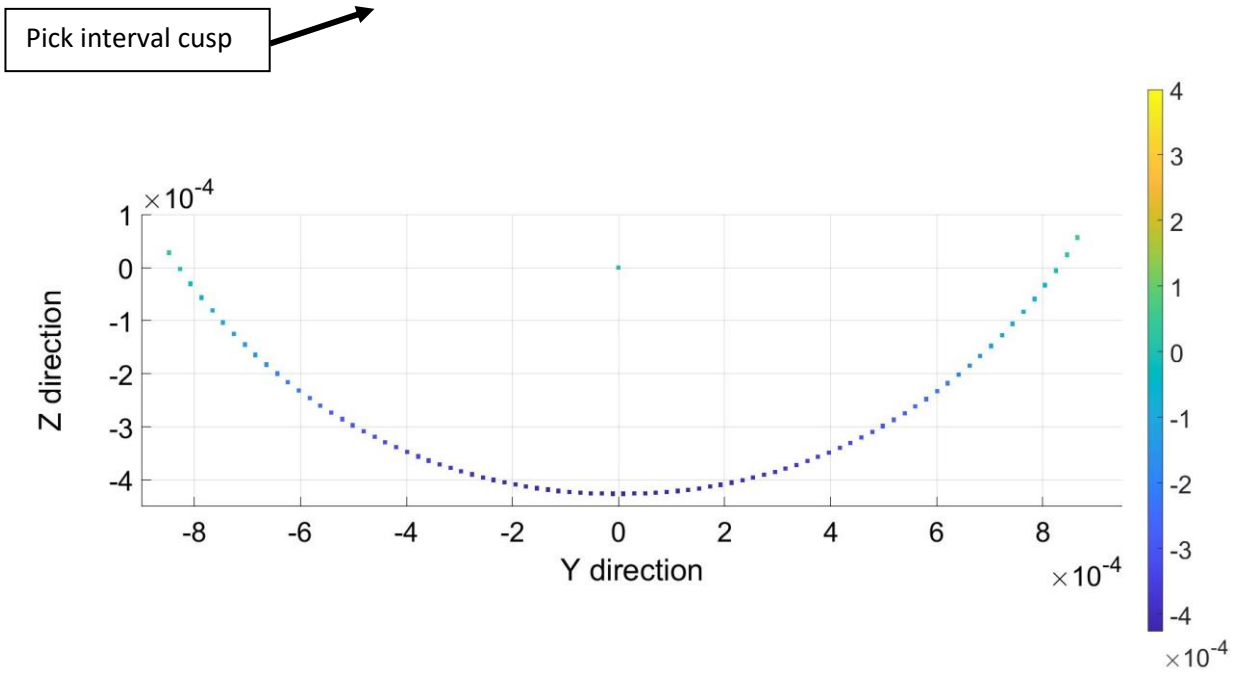

Figure 35. Front view of the surface result (dimension in m)

Finally, a profile within the surface result has been selected for a further investigation using the method described in section 5.2.3. The profile at y = 0 has been selected from Fig 34 for investigation as shown in Fig 36, the fine detail of the profile shows that there is a vertical movement which is the feed mark.

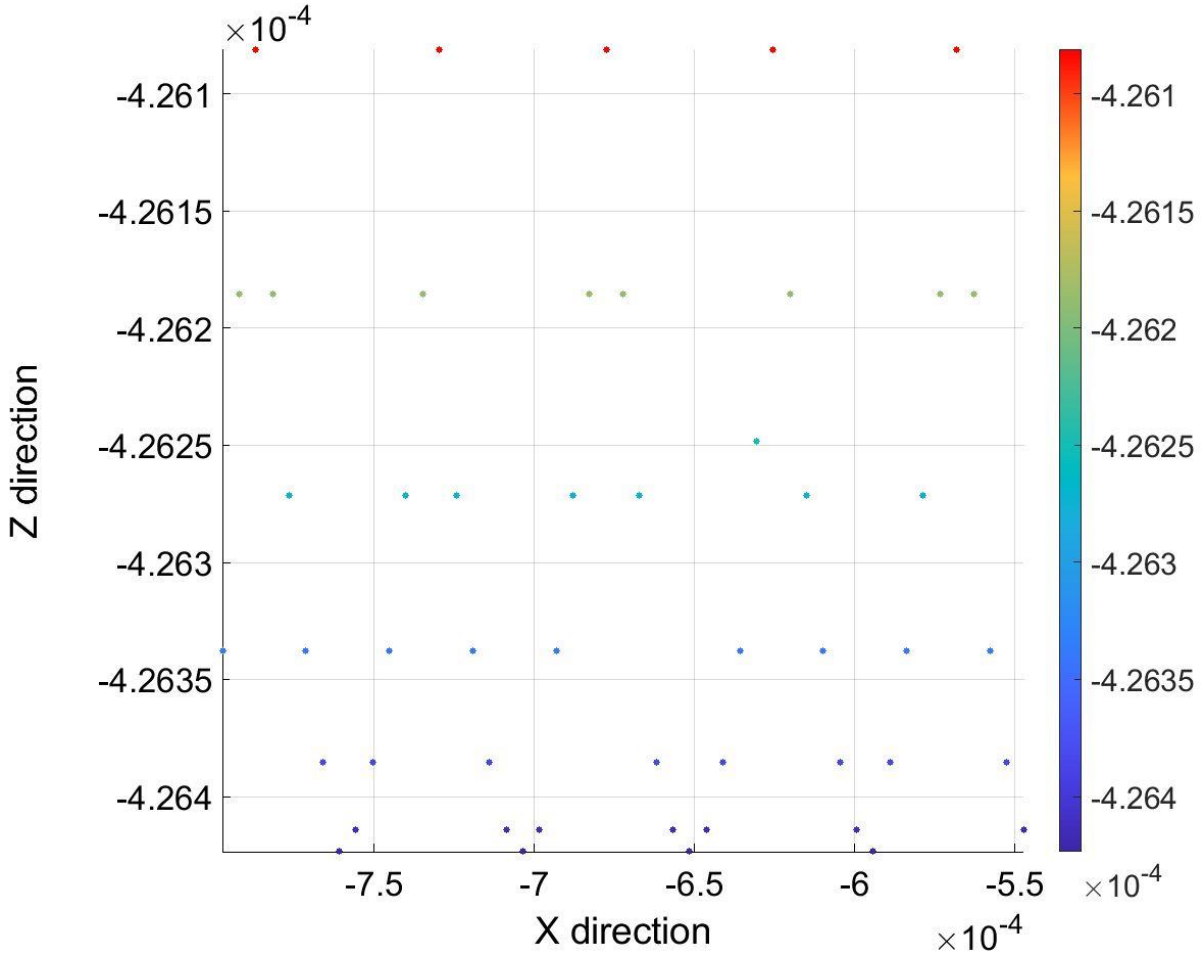

Figure 36. The profile at y=0 of the final surface for the EAC1 specimen (dimension in m)

Another result from the previous example shown in Fig 29 for the profile at y=0 is given in Fig 37. This example used a feed rate of 0.324 m/s. The result shows that the resolution of the profile is greater than the previous result.

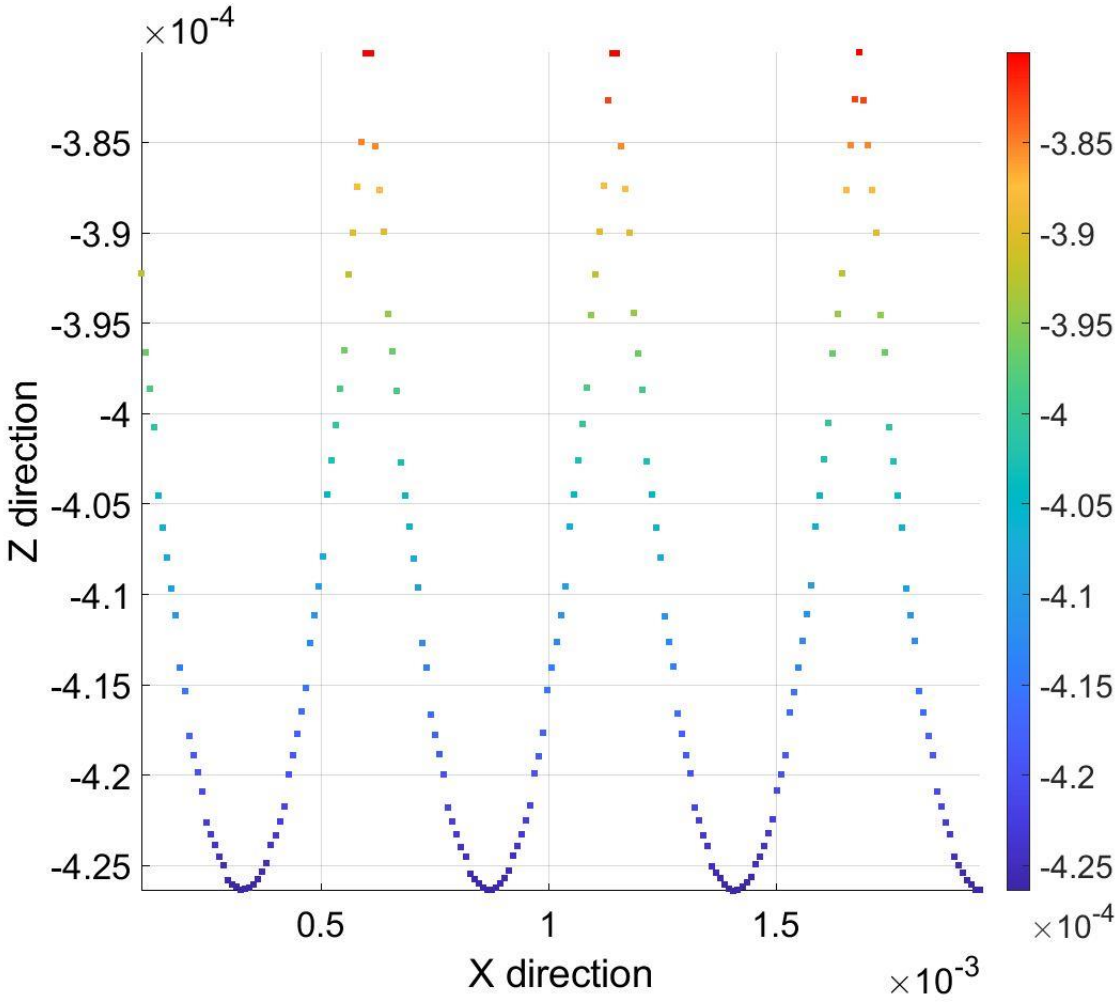

Figure 37. The profile at y=0 of the final surface for the EAC1 specimen with 10x faster feed rate (dimension in m)

5.3.2. Mathematical validation

To validate the feed marks, the distance between two feed marks must be calculated. In order to find the distance, the units of the original feed rate needs to be converted. The feed rate in the specification used metres per second, and is converted into millimetres per minute using the 1944 mm/min associated with a spindle speed of 12,000 rpm. as shown below.

$$0.0324m/s \ * 60s * 1000mm = 1944\, mm/min$$

The distance for each revolution can be found as shown below.

$$\frac{1944\ mm/min}{12000\ rpm} = 0.162\ mm/rev$$

In this experiment, the cutter has three cutting edges. Therefore, the distance for each revolution can be used to calculate the distance between two feed marks, as shown below.

$$\frac{0.162\ mm/rev}{3} = 0.054\ mm/cut$$

In Fig 36, the distance between the start and end of the first feed mark is 0.0572 mm, and those between the start and end of the second and third marks are both 0.0521 mm. The distance for one revolution is 0.161 mm. Therefore, the difference between the theorical calculation and the actual result from the MATLAB of a single revolution distance is less than 1%. However, the differences between feed interval cusp marks are 5.6% and 3.6%. This is because there are too few points for the system to generate an accurate result. Table 4 shows that the interval for an x value with the same z value are different with results of 0.06 mm and 0.05 mm. The resolution setting determines the point generation and filtration, affecting the final result and leading to the difference.

Table 4. Table of the x and z value of the EAC1 specimen profile at y=0

x (mm)	z (mm)
-0. 79	-0. 43
-0. 73	-0. 43
-0. 68	-0. 43
-0. 63	-0. 43
-0. 57	-0. 43

In Fig 37, the distance between the start and end of each feed mark is 0.542 mm. The distance for one revolution is 1.62 mm. The result should be 10 times greater than the previous result. This result is more accurate and proves that the model generates results that match the theorical calculation. However, it also shows that the resolution and the accuracy of the final result depend on the feed rate associated with the tool radius.

Ra has also been obtained for the EAC 1-1 sample on the centre of the pick interval cusp. The result from the MATLAB code was 93.33 nm. The result from inspection of the same area of the cusp averaged 457.33 nm. The actual result is a 5 times greater than the simulation. This is because the measured surface contained defects created by tool edge wear and tool vibration. These factors created rough cusp edges and uneven cusp depth across the sampling area and the simulation assumed perfect conditions. This model is a foundation and can be further developed to include kinetic effects such as tool vibration, tool run out and tool wear. It is not possible to include elastic and plastic deformation in the MATLAB code at this stage as it involves the calculation of cutting force and temperature.

5.4. Conclusion

This chapter can be summarised as follows:

- Time increments per revolution have been incorporated in the code to fix the number of time increments for each revolution no matter how many revolutions are simulated in the model.
- A step to filter the cutting trail into a final surface and surface profile has been developed. These steps aim to simulate the final cut surface and illustrate the feed interval cusp marks within the pick interval cusp.
- The cutting model has been optimised. The code has been moved from 'Live Script' to 'Script', this step saves time by not generating an answer for every single line. The code has been separated into two parts, cutting trail generation and filtration. This step allows the user to inspect the cutting trail before starting filtration. Although this step does not reduce the computing time overall, the user can inspect the cutting trail to ensure there are no issues and save time by not filtering incorrect cutting trails.
- The time for surface filtering was reduced by reducing the number of points that the model needed by only generating the part required for filtering.

- The final surface was generated by adding a filtration routine to filter the lowest points in each pre-set grid from the cutting trail generation.
- The surface roughness parameter Ra was calculated by adding a filtration routine to filter points from the final surface into a profile and the equation for calculate the Ra. The Ra value from the actual result is 5 times greater than the simulation because the actual result contained defects from tool vibration and wear on the surface, leading to a higher value of Ra.
- The surface result has been validated mathematically. The result with the original cutting parameters has a maximum difference of 5.6%. The result with 10 times faster feed rate is identical to the theorical calculation.
- The model accuracy is directly proportional to the feed rate. The faster the feed rate, the greater the accuracy of the model results.

6. Experimental measurements

Some of the work presented in this chapter has previously been reported in Chan and Walton (2021).

6.1. Work-piece inspection method and material

There are two types of 5-axis milling machine currently in use in the University of Huddersfield laboratory. The first machine, the HURCO VMX30Ui, is for low volume and weight workpieces. Its specification is shown in Table 5. This machine bed moves in the x and y directions and rotates in the A and C directions as shown in Fig 38. The spindle only moves in the z direction.

Figure 38. AC type 5-axis milling machine with moving bed

Table 5. HURCO VMX30Ui machine specification

X, Y, Z Axis Travel	762 x 508 x 520 mm
A-Axis Travel	+30°/-110°
Spindle Nose to Table (Min-Max)	90 mm / 610 mm
Table Diameter	248 mm
Max. Weight on Table	200 kg

T-Slot Size	6 x 12 mm x 60°
Max. Spindle Speed	12,000 rpm
Peak Spindle Motor	13.4 kW @600 rpm
Spindle Torque (peak - 1 min)	214 Nm @ 600 rpm

The second machine, called GEISS and shown in Fig 39, is intended for high volume and weight workpieces. The machine bed does not move, and the spindle alone moves in the x, y and z directions and also rotates in the A and C directions. The maximum spindle speed of this machine is 24,000rpm and the maximum feed rate is 70 m/min.

Figure 39. AC type of 5-axis milling machine with fixed bed

A series of 120 mm by 25 mm by 5 mm dog-bone shaped Aluminium alloy samples were machined using the HURCO VMX30Ui 5 axis milling machine. The pick interval cusps were machined on the middle of the sample as shown in Fig 40 and the cutting parameters are given in Table 6. These experimental examples were created as part of the research by Barrans et al. (2017). The cutting tool used in this experiment was a 2 mm diameter ball end cutter with three helical cutting edges.

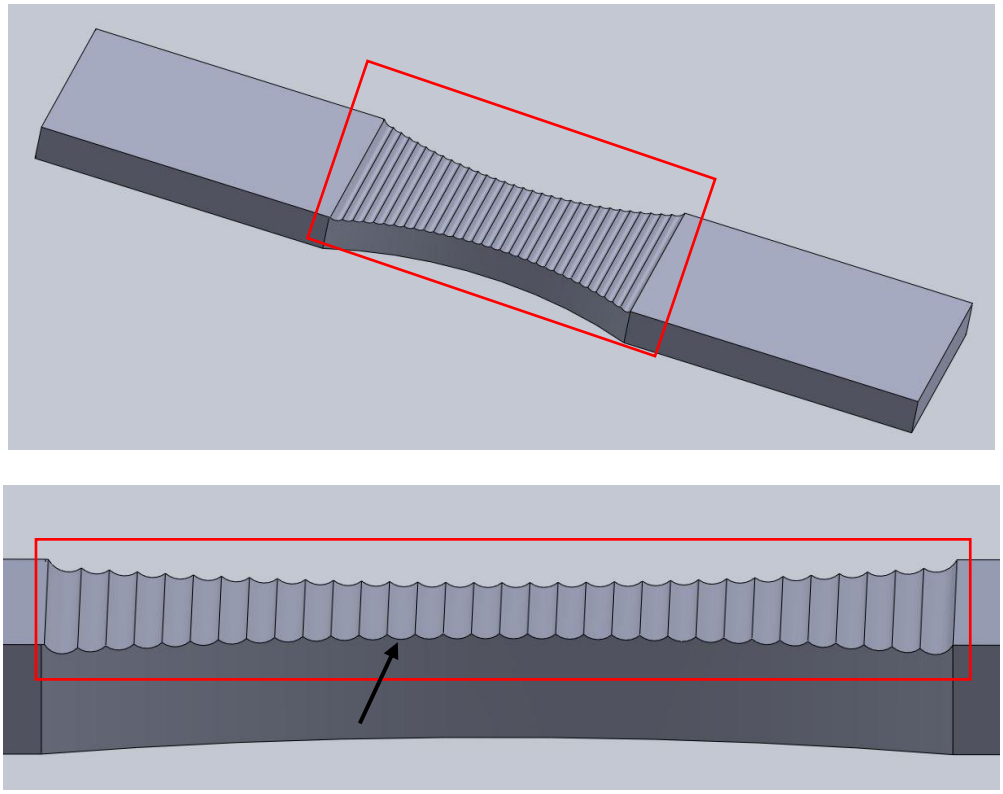

Figure 40. CAD model of the sample (the red square represents the machined area)

Table 6. The cutting parameters for samples

Feed Rate(mm/Min)	Tilt Angle	Lead Angle	Quantity	Specimen ID
972	0	-55	2	**BAC1**
1273	0	-55	1	**CAC1**
1944	0	-55	2	**EAC1**

Surface inspection was carried out using an optical 3D measurement system (Alicona Infinite Focus Measurement G4), as shown in Fig 41.

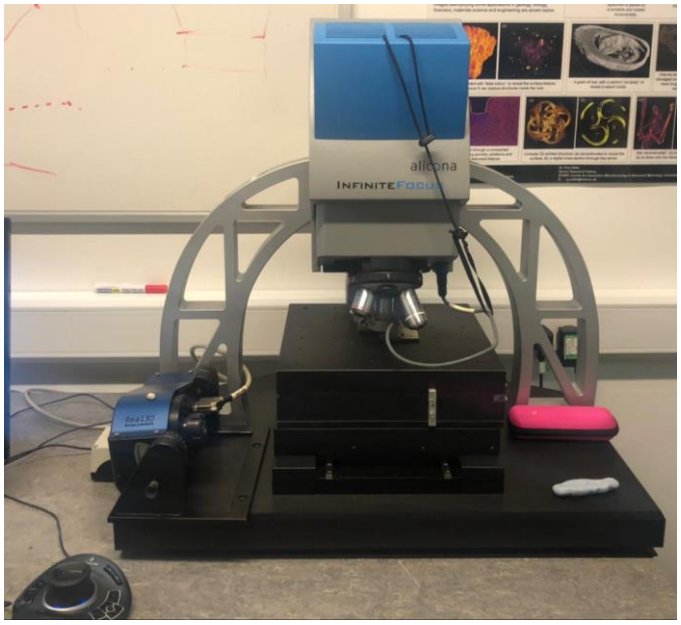

Figure 41. The setup of the Alicona Infinite Focus Measurement G4

This machine measures the surface topography without making contact. This type of profilometry uses a microscope to capture an image of the surface and analyse the depth of field using the variation in focus, subsequently reconstructing a 2.5D area and determining the topography of the surface. A magnification of 20x has been used to inspect an area approximately 4 mm x 4 mm x 300 µm, including at least 6 cusps in each inspection. A fixture was made to secure the samples to the inspection bed. This step ensured that each sample was aligned accurately along the x and y axis. The estimated vertical resolution was 0.2172 µm and the lateral resolution was 2.9063 µm. Since the machine must divide the whole area into individual fields and scan each individually in order to maintain the resolution, the individual images must then be merged by matching pixel heights to create the full image. The overlap between individual images was 10%. In this study, all samples had the same cutting lead and tilt angle of -55° and 0° respectively, the spindle speed was 12,000 rpm, the tool diameter was 2 mm, and the cutting style was push. Other specifications and code numbers are given in Table 7.

Table 7. Samples specification

Converted Feed Rate (mm/min)	Code number	Expected feed interval mark distance (mm)
972	BAC1	0.027
1273	CAC1	0.035
1944	EAC1	0.054

6.2. Scales of the samples

Fig 42 shows one of the samples with 6 cusps with cusp marks, feed marks, tool marks and defects. On the macro scale, defects can be seen which are potentially caused by material imperfections, tool run out, tool vibration, tool wear and microscopic particles left on the surface before inspection. Although all samples have been cleaned with alcohol cleaner on a fabric towel, fine dust may still remain on the surface which create an error on the final inspection result. In order to investigate the cusps with as little error as possible, cusp selection was performed. Fig 42(b) shows details of a selected area in one of the cusps in Fig 42(a). This meso-scale view of this sample shows feed marks on the surface, which are equally distributed throughout the cusp. The feed marks vary according to the feed rate. Fig 42(c) shows the detail in Fig 42(b) illustrating the tool marks. The micro-scale view of this sample shows tool marks which differ from the feed marks. The most significant difference between feed marks and tools marks is that feed marks occur regularly on the surface, but tool marks appear randomly within the feed marks. Tool marks are potentially created by tool wear, which leads to defects on the tool edge, and by aluminium oxide, created during the cutting process, adhering to the tool edge.

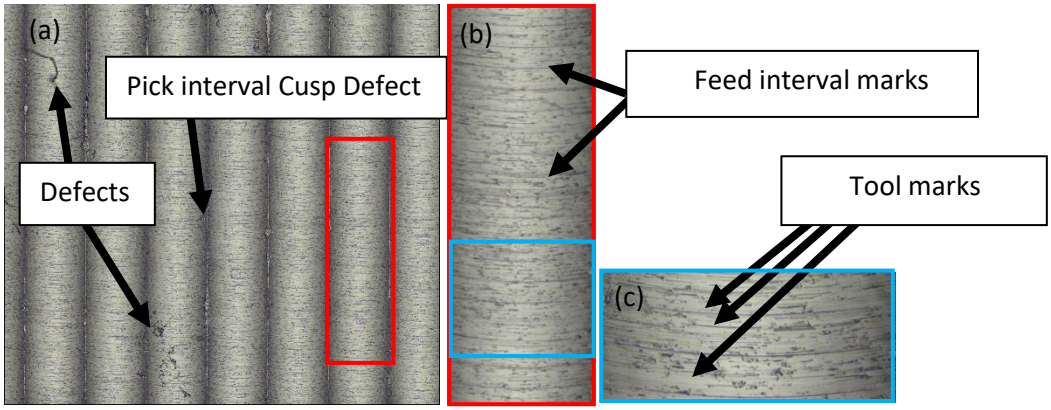

Figure 42. (a) Alicona inspection results at macro scale (Sample BAC 1-1) (b) Meso scale (c) Micro scale

6.3. Feed-interval cusp mark

Most research has concentrated on a general review of cusp mark generation at the macroscopic scale. However, there is a lack of research into these surfaces at the meso- and micro- scales in terms of the surface roughness resulting from marks within the cusps, since the surface roughness is dominated by the cusp height. Here, the meso-scale is defined as the feed marks within the cusp generated by the kinematics of cutting-edge rotation and potential defects at that scale created by tool vibration and tool run out. The micro scale is defined as the machining marks between each flute of the cutting tool. These marks are identified in Fig 43 and this example is from the compressor wheel shown in Fig 4. However, the compressor wheel was machined by an external company so the cutting parameters are confidential. Therefore, the surface marks on the specimen surface described in section 6.1 and the compressor wheel surface shown in Fig 43 are different. It also shows that the curved tool marks on the surface arise because the ball end cutting tool has a helical profile.

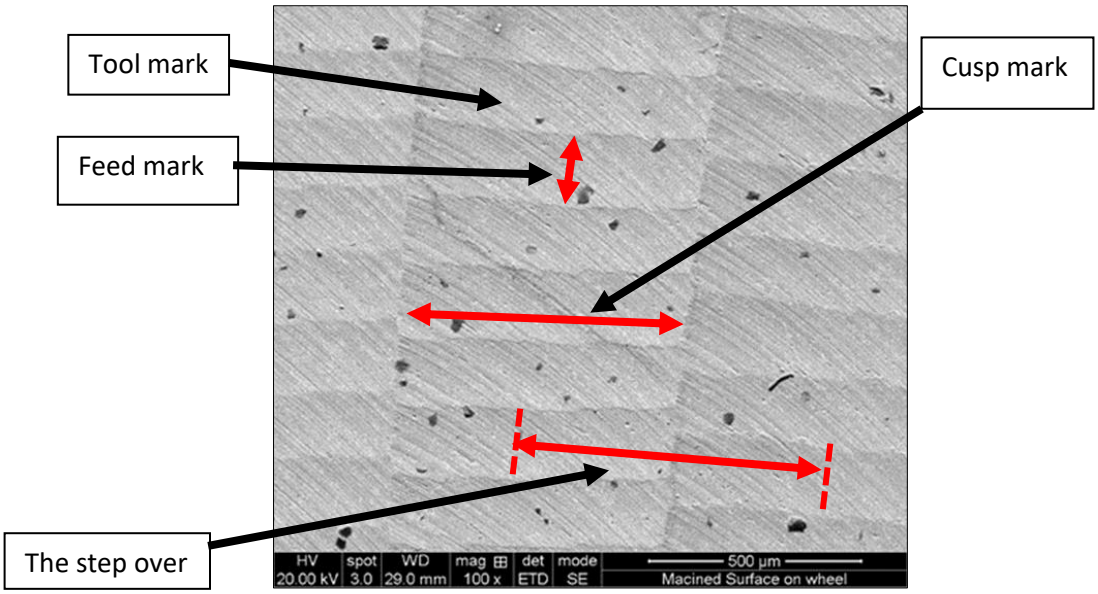

Figure 43. Illustration of Cusp, Feed and Tool mark

At different scales, the surface can be represented by different wavelengths. The macro scale surface can be described by its form, which in this study will refer to as the cusp. The meso-scale surface can be described as waviness, referring to the feed marks. Finally, the micro scale of the surface can be described as roughness, referring to the defects. These different scales are illustrated in Fig 44.

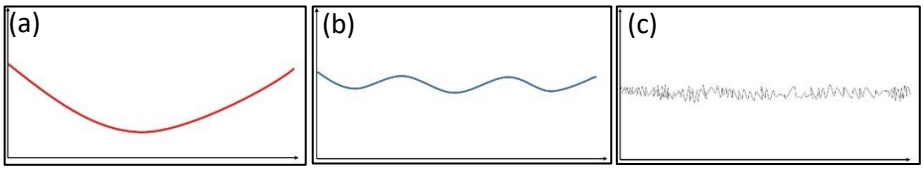

Figure 44. The illustration of (a) form, (b) waviness and (c) roughness

6.4. Cylindrical form removal

The Alicona has a form removal function that allows the user to remove a geometric primitive form, including a cylinder, from the surface. This form removal function aims to remove the corresponding shape but does not affect the other features of the surface. In this section, an individual cusp created by the ball shape cutter relative to the cutter diameter can be transformed from a cylindrical shape

into a flat surface. By selecting the cylindrical form area, the software can automatically define the cylindrical shape and transform it to a flat surface. This step allows the user to investigate the surface within the cusp without the effect of the cusp profile. Subsequently, area roughness parameters can be calculated from the decomposed result. Otherwise, the pick-interval cusp mark always dominates the overall surface roughness. However, this function has a disadvantage in that it can only remove one form at once. In this study, each inspection contains at least 6 cusps, therefore it is necessary to manually crop the surface to a single cusp so that the system can recognise the cylindrical shape. This step creates another issue when the edge of the cusp has defects, which affect the result and the form removal process. Therefore, the edges of all the cusps must be cropped Fig. 45 shows an example before and after cylindrical form removal. The system determined the radius of the cylindrical shape to be 998.8 µm, which matches the tool radius of 1mm. The surface depth of the original cusp surface (Fig. 45 left) is dominated by the two sides of the cusp as those areas are the highest and the middle of the cusp is the lowest in general. The surface after the form removal step (Fig. 45 right) shows uniform feed marks.

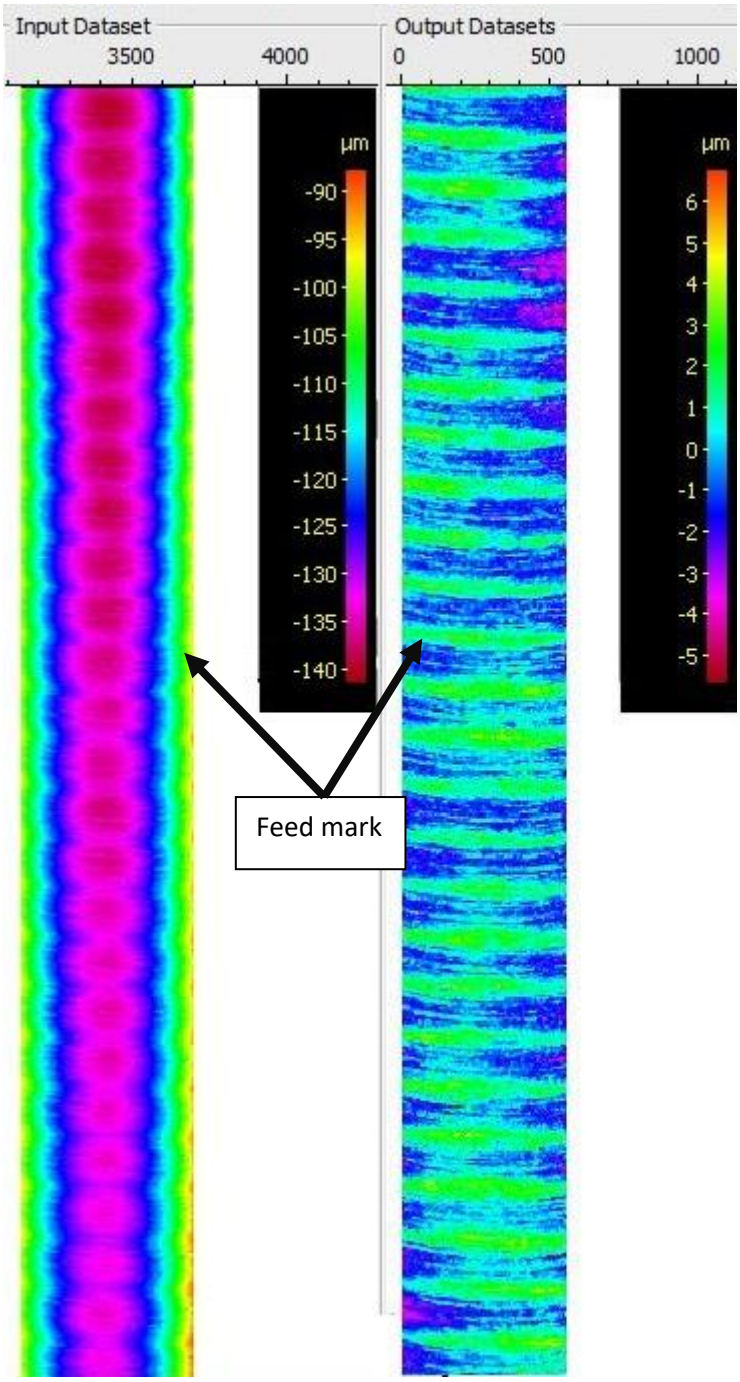

Figure 45. Original depth of sample EAC 1-1 (left), Depth after the form removal (right) (dimension in µm)

Fig 45 shows a before and after overview of one cusp of EAC 1-1. This example clearly shows that the height is dominated by the sides of the pick interval mark before the form removal process. Feed

marks can still be seen through the cusp. In the post-processed example, feed marks are clearly shown throughout the cusp.

The other angle of the 3D view shown in Fig 46 shows that the bottom of the cusp has been transformed from a cylindrical shape into a completely flat surface, but all the features of the surface remain unchanged. This example shows the same big features as in Fig 46. The big defect at the top has clearly been transferred and remains in the same position, another example of a deep feed interval cusp mark on the bottom has also clearly been transferred.

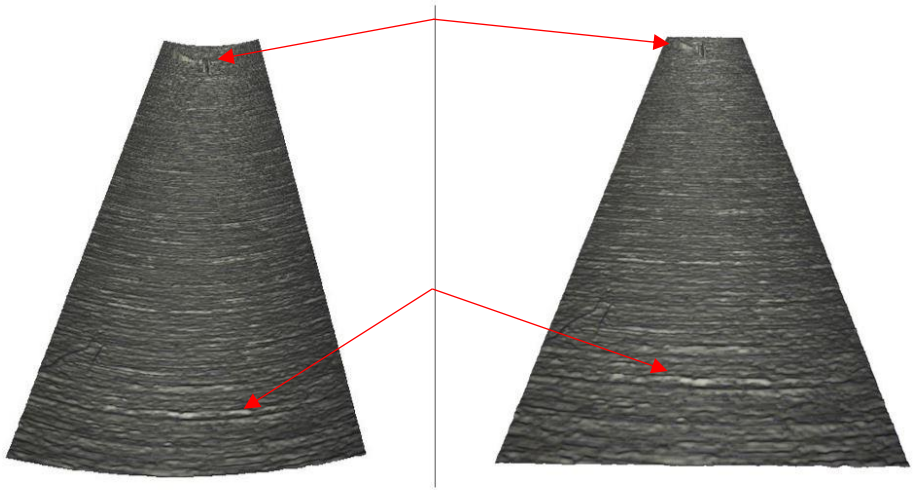

Figure 46. Before cylindrical form removal (left), After cylindrical form removal (right)

6.5.SurfStand inspection software

6.5.1. Filtering process

6.5.1.1. Wavelet filtering

Wavelet filtration (Multi-Scale Analysis) is a filter that determines the proportion of a signal that is accounted for by a specified wavelet at a pre-set scale and location. This filter allows the user to select a range of pre-set wavelets from 0.008mm to 8mm and to show the selected data. The longest and

shortest wavelets for the surface were 0.05mm for the pick interval mark and 0.009mm for the feed interval mark, which were within the system limits that the system could process. However, this function has 8 pre-determined sets of wavelet range for the user to select from rather than a user pre-set value. In this case, the longer wavelet range sets correspond to the cusp marks, the middle sets to the feed interval marks and the shorter sets to the tool marks. In this step, the middle (0.025mm) and shorter (0.008mm) wavelet range sets were selected to illustrate the feed interval marks and tool marks. After selecting the wavelet range, area roughness parameters can be calculated from the result. However, this approach has the disadvantage that the user does not have control over the exact value of the wavelet when using this software. This setup affects the results at different feed rates especially, as the feed rate affects the feed interval distance. As mentioned in section 5.3.2, the distance between two feed marks in sample EAC 1-1 was 0.054mm/cut. The same calculation with the slower feed rate of sample BAC 1-1 gave a distance between consecutive feed marks of 0.027mm/cut. Therefore, the wavelet can differ, and it might not be possible for the user to select the exact preferred value of the wavelet in this approach. Also, there are some features that contain different data but have similar wavelets. This approach could not separate different features with similar wavelets. This also affects the calculated surface roughness parameters.

Wavelet filtration was carried out. The results before and after the filtering process are shown in Fig 47 & 48. The example shown in Fig 47 is the pre-process cusp, where the height of the cusp is dominated by the pick interval cusp at the side of the cusp. There are some feed interval marks within the cusp. The post-processed example is shown in Fig 48. This filtering process used 0.008mm as the shortest and 0.025mm as the longest wavelet to try and filter the cusp surface into a flat surface. Although the surface has been flattened, the result shows that it recognised the side of the pick interval marks as a wavelet and removed most of the feed interval marks. Noise also appeared across the centre of the pick interval cusp.

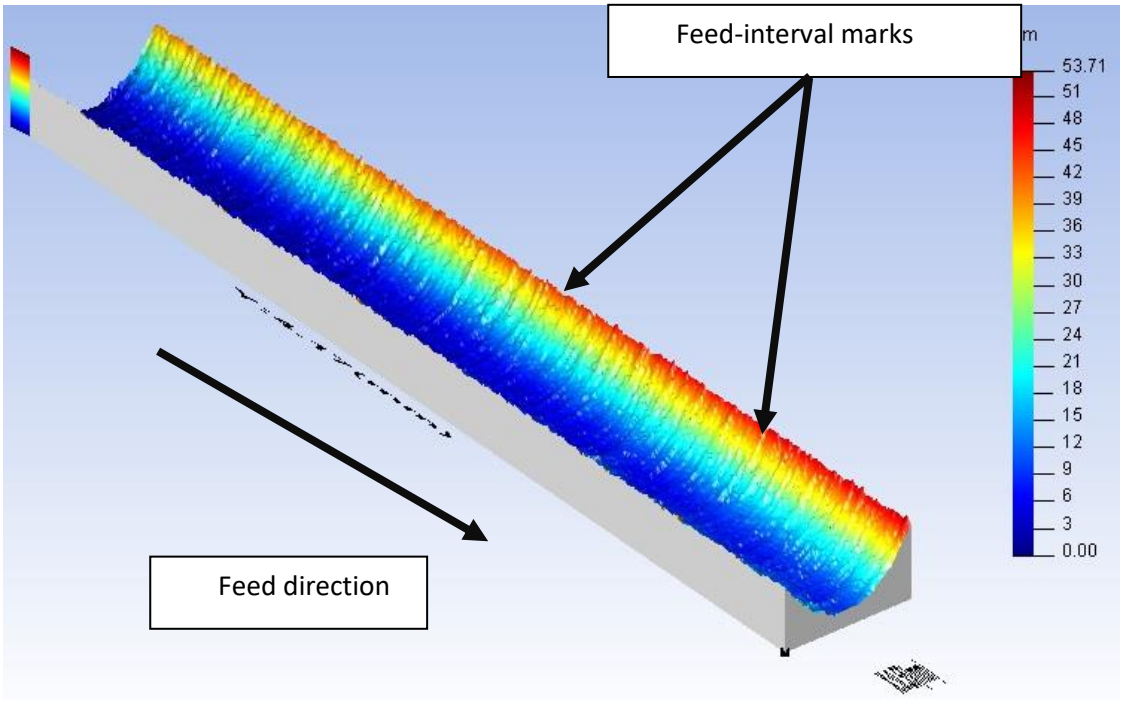

Figure 47. Cusp before wavelet filtration process

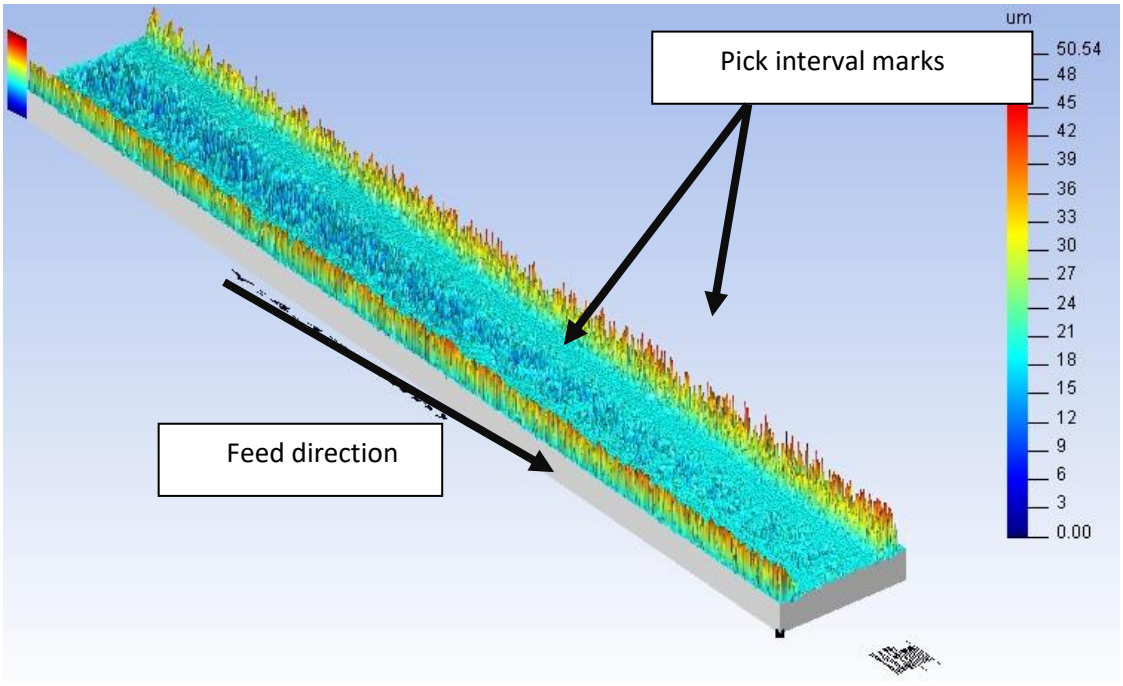

Figure 48. Cusp after wavelet filtration process

Another test that was conducted was multiple cusp filtering. A pre-processed image is shown in Fig 49. The visual result seems visually to have removed the cusp effectively, as shown in Fig 50. However,

the centre shows some noise, and the sides of all the pick interval marks are still dominated by the surface height.

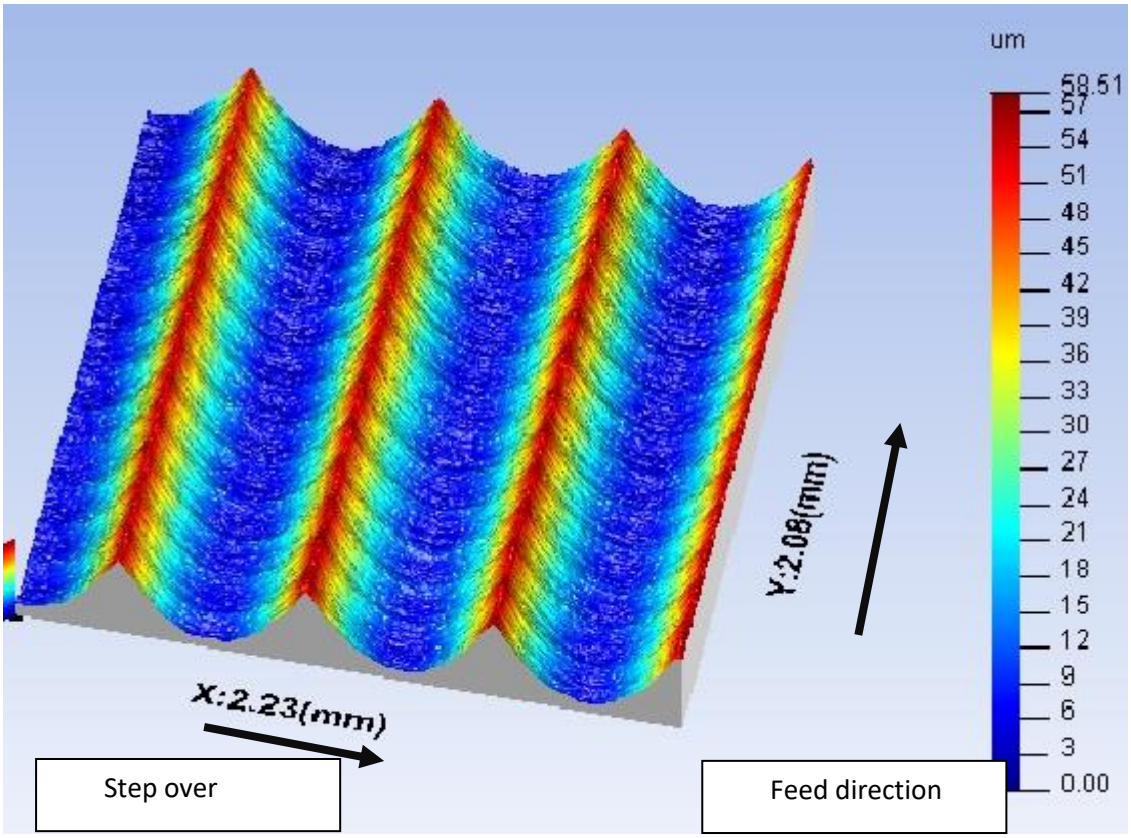

Figure 49. Multiple cusps before the wavelet filtration process

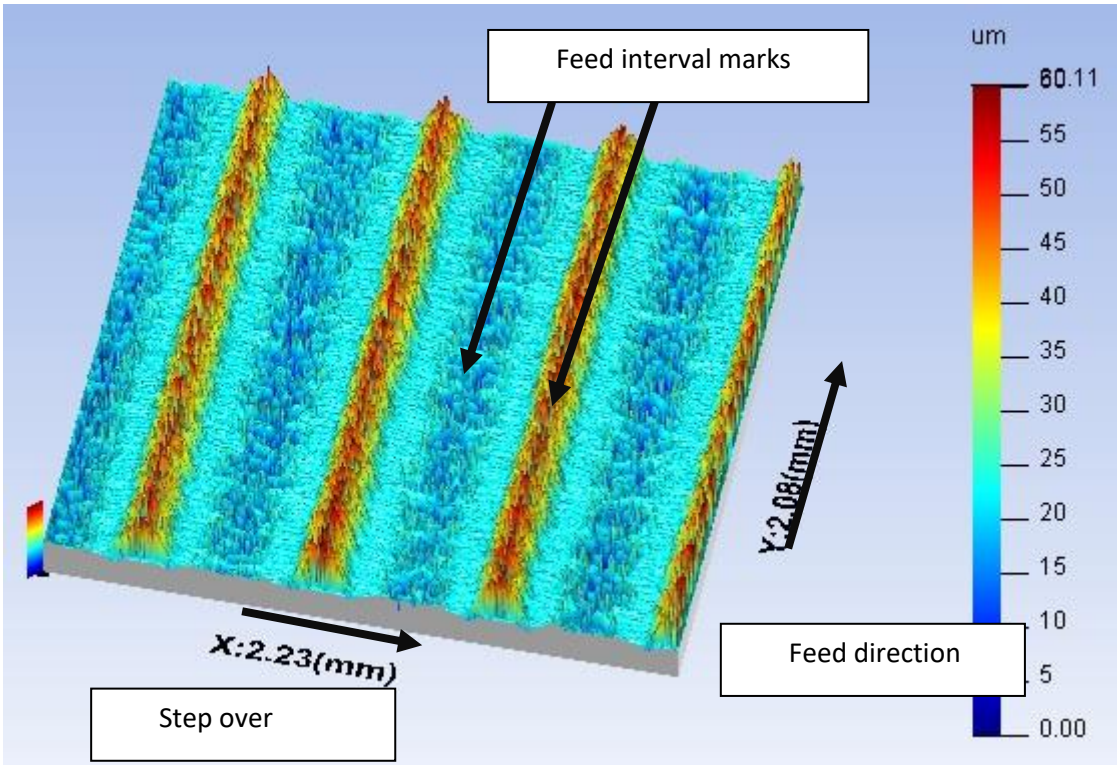

Figure 50. Multiple cusps after the wavelet filtration process

Mathematical validation is not possible here because there was noise on the surface so that the feed interval mark could not be defined.

Wavelet filtering has been used with the aim of removing the pick interval marks on the surface. However, this filtering function is limited to a certain range of pre-determined sets of wavelet value and the wavelet value used to filter the surface cannot be selected manually. Therefore, this function is not suitable to remove the pick interval mark effectively.

6.5.1.2. Polynomial fitting

Another approach in the SurfStand software is polynomial fitting, which is a form of regression analysis to model an independent variable x and a dependent variable y with an n^{th} degree polynomial in x. SurfStand can remove polynomial curves from the second order up to the twentieth order. In this study, the cusp can be understood as the second order since the cusp shape is half a complete wavelet.

After the order is set by the user, the software generates the result from second to first order using the least squares method. The limitation of this approach is that multiple cusps cannot be defined as third order or higher, because the cusp marks are not a differentiable surface, and hence cannot be fitted by a polynomial. Therefore, it can only process a single cusp.

A result from using the polynomial fitting technique in SurfStand to remove a single cusp is shown in Fig 51. The height range of the surface feature is between 0 and 8µm. However, noise appears on the surface which affecting the maximum height (Sz) and creating a maximum height of the surface as 23.37µm.

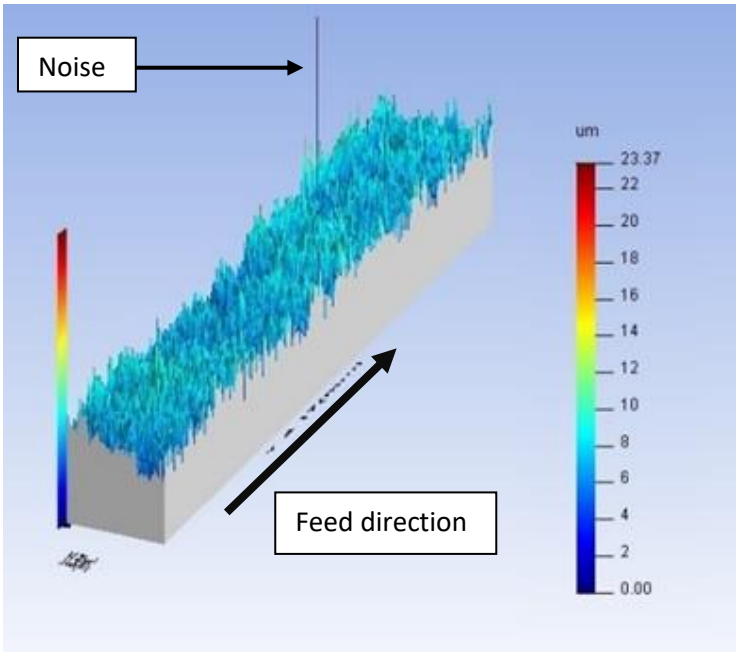

Figure 51. The polynomial fitting in the SurfStand

Fig 52 shows the 2D profile of one of the cusps in each sample (Blue – BAC 1-1, Green – CAC 1-1, Red – EAC 1-1) after polynomial fitting. The sample with the slowest feed rate created a steadier line by comparison with others. This is probably because the faster feed rate generates more vibration and tool run-out during the cutting process. Therefore, those waves are not on the same level as each other. This also explains why the Sa value increases with the feed rate. However, 74 waves should be expected on the red line (EAC 1-1 sample). This result only shows around 25 waves, which might result

from one worn cutting edge dominating the height during each revolution of cutting, and also the inspection did not achieve a high enough resolution to identify the other cutting marks. Fig 53 shows before and after views for the polynomial fitting of the EAC 1-1 sample. The pre-process data has been dominated by the pick interval mark at both sides of the cusp. The post-processed data showed that the pick interval has been removed completely and the feed interval marks are the main effect that dominates the height.

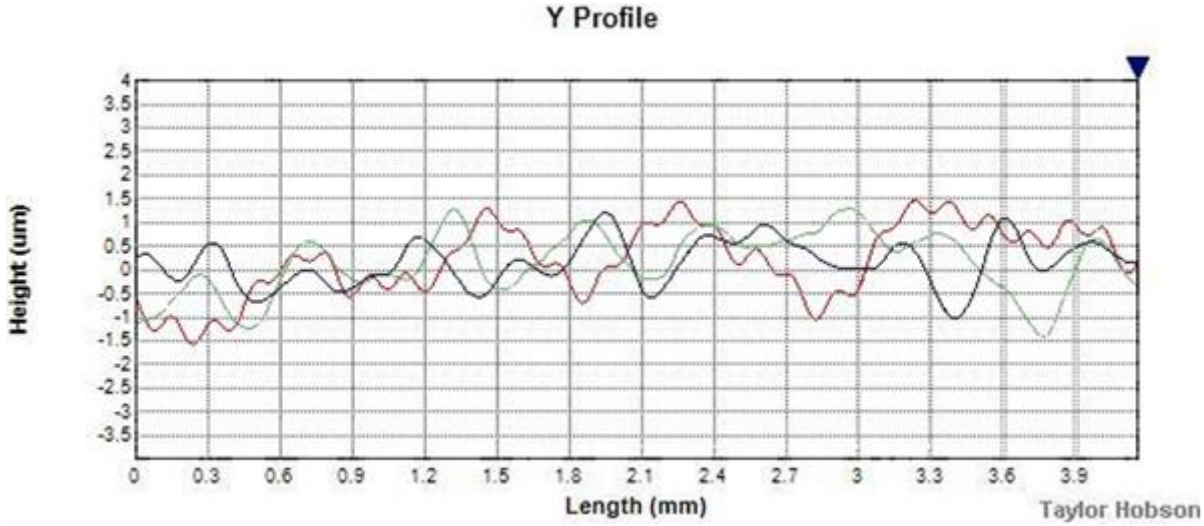

Figure 52. 2D profile of all samples (Blue – BAC 1-1, Green - CAC 1-1, Red – EAC 1-1)

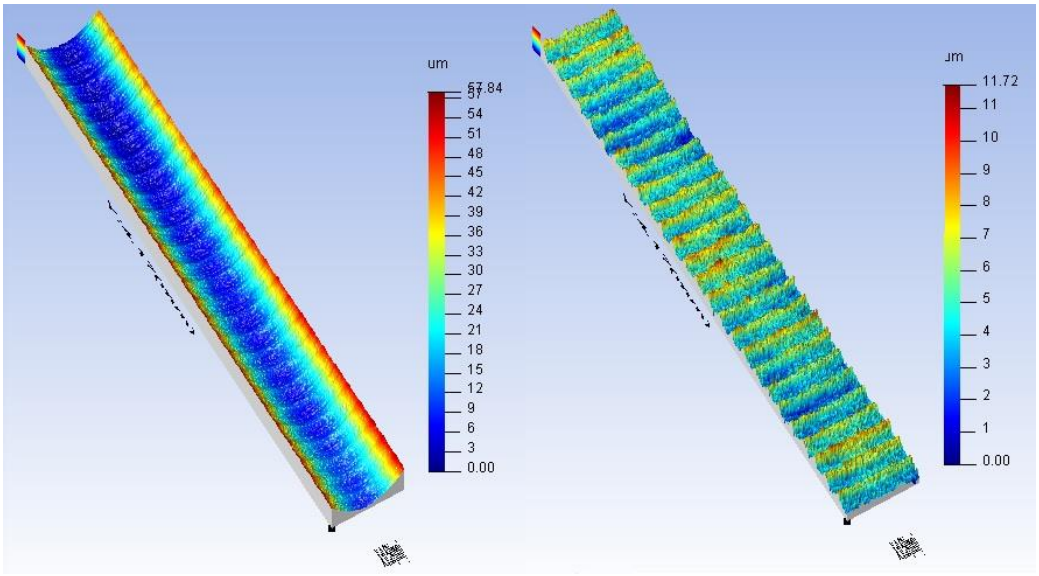

Figure 53. EAC 1-1 sample 3D before (left) and after (right) view of the polynomial fitting

6.6. Results

6.6.1. Mathematical validation

A section of the EAC 1-1 sample extracted from Alicona is shown in Fig 54. This is a part of the section described in section 6.4. The two peaks are located at 44µm and 214µm, and are 170µm apart from each other. The result is only 4.7% difference from the theoretical calculation.

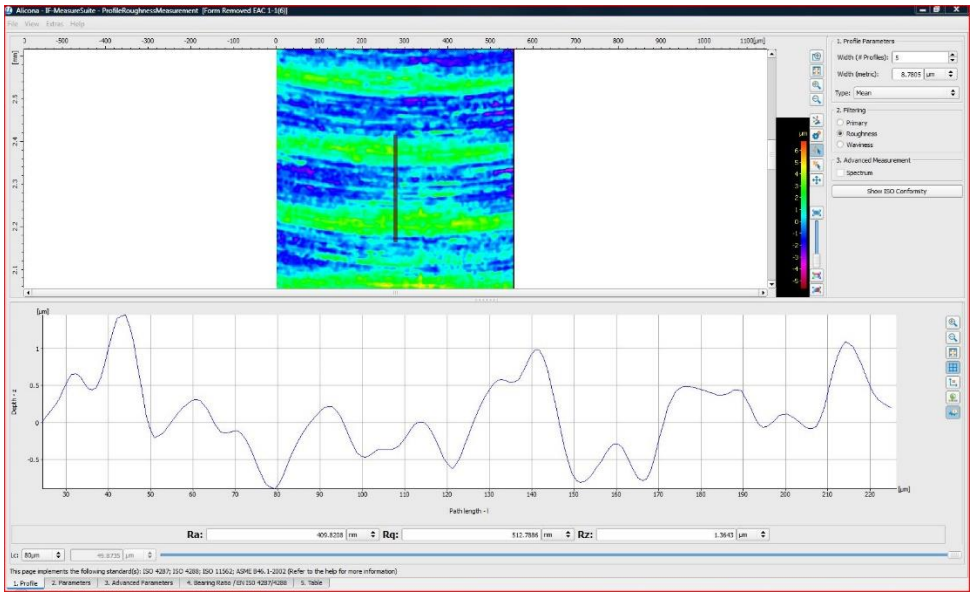

Figure 54. A section of EAC 1-1 after form removal in Alicona

The previous section stated that the slowest feed rate (BAC 1-1) created the steadiest profile, but the feed marks cannot be shown as clearly as possible because of the resolution of the system. On the other side, the profile of the fastest feed rate (EAC 1-1) shows feed marks. Fig 55 shows a detailed 3D result after polynomial fitting. This result clearly shows 25 peaks through the surface.

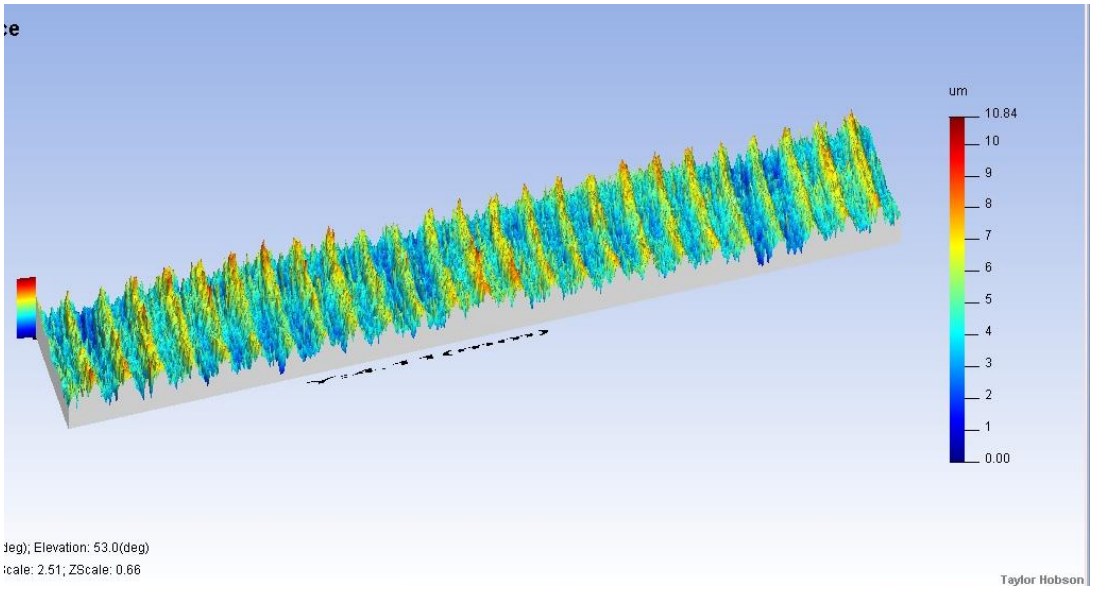

Figure 55. Polynomial fitting of the sample EAC 1-1

Table 3 shows the cutting parameters for the specimen used in the milling process. 6.2 revolutions should cut a 1 mm length. 25.7 revolutions should traverse a 4 mm sample. As the cutter has 3 cutting edges, the surface should show around 77 peaks. Fig 53 shows that only 25 peaks are presented on the surface, which means that the cutter might have one worn cutting edge that made an insufficient cut throughout the surface. Fig 56 shows that the distance between two peaks is 0.169 mm. In section 5.4.2 explained that the distance traversed in one revolution for this sample should be 0.162 mm. Therefore, the difference is 4.1%. This confirms that the distance between these two peaks is one revolution rather than one cut.

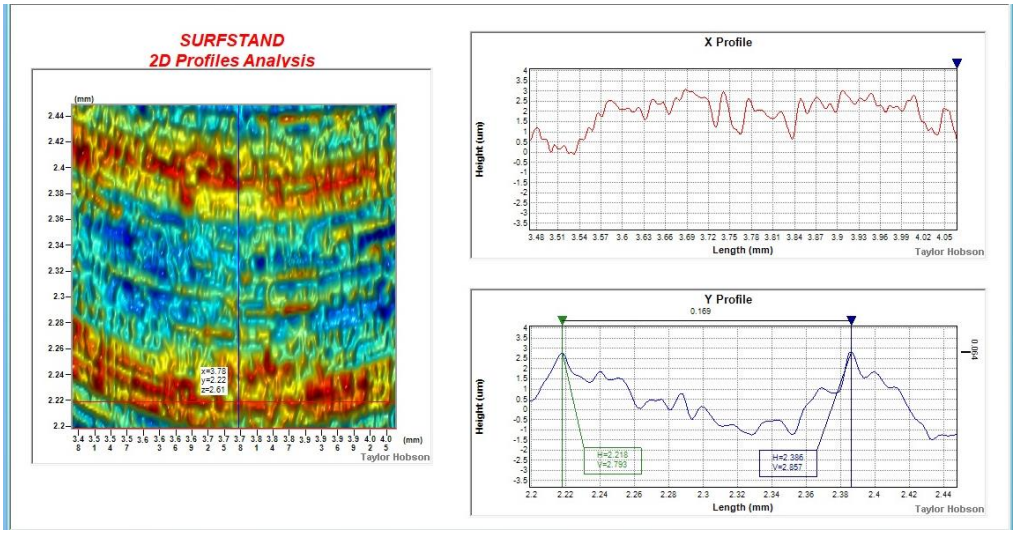

Figure 56. Single feed mark on the Polynomial fitting of the sample EAC 1-1

6.6.2. Analysis of results

Using the cylindrical form removal function in the Alicona to decompose two pick interval cusp marks in each sample, the area roughness parameters in terms of Sa (arithmetical mean height) and Sz (Maximum height) were determined, as shown in Fig 57 and 58. The standard deviation for each sample in Fig 55 was relatively small in the Sa result, being 0.0246 μm for BAC 1-1, 0.063 μm for CAC 1-1 and 0.06 μm for EAC 1-1. However, the standard deviation in the Sz result for BAC 1-1 was 0.286 μm, for CAC 1-1 was 2.76 μm and for EAC 1-1 was 0.203 μm. The CAC 1-1 result is significantly higher than BAC 1-1 and EAC 1-1. Sa and Sz for the actual result and simulation cannot be compared because the simulation does not yet allow the cusp surface to be flattened for direct comparison.

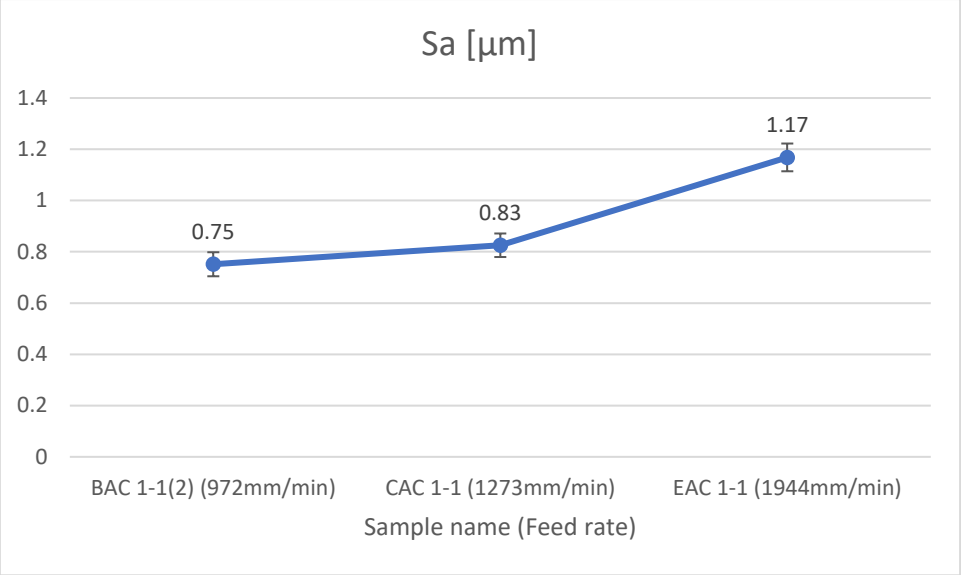

Figure 57. The average Sa value for two cusps on each sample

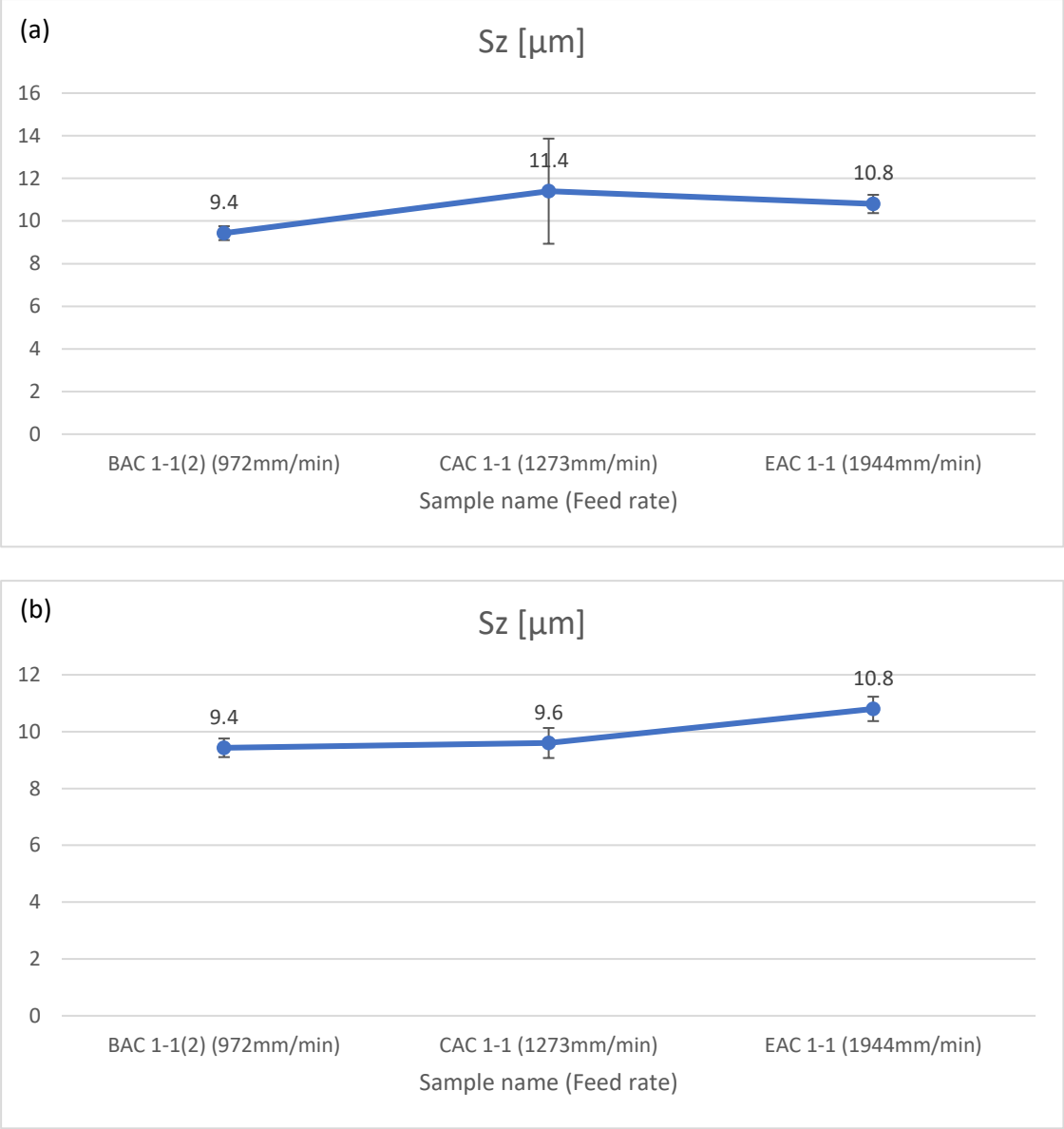

Figure 58. (a)The average Sz value for two cusps on each sample (b) The adjusted average Sz value

These two figures represent the average value of two pick interval cusp marks on all three samples. This step aims to minimise the defects and errors affecting the result. The Sa value gradually increases with the feed rate as shown in Fig 57. This is potentially because the faster feed rate creates vibration of the tool during the cutting process, and the spindle speed was too slow. This leads to the result that the cutter cannot cut effectively and potentially cuts less material than it is designed to cut. The Sz value suddenly increased from the first sample to the second in Fig 58(a). This phenomenon happened

because a defect occurred on the first cusp of the sample which affected the Sz value. It is not good practice to ignore cusps that contain defects since those defects may be caused by the cutting process, rather than being post-cutting artefacts. Another function, called 3D-Editor allows the user to select a defect area or error to remove and fill in the surface according to the surface roughness around that region. However, this function relies greatly on user judgement to define the area as defect or error. After using this function to eliminate the defect, the adjusted Sz value is shown in Fig 58(b). The result shows that there are no significant changes in Sz value. The standard deviation for CAC 1-1 was 0.267 µm, which is more realistic when compared with the other data points. This can be expected because the lead and tilt angle has not changed, and those are the main parameters that affect the height within the feed interval cusp height.

To conclude this section, the Alicona surface inspection machine was used to inspect samples of pick and feed interval cusp marks. Cutting samples have been divided into three scales and the meso- and micro- scales have mainly been used to inspect the feed interval cusp marks. The cylindrical form removal function transformed the pick interval results from a cylindrical form into a flat surface for further investigation of the feed interval cusp marks. Errors appeared on the surface resulting from defects on the surface or from the inspection. The project has only been able to use different feed rate to investigate the simulation result. Therefore, lead and tilt angle investigations are for future research.

6.7. Conclusion

This chapter can be summarised in the following areas.

- A set of cut samples from a previous researcher was inspected using the Alicona Infinite Focus 3D measurement system and the method and the sample surface was divided into three scales for optical inspection.

- The form removal filtration method of the Alicona Infinite Focus 3D measurement system was used to filter the pick interval cusp marks. The result transferred all the feed interval cusp marks and defects but not the pick interval cusp marks.
- The SurfStand inspection software was used to carry out two filtration techniques. Wavelet filtering was carried out and discussed. This filtration method did not remove the pick interval cusp marks satisfactorily. Both sides of the pick interval cusp dominated the sample, leading to errors in the result. Another techniques used was polynomial fitting. The results showed that features on the pick interval cusp can be transformed onto a flat surface.
- Both form removal and polynomial fitting filtration methods have been mathematically validated. The difference between form removal and the theoretical calculation was 4.7%, and the difference between polynomial fitting and the theoretical calculation was 4.1%.
- The Sa result after form removal filtration showed that the overall surface roughness on a single pick interval cusp is proportional to the feed rate. The result for Sz has a similar result but the increase is less than for Sa. Errors on the surface can affect the surface roughness parameters and affected the Sz results in this study. The Sz result was investigated and adjusted to eliminate the error.

7. Conclusion and suggestions for further research

7.1. Conclusion

- A model was developed to simulate the cutting trail of 5-axis milling with adjustable feed rate, spindle speed and different number of cutting edges. The results of the simulation and theoretical calculation were compared. The difference in the feed mark distance was 5.7% because the resolution of the model is not infinite.
- The model was further developed to simulate the cutting trail with lead and tilt angles and a helical cutting edge profile. The simulation clearly demonstrated that the cutting trail leans to the corresponding angle and the helical profile successfully showed at the beginning and end of the each cutting edge.
- A filtration step was developed to filter the cutting trail into a surface to simulate a machined surface to investigate the distance between feed interval marks. The differences in the feed interval mark distance between the simulation model and both Alicona and SurfStand result were less than 1%.
- Another filtration step was developed to filter the surface into a profile to calculate the Ra value. The Alicona Ra result was 5 times greater than that from the model because tool vibration and worn cutting edge occurred during actual cutting.
- An optical 3D measurement system (Alicona Infinite Focus Measurement G4) was used to inspect the specimen surface. An area of approximately 4 mm x 4 mm x 300 µm on each specimen was inspected using a 20x magnification lens.
- Cylindrical form removal, polynomial fitting and wavelet filtering were carried out to investigate feed marks. Cylindrical form removal created the most successful result of these three filtering function, and was used for further investigation as discussed in above.
- Different sample scales within the specimen were investigated. The macro scale view showed the pick interval cusps and the cutting defect. The meso- scale view showed feed

interval marks on the surface. The micro scale view showed tool marks which differ from the feed marks. Tool marks within feed interval marks are not expected in the cutting result. These may result from aluminium oxide generated during the cutting process.

7.1.1. Novelty

The main novelties claimed are:

- A new model was generated to simulate the final surface of 5-axis milling using a ball-end cutter with a helical cutting profile including lead and tilt angles in advance of previous studies.
- The results of the model focus on the feed marks instead of the general surface considered by many previous studies, especially the feed mark chasing effect resulting from a helical cutting edge and fast feed rate, and the distance between each feed interval cusp.

7.2. Further research

7.2.1. Cutting specimen

A range of cutting specimens were made in previous research. However, these specimens resulted from the requirements of the previous research, so the feed rate was relatively slow, and the cutter diameter was relatively small. This created the issue that the feed marks within the cusp were not very clear and the roughness was possibly dominated by tool wear and aluminium oxide created during cutting. Cutting with a faster feed rate and a larger diameter cutter should be arranged for optical inspection to verify more aspects of the cutting model, such as the pattern of any marks within feed mark.

7.2.2. Optical inspection

In this work, the inspection used 20x magnification to inspect all the specimens. However, the result showed that this might not be a high enough magnification to show all the detail required for validation within the cusp and especially within the feed marks. Therefore, a greater level of magnification lens should be used for inspection to acquire more detailed surface results.

7.2.3. Cutting model

The current model can simulate a cutting trail and final surface with various combinations of lead and tilt angle, feed rate, spindle speed, tool diameter, helix angle and time. However, there are no kinetic effects in the model. The model was developed to allow the addition of a variety of kinetic effects such as chipped and worn tool edges, any particles stuck to the tool and tool vibration. This is because the inspection of the specimens was not sufficiently detailed, and the cutting parameters were not ideal to show any relationship between these factors. Therefore, there are no solid results with which to develop the kinetic effects in the model as yet.

For the filtration step, the idea of going through all the points and searching for those within the pre-set grid may not be the most efficient. New code which sets up all the grid at the beginning and picks the points one by one to fit into a relative grid, and then loop to find the lowest point could result a shorter computing time and should be tested.

8. References

Arizmendi, M., Jiménez, A., Cumbicus, W. E., Estrems, M., & Artano, M. (2019). Modelling of elliptical dimples generated by five-axis milling for surface texturing. *International Journal of Machine Tools and Manufacture, 137*, 79-95.

Bandila, A., Khotb, T., Guhaa, A., & Tewaria, A. (2017). Cutting Force Modeling of Multi-axis Milling Processes for Variable Tool Workpiece Encounter Geometries.

Baptista, R., & Simoes, J. A. (2000). Three and five axes milling of sculptured surfaces. *Journal of Materials Processing Technology, 103*(3), 398-403.

Barrans, Tabriz, & Ellis. (2017). DETERMINING STRESS IN TURBOCHARGER IMPELLERS DUE TO COMPONENT MACHINING PROCESS. *SAE International Journal of Materials and Manufacturing*, 11.

Barrans, S., Tabriz, M. S. E., & Ellis, C. (2017). Determining stress in turbocharger impellers due to component machining. *ASME Turbo Expo: Turbomachinery Technical Conference & Exposition 2017*.

Bhardwaj, B., Kumar, R., & Singh, P. K. (2014). Surface roughness (Ra) prediction model for turning of AISI 1019 steel using response surface methodology and Box–Cox transformation. *Proceedings of the Institution of Mechanical Engineers, Part B: Journal of Engineering Manufacture, 228*(2), 223-232.

Biermann, D., Kersting, P., & Surmann, T. (2010). A general approach to simulating workpiece vibrations during five-axis milling of turbine blades. *CIRP annals, 59*(1), 125-128.

Blunt, L., & Jiang, X. (2003a). *Advanced techniques for assessment surface topography: development of a basis for 3D surface texture standards" surfstand"*. Elsevier.

Blunt, L., & Jiang, X. (2003b). *Advanced techniques for assessment surface topography: development of a basis for 3D surface texture standards" surfstand"*. Elsevier.

Bo, L., Yanlong, C., Wenhua, C., & Jun, P. (2017). Geometry simulation and evaluation of the surface topography in five-axis ball-end milling. *The International Journal of Advanced Manufacturing Technology, 93*(5), 1651-1667.

Buj-Corral, I., Vivancos-Calvet, J., & Domínguez-Fernández, A. (2012). Surface topography in ball-end milling processes as a function of feed per tooth and radial depth of cut. *International Journal of Machine Tools & Manufacture, 53*(1), 151-159.

Cagan, S. C., Venkatesh, B., & Buldum, B. B. (2020). Investigation of surface roughness and chip morphology of aluminum alloy in dry and minimum quantity lubrication machining. *Materials Today: Proceedings, 27*, 1122-1126.

Cai, Y., Chang, W., Luo, X., Sousa, A. M., Lau, K. H. A., & Qin, Y. (2018). Superhydrophobic structures on 316L stainless steel surfaces machined by nanosecond pulsed laser. *Precision Engineering, 52*, 266-275.

Chan, C., & Barrans, S. (2021). Simulating 5-Axis Milling with a Ball Nose Cutting Tool. 2021 12th International Conference on Mechanical and Aerospace Engineering (ICMAE),

Chan, C., & Walton, K. (2021). Areal Decomposition Methodology for a 5-Axis Milled Surface. Advances in Manufacturing Engineering and Materials II: Proceedings of the International Conference on Manufacturing Engineering and Materials (ICMEM 2020), 21–25 June, 2021, Nový Smokovec, Slovakia,

Chen, Huang, & Chen. (2005). A study of the surface scallop generating mechanism in the ball-end milling process. *International Journal of Machine Tools & Manufacture 45*, 8.

Chen, J.-S., Huang, Y.-K., & Chen, M.-S. (2005). A study of the surface scallop generating mechanism in the ball-end milling process. *International Journal of Machine Tools & Manufacture, 45*(9), 1077-1084.

Chen, Q., Yang, S., & Li, Z. (1999). Surface roughness evaluation by using wavelets analysis. *Precision Engineering, 23*(3), 209-212.

Chen, X., Zhao, J., & Zhang, W. (2019). Optimization analysis considering the cutting effects for high-speed five-axis down milling process by employing ball end mill. *The International Journal of Advanced Manufacturing Technology, 105*(12), 4989-5008.

Dai, Y., Li, H., Dong, J., Zhou, Q., Yong, J., & Liu, S. (2019). An updated model of stability prediction in five-axis ball-end milling. *The International Journal of Advanced Manufacturing Technology, 103*(9), 3293-3306.

Denkena, Böß, Nespor, Gilge, Hohenstein, & Seume. (2015). Prediction of the 3D Surface Topography after Ball End Milling and its Influence on Aerodynamics. *Procedia CIRP 31*, 7.

Denkena, B., Krödel, A., Muecke, A., & Ellersiek, L. (2021). Prediction of plastic surface defects for 5-axis ball end milling of Ti-6Al-4 V with rounded cutting edges using a material removal simulation. *CIRP annals, 70*(1), 91-94.

Devi, R. R., & Pugazhenthi, D. (2016). Ideal sampling rate to reduce distortion in audio steganography. *Procedia Computer Science, 85*, 418-424.

Duval-Chaneac, M., Han, S., Claudin, C., Salvatore, F., Bajolet, J., & Rech, J. (2018a). Characterization of maraging steel 300 internal surface created by selective laser melting (SLM) after abrasive flow machining (AFM). *Procedia CIRP, 77*, 359-362.

Duval-Chaneac, M., Han, S., Claudin, C., Salvatore, F., Bajolet, J., & Rech, J. (2018b). Experimental study on finishing of internal laser melting (SLM) surface with abrasive flow machining (AFM). *Precision Engineering, 54*, 1-6.

Fan, J., & Gijbels, I. (1995). Data-driven bandwidth selection in local polynomial fitting: variable bandwidth and spatial adaptation. *Journal of the Royal Statistical Society: Series B (Methodological), 57*(2), 371-394.

Feng, H.-Y., & Su, N. (2000). Integrated tool path and feed rate optimization for the finishing machining of 3D plane surfaces. *International Journal of Machine Tools and Manufacture, 40*(11), 1557-1572.

Ficker, T., & Martišek, D. (2015). 3D image reconstructions and the Nyquist–Shannon theorem. *3D Research, 6*(3), 1-18.

Gdula, M. (2020). Empirical models for surface roughness and topography in 5-axis milling based on analysis of lead angle and curvature radius of sculptured surfaces. *Metals, 10*(7), 932.

Gdula, M., Burek, J., Zylka, L., & Plodzien, M. (2018). Five-axis milling of sculptured surfaces of the turbine blade. *Aircraft Engineering and Aerospace Technology, 90*(1), 146-157.

Ghorbani, M., & Movahhedy, M. R. (2019). An analytical model for cutter-workpiece engagement calculation in ball-end finish milling of doubly curved surfaces. *The International Journal of Advanced Manufacturing Technology, 102*(5), 1635-1657.

Gómez-Escudero, G., Jimeno Beitia, A., Martínez de Pissón Caruncho, G., López de Lacalle, L. N., González-Barrio, H., Pereira Neto, O., & Calleja-Ochoa, A. (2021). A reliable clean process for five-axis milling of knee prostheses. *The International Journal of Advanced Manufacturing Technology, 115*(5), 1605-1620.

Gray, P. J., Ismail, F., & Bedi, S. (2003). Cusp modeling for 5-axis surface machining. Proceedings of the eighth ACM symposium on Solid modeling and applications,

Habibi, M., Kilic, Z. M., & Altintas, Y. (2021). Minimizing flute engagement to adjust tool orientation for reducing surface errors in five-axis ball end milling operations. *Journal of Manufacturing Science and Engineering, 143*(2).

Haddag, B., Atlati, S., Nouari, M., & Moufki, A. (2016). Dry machining aeronautical aluminum alloy AA2024-T351: Analysis of cutting forces, chip segmentation and built-up edge formation. *Metals, 6*(9), 197.

Han, S. G., & Zhao, J. (2010). Effect of tool inclination angle on surface quality in 5-axis ball-end milling. Advanced Materials Research,

Han, S. G., Zhao, J., & Zhang, X. F. (2009). Surface topography and roughness simulations for 5-axis ball-end milling. Advanced Materials Research,

Hauth, S., Richterich, C., Glasmacher, L., & Linsen, L. (2011). Constant cusp toolpath generation in configuration space based on offset curves. *The International Journal of Advanced Manufacturing Technology, 53*(1-4), 325-338.

Huang, W., Li, X., Zhang, Y., Liang, G., & Gao, W. (2018). Prediction of ball end milling forces based on special turning experiment data. *The International Journal of Advanced Manufacturing Technology, 96*(9), 4423-4430.

Huang, W., Zhao, J., Niu, J., Wang, G., & Cheng, R. (2018). Comparison in surface integrity and fatigue performance for hardened steel ball-end milled with different milling speeds. *Procedia CIRP, 71*, 267-271.

Huang, W., Zhao, J., Xing, A., Wang, G., & Tao, H. (2018). Influence of tool path strategies on fatigue performance of high-speed ball-end-milled AISI H13 steel. *The International Journal of Advanced Manufacturing Technology, 94*(1), 371-380.

[Record #55 is using a reference type undefined in this output style.]

Ju, G., Song, Q., Liu, Z., Shi, J., & Wan, Y. (2015). A solid-analytical-based method for extracting cutter-workpiece engagement in sculptured surface milling. *The International Journal of Advanced Manufacturing Technology, 80*, 1297-1310.

Jung, Y., Lee, D., Kim, J., & Mok, H. (2002). NC post-processor for 5-axis milling machine of table-rotating/tilting type. *Journal of Materials Processing Technology, 130*, 641-646.

Keren, D., & Gotsman, C. (1999). Fitting curves and surfaces with constrained implicit polynomials. *IEEE Transactions on Pattern Analysis and Machine Intelligence, 21*(1), 31-41.

KEYENCE. (2024a). *Sk(Core height) | Area Roughness Parameters*. https://www.keyence.com/ss/products/microscope/roughness/surface/sk-core-roughness-depth.jsp

KEYENCE. (2024b). *Svk (Reduced Dale Height, Reduced Valley Depth) | Area Roughness Parameters*. https://www.keyence.com/ss/products/microscope/roughness/surface/svk-reduced-dale-height.jsp

Khare, S. K., & Agarwal, S. (2015). Predictive modeling of surface roughness in grinding. *Procedia CIRP, 31*, 375-380.

Khorasani, A. M., Gibson, I., Goldberg, M., & Littlefair, G. (2018). A comprehensive study on surface quality in 5-axis milling of SLM Ti-6Al-4V spherical components. *The International Journal of Advanced Manufacturing Technology, 94*(9), 3765-3784.

Kittali, P., Kalwa, V., Athith, D., Prashanth, K., & Venkatesh, B. (2022). Optimization of machining parameters in turning operation to minimize the surface roughness using Taguchi technique for EN1A alloy steel. *Materials Today: Proceedings, 54*, 463-467.

Lavernhe, S., Quinsat, Y., & Lartigue, C. (2010). Model for the prediction of 3D surface topography in 5-axis milling. *The International Journal of Advanced Manufacturing Technology, 51*(9), 915-924.

Layegh, & Lazoglu. (2017). 3D surface topography analysis in 5-axis ball-end milling. *CIRP Annals - Manufacturing Technology*, 4.

Leach, R. (2013). *Characterisation of areal surface texture*. Springer.

Lévesque, L. (2014). Nyquist sampling theorem: understanding the illusion of a spinning wheel captured with a video camera. *Physics Education, 49*(6), 697.

Li, H. S., Romeijn, H. E., & Dempsey, J. F. (2006). A Fourier analysis on the maximum acceptable grid size for discrete proton beam dose calculation. *Medical physics, 33*(9), 3508-3518.

Li, Z.-L., Wang, X.-Z., & Zhu, L.-M. (2016). Arc–surface intersection method to calculate cutter–workpiece engagements for generic cutter in five-axis milling. *Computer-Aided Design, 73*, 1-10.

Lizzul, L., Sorgato, M., Bertolini, R., Ghiotti, A., & Bruschi, S. (2021). Ball end milling machinability of additively and conventionally manufactured Ti6Al4V tilted surfaces. *Journal of Manufacturing Processes, 72*, 350-360.

Ma, J.-w., Jia, Z.-y., Wang, F.-j., & Ning, F.-d. (2014). Spindle speed selection for high-speed milling of titanium alloy curved surface. *Materials and Manufacturing Processes, 29*(3), 364-369.

Mersni, Boujelbene, Salem, & Alghamdi. (2018). Optimization of the surface roughness in ball end milling of titanium alloy Ti-6A1-4V using the Taguchi Method. *Procedia Manufacturing 20*, 7.

Muralikrishnan, B., & Raja, J. (2009). A Brief History of Filtering. *Computational Surface and Roundness Metrology*, 7-11.

Nakatani, M., Masuo, H., Tanaka, Y., & Murakami, Y. (2019). Effect of surface roughness on fatigue strength of Ti-6Al-4V alloy manufactured by additive manufacturing. *Procedia Structural Integrity, 19*, 294-301.

Nespor, D., Denkena, B., Grove, T., & Pape, O. (2016). Surface topography after re-contouring of welded Ti-6Al-4V parts by means of 5-axis ball nose end milling. *The International Journal of Advanced Manufacturing Technology, 85*(5), 1585-1602.

Nwaogu, U. C., Tiedje, N. S., & Hansen, H. N. (2013). A non-contact 3D method to characterize the surface roughness of castings. *Journal of Materials Processing Technology, 213*(1), 59-68.

Ozturk, Tunc, & Budak. (2009). Investigation of lead and tilt angle effects in 5-axis ball-end milling processes. *International Journal of Machine Tools & Manufacture*, 10.

Ozturk, E., & Budak, E. (2007). Modeling of 5-axis milling processes. *Machining science and technology, 11*(3), 287-311.

Ozturk, E., Tunc, L. T., & Budak, E. (2009). Investigation of lead and tilt angle effects in 5-axis ball-end milling processes. *International Journal of Machine Tools & Manufacture, 49*(14), 1053-1062.

Park, S., Jun, Y.-T., Lee, C.-W., & Yang, M.-Y. (1993). Determining the cutting conditions for sculptured surface machining. *The International Journal of Advanced Manufacturing Technology, 8*(2), 61-70.

Pham, T.-H., Nguyen, D.-T., Banh, T.-L., & Tong, V.-C. (2020). Experimental study on the chip morphology, tool–chip contact length, workpiece vibration, and surface roughness during high-speed face milling of A6061 aluminum alloy. *Proceedings of the Institution of Mechanical Engineers, Part B: Journal of Engineering Manufacture, 234*(3), 610-620.

Podulka. (2018). The Effect of Valley Location in Two-Process Surface Topography Analysis. *Advances in Science and Technology Research Journal, 12*(4), 6.

Polishetty, A., Alabdullah, M., & Littlefair, G. (2017). Tool wear analysis due to machining in super austenitic stainless steel. MATEC Web of Conferences,

Por, E., van Kooten, M., & Sarkovic, V. (2019). Nyquist–Shannon sampling theorem. *Leiden University, 1*, 1.

Prat, D., Fromentin, G., Poulachon, G., & Duc, E. (2012). Experimental Analysis and Geometrical Modeling of Cutting Conditions Effect in 5 Axis Milling With Ti6Al4 V Alloy. *Procedia CIRP, 1*, 84-89.

Quinsat, Y., Lavernhe, S., & Lartigue, C. (2011). Characterization of 3D surface topography in 5-axis milling. *Wear, 271*(3-4), 590-595.

Romo-Cárdenas, G., Avilés-Rodríguez, G., Sánchez-López, J. d. D., Cosío-León, M., Luque, P., Gómez-Gutiérrez, C., Nieto-Hipólito, J. I., Vázquez-Briseño, M., & Navarro-Cota, C. X. (2018). Nyquist-Shannon theorem application for Savitzky-Golay smoothing window size parameter determination in bio-optical signals. *Results in Physics, 11*, 17-22.

Ryabov, E., Khisamutdinov, R., Grechishnikov, V., Yurasov, S. Y., & Yurasova, O. (2018). Ball end mill with curved cutting edge and constant cutting geometry. *Russian Engineering Research, 38*(12), 1015-1017.

Seid Ahmed, Y., Paiva, J. M., Covelli, D., & Veldhuis, S. C. (2017). Investigation of coated cutting tool performance during machining of super duplex stainless steels through 3D wear evaluations. *Coatings, 7*(8), 127.

Shan, C., Lv, X., & Duan, W. (2016). Effect of tool inclination angle on the elastic deformation of thin-walled parts in multi-axis ball-end milling. *Procedia CIRP, 56*, 311-315.

Shannon, C. E. (1948). A mathematical theory of communication. *The Bell system technical journal, 27*(3), 379-423.

Sharma, P., Sharma, S., & Khanduja, D. (2015). A study on microstructure of aluminium matrix composites. *Journal of Asian Ceramic Societies, 3*(3), 240-244.

Shaw, D., & Ou, G.-Y. (2008). Reducing X, Y and Z axes movement of a 5-axis AC type milling machine by changing the location of the work-piece. *Computer-Aided Design, 40*(10-11), 1033-1039.

Sheen, B.-T., & You, C.-F. (2006). Machining feature recognition and tool-path generation for 3-axis CNC milling. *Computer-Aided Design, 38*(6), 553-562.

Song, Liu, Ju, & Wan. (2017). A generalized cutting force model for five-axis milling processes. *Journal of Engineering Manufacture, 233(1)*, 15.

Sreejith, P. (2008). Machining of 6061 aluminium alloy with MQL, dry and flooded lubricant conditions. *Materials letters, 62*(2), 276-278.

Ståhl, J.-E., Schultheiss, F., & Hägglund, S. (2011). Analytical and experimental determination of the Ra surface roughness during turning. *Procedia Engineering, 19*, 349-356.

Sun, & Guo. (2011). Numerical simulationandpredictionofcuttingforcesinfive-axismilling processes withcutterrun-out. *International Journal of Machine Tools and Manufacture, 51*(10-11), 10.

Tabriz, M. S. E., Barrans, S. M., & Bills, P. J. (2017). Effect of machining parameters on surface roughness in Al 2618 alloy subject to multi-axis machining process using ball nose cutting tools. 2017 8th International Conference on Mechanical and Aerospace Engineering (ICMAE),

Tan, L., Yao, C., Zhang, D., Ren, J., Zhou, Z., & Zhang, J. (2020). Evolution of surface integrity and fatigue properties after milling, polishing, and shot peening of TC17 alloy blades. *International Journal of Fatigue, 136*, 105630.

Thakur, A., & Gangopadhyay, S. (2016). State-of-the-art in surface integrity in machining of nickel-based super alloys. *International Journal of Machine Tools & Manufacture, 100*, 25-54.

Tunc, L. T. (2019). Smart tool path generation for 5-axis ball-end milling of sculptured surfaces using process models. *Robotics and Computer-Integrated Manufacturing, 56*, 212-221.

Tunc, L. T., & Budak, E. (2009). Extraction of 5-axis milling conditions from CAM data for process simulation. *The International Journal of Advanced Manufacturing Technology, 43*(5), 538-550.

Vakondios, Kyratsis, Yaldiz, & Antoniadis. (2015). Influence of milling strategy on the surface roughness in ball end milling of the aluminum alloy Al7075-T6. *Measurement*, 9.

Walton, Blunt, & Fleming. (2015, 10 August 2015). The topographic development and areal parametric characterization of a stratified surface polished by mass finishing. *Surface Topography: Metrology and Properties, 3*, 11.

Wang, Zhang, & Yan. (2017, March 2017). Study on surface defects in five-axis ball-end milling of tool steel. *The International Journal of Advanced Manufacturing Technology, 89*(1-4), 11.

Wang, P., Sin, W. J., Nai, M. L. S., & Wei, J. (2017). Effects of processing parameters on surface roughness of additive manufactured Ti-6Al-4V via electron beam melting. *Materials, 10*(10), 1121.

Wang, P., Zhang, S., Li, Z., & Li, J. (2016). Tool path planning and milling surface simulation for vehicle rear bumper mold. *Advances in Mechanical Engineering, 8*(3), 1687814016641569.

Wang, S., Geng, L., Zhang, Y., Liu, K., & Ng, T. (2015). Cutting force prediction for five-axis ball-end milling considering cutter vibrations and run-out. *International Journal of Mechanical Sciences, 96*, 206-215.

Wang, Y., Xu, J., & Sun, Y. (2021). Tool orientation adjustment for improving the kinematics performance of 5-axis ball-end machining via CPM method. *Robotics and Computer-Integrated Manufacturing, 68*, 102070.

Wang, Z., Wang, B., & Yuan, J. (2019). Modeling of surface topography based on cutting vibration in ball-end milling of thin-walled parts. *The International Journal of Advanced Manufacturing Technology, 101*(5), 1837-1854.

Whitehouse, D. J. (2010). *Handbook of surface and nanometrology*. CRC press.

Wojciechowski, Twardowski, Pelic, Maruda, Barrans, & Krolczyk. (2016). Precision surface characterization for finish cylindrical milling with dynamic tool displacements model. *Precision Engineering, 46*, 8.

Wojciechowski, S., Maruda, R., Barrans, S., Nieslony, P., & Krolczyk, G. (2017). Optimisation of machining parameters during ball end milling of hardened steel with various surface inclinations. *Measurement, 111*, 18-28.

Xu, J., Xu, L., Geng, Z., Sun, Y., & Tang, K. (2020). 3D surface topography simulation and experiments for ball-end NC milling considering dynamic feedrate. *CIRP Journal of Manufacturing Science and Technology, 31*, 210-223.

Yang, Yao, Xie, Zhang, & Dou. (2016). Effect of Tool Orientation on Surface Integrity during Ball End Milling of Titanium Alloy TC17. *Procedia CIRP 56*, 6.

Yang, P., Yao, C., Xie, S., Zhang, D., & Tang, D. X. (2016). Effect of tool orientation on surface integrity during ball end milling of titanium alloy TC17. *Procedia CIRP 31, 56*, 143-148.

Yigit, I. E., & Lazoglu, I. (2015). Analysis of tool orientation for 5-axis ball-end milling of flexible parts. *CIRP annals, 64*(1), 97-100.

Yu, Y., Lin, C., & Hu, Y. (2021). Study on simulation and experiment of non-circular gear surface topography in ball end milling. *The International Journal of Advanced Manufacturing Technology, 114*(7), 1913-1923.

Zamaruiev, V. (2017). The use of Kotelnikov-Nyquist-Shannon sampling theorem for designing of digital control system for a power converter. 2017 IEEE First Ukraine Conference on Electrical and Computer Engineering (UKRCON),

Zhang, X., Zhang, J., Zheng, X., Pang, B., & Zhao, W. (2017). Tool orientation optimization of 5-axis ball-end milling based on an accurate cutter/workpiece engagement model. *CIRP Journal of Manufacturing Science and Technology, 19*, 106-116.

Zhao, Y., & Suhr, H. (1992). Aluminium oxide thin films prepared by plasma-enhanced chemical vapour deposition. *Applied Physics A, 55*(2), 176-179.

9. Appendix

9.1. Appendix A – 3-axis cutting trail

```
clear
fx = 0.007; % feedrate in m/s
omega = 2*pi; % spindle speed in rad/s
radius = 0.005; % tool diameter in m
count = 0; % count number for later for loop
for t = 0:800 % time unit
time = t/400; % resolution for each time unit
for angle = 0:200 % resolution for each cutting edge
theta = (pi/2)*angle/200; % the theta point
      count = count + 2;
      uvw_vector=[(-radius*cos(theta)*cos(omega*time));
   (radius*cos(theta)*sin(omega*time)); (radius-radius*sin(theta))]; %
   uvw vector of first cutting edge
      xyz_vector=uvw_vector;
      uvw_vector2=[(-radius*cos(theta)*cos(omega*time+pi));
   (radius*cos(theta)*sin(omega*time+pi)); (radius-radius*sin(theta))];
   % uvw vector of second cutting edge
      xyz_vector2=uvw_vector2;
      xyzPoints(count,1) = xyz_vector(1)+fx*time; % calculate the
   point of interest in x direction
      xyzPoints(count,2) = xyz_vector(2); % calculate the point of
   interest in y direction
      xyzPoints(count,3) = xyz_vector(3); % calculate the point of
   interest in z direction
      xyzPoints(count+1,1) = xyz_vector2(1)+fx*time; % calculate the
   point of interest in x direction
      xyzPoints(count+1,2) = xyz_vector2(2); % calculate the point of
   interest in y direction
      xyzPoints(count+1,3) = xyz_vector2(3); % calculate the point of
   interest in z direction
      end
      end
      figure (1)
      ptCloud = pointCloud(xyzPoints)
      pcshow(xyzPoints,'MarkerSize',20)
```

9.2. Appendix B – 5-axis cutting trail

```
clear
fx = 0.007; % feedrate in m/s
omega = 2*pi; % spindle speed in rad/s
radius = 0.005; % tool diameter in m
phi = (pi*(30)/180); % Lead angle
xi = (pi*(0)/180); % Tilt angle
```

```
7) Tmatrix=[cos(phi) 0 sin(phi);sin(xi)*sin(phi) cos(xi) -
   sin(xi)*cos(phi);cos(xi)*-sin(phi) sin(xi) cos(xi)*cos(phi)% Lead and
   tilt angle matrix
8) count = 0;
9) for t = 0:800
10)      time = t/400;
11)      for angle = 0:200
12)      theta = (pi/2)*angle/200;
13)      count = count + 2;
14)      uvw_vector = [(-radius*cos(theta)*cos(omega*time));
   (radius*cos(theta)*sin(omega*time)); (radius-radius*sin(theta))]; %
   uvw vector of first cutting edge
15)      fcn_vector = Tmatrix*uvw_vector;
16)      uvw_vector2 = [(-radius*cos(theta)*cos(omega*time+pi));
   (radius*cos(theta)*sin(omega*time+pi)); (radius-radius*sin(theta))];
   % uvw vector of second cutting edge
17)      fcn_vector2 = Tmatrix*uvw_vector2;
18)      xyzPoints(count,1) = fcn_vector(1)+fx*time; % calculate the
   point of interest in x direction
19)      xyzPoints(count,2) = fcn_vector(2); % calculate the point of
   interest in y direction
20)      xyzPoints(count,3) = fcn_vector(3); % calculate the point of
   interest in z direction
21)      xyzPoints(count+1,1) = fcn_vector2(1)+fx*time; % calculate the
   point of interest in x direction
22)      xyzPoints(count+1,2) = fcn_vector2(2); % calculate the point of
   interest in y direction
23)      xyzPoints(count+1,3) = fcn_vector2(3); % calculate the point of
   interest in z direction
24)      end
25)      end
26)      figure (1)
27)      ptCloud = pointCloud(xyzPoints)
28)      pcshow(xyzPoints,'MarkerSize',20)
```

9.3. Appendix C – 5-axis cutting trail with helical cutting edge profile

```
1) clear
2) fx = 0.324; % feedrate in m/s
3) rev = 12000; % spindle speed in rev/min
4) revper1 = 1/((rev)/60); % time for each revolution
5) omega = -(rev)/9.5493; % spindle speed in rad/s
6) radius = 0.001; % tool radius in m
7) phi = (pi*(-55)/180); % Lead angle
8) xi = (pi*(0)/180); % Tilt angle
9) helix = ((pi)*(30)/180); % Helix angle
10)      NC = 3; % No. of the cutting edge
11)      Tmatrix=[ cos(phi) 0 sin(phi);sin(xi)*sin(phi) cos(xi) -
   sin(xi)*cos(phi);cos(xi)*-sin(phi) sin(xi) cos(xi)*cos(phi)]% Lead
   and tilt angle matrix
12)      realtime = ((revper1)*(2)); % actual cutting time in sec and
   set the number of revolution
```

```
13)      TU = (revper1)*100000; % number of increment per rev, Original
   3000000
14)      timeunit = (TU)*((rev)/60); % number of increment in 1 sec
15)      thetaincrement = 0.5; % theta increment
16)      CropHeight = -0.00035; % Cusp height
17)      totalcount =
   (timeunit)*(realtime)*((90+1)/(thetaincrement))*NC; % total number of
   points
18)      count = 0 ;% Set the count no. from 0
19)      xyzPoints = zeros(totalcount,3);
20)      totaltooltraveldistance = (fx)*(realtime);

21)      for t = 0:((timeunit)*(realtime)); % No. of section for total
   time
22)      time = t/(timeunit); % Time unit
23)      for theta = 0:thetaincrement:90;
24)      wi = radius*((1-(sind(theta)))); % non-linear spacing for the
   zi value;
25)      ri = (sqrt((2*radius*wi)-(wi^2))); % Correlated distance
   between the pre-set point and the tool axis
26)      beta = (wi/radius)*tan(helix); % Angle bewteen the pre-set
   point and the x axis
27)      uvw_vector=[-ri*cos(beta+omega*time);-
   ri*sin(beta+omega*time);(wi)] % TCS matrix
28)      xyz_vector=Tmatrix*uvw_vector; % Combine lead and tilt angle
   matrix and TCS matrix
29)      uvw_vector2=[-ri*cos(beta+(omega*time+(2*pi/3)));-
   ri*sin(beta+(omega*time+(2*pi/3)));(wi)] % TCS matrix
30)      xyz_vector2=Tmatrix*uvw_vector2; % Combine lead and tilt angle
   matrix and TCS matrix
31)      uvw_vector3=[-ri*cos(beta+(omega*time+(4*pi/3)));-
   ri*sin(beta+(omega*time+(4*pi/3)));(wi)] % TCS matrix
32)      xyz_vector3=Tmatrix*uvw_vector3; % Combine lead and tilt angle
   matrix and TCS matrix

33)      count = count + NC; % Start the count no. from 0 + 3
34)      xyzPoints(count,1) = xyz_vector(1)+fx*time; % calculate the
   point of interest in x direction
35)      xyzPoints(count,2) = xyz_vector(2); % calculate the point of
   interest in y direction
36)      xyzPoints(count,3) = xyz_vector(3); % calculate the point of
   interest in z direction
37)      if xyzPoints(count,3) < CropHeight
38)      xyzPoints(count,3) = xyz_vector(3);
39)      else count = count - 1;
40)      end
41)      xyzPoints(count+1,1) = xyz_vector2(1)+fx*time; % calculate the
   point of interest in x direction
42)      xyzPoints(count+1,2) = xyz_vector2(2); % calculate the point of
   interest in y direction
43)      xyzPoints(count+1,3) = xyz_vector2(3); % calculate the point of
   interest in z direction
44)      if xyzPoints(count+1,3) < CropHeight % filter the point of
   interest higher than preset cusp height
45)      xyzPoints(count+1,3) = xyz_vector2(3);
46)      else count = count - 1;
```

```
47)      end
48)      xyzPoints(count+2,1) = xyz_vector3(1)+fx*time; % calculate the
   point of interest in x direction
49)      xyzPoints(count+2,2) = xyz_vector3(2); % calculate the point of
   interest in y direction
50)      xyzPoints(count+2,3) = xyz_vector3(3); % calculate the point of
   interest in z direction
51)      if xyzPoints(count+2,3) < CropHeight % filter the point of
   interest higher than preset cusp height
52)      xyzPoints(count+2,3) = xyz_vector3(3);
53)      else count = count - 1;
54)      end
55)      end
56)      end
57)      figure (61) % Name of the following pcshow
58)      ptCloud = pointCloud(xyzPoints) % Illustration of the cutter
   movement, the size of each point
59)      pcshow(ptCloud,'MarkerSize',20)
60)      unit_vector=Tmatrix*[0;0;1] % Show the unit vector of the
   cutting tool
61)      save('testing3surface1test1Feed1620R1SS399fx0027Lead55Tilt20Hel
   ix_30RT1.500TU500000.mat','ptCloud')
```

9.4. Appendix D – Filtering the cutting trail into a surface

```
1) clear
2) load('PaperResultWith3CutterCropTop0003EAC1CropTop015.mat')
3) xyzPoints = ptCloud.Location;
4) figure (66) % Name of the following pcshow
5) ptCloud = pointCloud(xyzPoints)
6) pcshow(ptCloud,'MarkerSize',20)
7) icount = size(xyzPoints,1); % Set the count no. from 0
8) FilteringZheight = 0; % The Z height for filtering
9) TotalLengthinx = fx*time; % Total length in x direction
10)      TotalFilterLength = fx*realtime+((sqrt((radius^2)-
   (FilteringZheight^2)))*2); % Total lenght of the filtered result
11)      eachincrementtraveldistance =
   (1/(timeunit))*(abs(omega))*(radius); % Distance travelled by outer
   edge of tool in 1 time increment
12)      samplecloudresolution = eachincrementtraveldistance*3; %
   Avoiding Aliasing
13)      min_values = min(xyzPoints); % Minimum value of xyzPoints
14)      xmin = -0.0008; % Set the xmin as the 1st row of minimum value
   in xyzPoints
15)      ymin = min_values(2); % Set the ymin as the 2nd row of minimum
   value in xyzPoints
16)      max_values = max(xyzPoints); % Maximum value of xyzPoints
17)      xmax = -0.00055; % Set the xmax as the 1st row of maximum value
   in xyzPoints
18)      ymax = max_values(2); % Set the ymax as the 2nd row of maximum
   value in xyzPoints
```

```
19)      xrange = xmax - xmin; % Set the x range within the xmax and
   xmin
20)      yrange = ymax - ymin; % Set the y range within the ymax and
   ymin
21)      numberpointsx = 200;
22)      numberpointsy = 137;
23)      xincrement = xrange/numberpointsx; % Set the x increment using
   xrange divided by xresolution
24)      yincrement = yrange/numberpointsy; % Set the y increment using
   yrange divided by yresolution
25)      totalcountdisplay = numberpointsx*numberpointsy;
26)      xyzdisplay = zeros(totalcountdisplay,3);
27)      kcount = 0; % 3rd set of count and named as kcount in 0
28)      for xsteps = 0:numberpointsx; % No. of section for xsteps
   according to x axis resolution
29)          xvalue = xmin + xincrement*(xsteps + 0.5); % Set xvalue
   equal xmin plus xincrement times xsteps plus 0.5 which is the middle
   of each step
30)           grid_xmin = xmin + xincrement*xsteps ; % Set the grid_xmin
   as xmin plus xincrement times xsteps
31)           grid_xmax = grid_xmin + xincrement; % Set the grid_xmax as
   grid_xmin plus xincrement
32)          for ysteps = 0:numberpointsy; % No. of section for ysteps
   according to y axis resolution
33)              kcount = kcount + 1; % Start the kcount no. from 0 + 1
34)              xyzdisplay(kcount,1) = xvalue; % Set 1st row of
   xyzdisplay equal to xvalue
35)              yvalue = ymin + yincrement*(ysteps + 0.5); % Set yvalue
   equal ymin plus yincrement times ysteps plus 0.5 which is the middle
   of each step
36)              xyzdisplay(kcount,2) = yvalue;% Set 2nd row of
   xyzdisplay equal to yvalue
37)              xyzdisplay(kcount,3) = 0.0004;% Set 3rd row of
   xyzdisplay equal to 0.0005 to limit the height
38)              point2_zvalue = NaN; % Establish a point2_zvalue for
   further use
39)              grid_ymin = yvalue - yincrement/2; % Set the grid_ymin
   as yvalue minus yincrement divided by 2
40)              grid_ymax = yvalue + yincrement/2; % Set the grid_ymax
   as yvalue plus yincrement divided by 2
41)              count = icount;
42)              for jcount = 1:count;  % 4th set of count and named as
   jcount from 1 to the No_points
43)                  if (grid_xmin <= xyzPoints(jcount,1)) &&
   (xyzPoints(jcount,1) < grid_xmax) && (grid_ymin <=
   xyzPoints(jcount,2)) && (xyzPoints(jcount,2) < grid_ymax); % The
   preset grid
44)                      point_zvalue = xyzPoints(jcount,3); % Find
   out the z value of each point within each preset grid
45)                      if point_zvalue < xyzdisplay(kcount,3);
46)                         xyzdisplay(kcount,3) = point_zvalue; %
   Find out the maximum z value in each preset grid
47)                         point2_zvalue = point_zvalue; % Set the
   maximum value in point2_zvalue for further use
48)                      end
49)                  end
```

```
50)             end
51)         if point2_zvalue < FilteringZheight; % Find out if
   point2_zvalue is greater than 0.0002
52)             xyzdisplay(kcount,3) = point2_zvalue; % If so
   point2_zvalue will be set as 3rd row of xyzdisplay as the greatest z
   value within each grid
53)         else
54)             kcount = kcount - 1;% Else than back to another point
   to find out the greatest within the grid
55)         end
56)         surfacegrid(xsteps+1,ysteps+1) = point2_zvalue;
57)         end
58)     end
59)     figure (666) % Name of the following pcshow
60)     pcshow(xyzdisplay,'MarkerSize',50) % Illustration of the cutter
   movement, the size of each point
61)     save
   'FilteredPaperResultWith3CutterCropTop0003EAC1PushVer3.mat'
```

9.5. Appendix E – Filtering the surface into a profile and calculate Ra value

```
1) clear
2) load('FilteredThesisTestRun1.mat')
3) figure (86) % Name of the following pcshow
4) pcshow(xyzdisplay,'MarkerSize',50)
5) ZTotal = 0
6) Rcount = 0
7) Ymax1 = (+0.00002)
8) Ymin1 = (+0.00000)
9) acount = 0
10)     xmax = (0.00195)
11)     for xcount = 1:kcount;
12)     if ((xmax) > xyzdisplay(xcount,1));
13)     acount = acount + 1;
14)     xyzdisplay1(acount,:) = xyzdisplay(xcount,:);
15)     end
16)     end
17)     figure (456) % Name of the following pcshow
18)     pcshow(xyzdisplay1,'MarkerSize',50)
19)     bcount = 0;
20)     xcount = 0;
21)     for xcount = 1:acount;
22)     if (Ymin1 < xyzdisplay1(xcount,2)) && (xyzdisplay1(xcount,2) <
   Ymax1); % filter the point of interest within the profile limit
23)     bcount = bcount + 1;
24)     xyzdisplay2(bcount,:) = xyzdisplay1(xcount,:);
25)     ZTotal = (ZTotal) + (abs(xyzdisplay1(xcount,3))); % calculate
   the total value of z
26)     Rcount = Rcount + 1;
27)     end
```

```
28)      end
29)      Zaverage = (ZTotal) / (Rcount); % calculate the mean of the z
   value
30)      Ra = 0
31)      RaTotal = 0
32)      Gcount = 0;
33)      for xcount = 1:bcount;
34)      if (Ymin1 < xyzdisplay1(xcount,2)) && (xyzdisplay1(xcount,2) <
   Ymax1);
35)      Gcount = Gcount + 1;
36)      AbsZvalue = ((abs(xyzdisplay2(xcount,3))) - Zaverage); %
   calculate the absolute value of z
37)      RaTotal = (abs(AbsZvalue)) + RaTotal; % calculate the total of
   the Ra
38)      end
39)      end
40)      Ra = (RaTotal) / (Rcount) % calculate the final Ra value
41)      figure (123) % Name of the following pcshow
42)      ax = pcshow(xyzdisplay2,'MarkerSize',200)
43)      zlim tight
```